Measurement of the Energy Spectrum of Cosmic Rays with the 26 Station Configuration of the IceTop Detector

D I S S E R T A T I O N

zur Erlangung des akademischen Grades

d o c t o r r e r u m n a t u r a l i u m
(Dr. rer. nat.)
im Fach Physik

eingereicht an der
Mathematisch-Naturwissenschaftlichen Fakultät I
der Humboldt-Universität zu Berlin

von
Dipl.-Phys. Fabian Kislat

Präsident der der Humboldt-Universität zu Berlin:
Prof. Dr. Jan-Hendrik Olbertz

Dekan der Mathematisch-Naturwissenschaftlichen Fakultät I:
Prof. Dr. Andreas Herrmann

Gutachter:
1. Prof. Dr. Hermann Kolanoski
2. Prof. Dr. Thomas K. Gaisser
3. Dr. Gernot Maier

eingereicht am: 21. Juli 2011
Tag der mündlichen Prüfung: 27. September 2011

Meiner Familie.
Weil Ihr immer für mich da seid,
Auch über eine große Entfernung.

Abstract

IceTop is an instrument at the geographic South Pole designed to detect cosmic ray air showers, particle cascades in the atmosphere initiated by high-energy cosmic rays. It is the surface component of the IceCube neutrino telescope. Since its completion in December 2010, IceTop consists of 81 detector stations covering an area of one square kilometer on the ice surface above IceCube. Each IceTop station consists of two ice-filled tanks in which the Cherenkov light emitted by charged air shower particles is measured. In this dissertation, an analysis of data taken in 2007 with 26 IceTop stations operational at that time is presented.

First, properties of air showers like core position, direction and shower size were reconstructed from the measured signals. The core position can be determined to an accuracy of up to 6 m and a direction resolution of up to 0.3° is achieved. The shower size is a measure of the energy of the primary particle and a resolution of up to 10% is achieved at high energies.

In the next step the relation between primary energy and shower size, as well as resolution and efficiency are determined from Monte Carlo simulations of air showers and the IceTop detector. Here, an assumption was made about the chemical composition of cosmic rays. The informations obtained in these simulations are then used to unfold the spectrum of measured shower sizes in order to obtain the all-particle cosmic ray energy spectrum. This is done independently for particles from three different zenith angle intervals.

The result of the unfolding depends on the assumed primary composition. Due to the isotropy of cosmic rays, results obtained in different zenith angle intervals must agree. While with the chosen analysis technique a simultaneous determination of primary particle mass and energy is limited due to systematic uncertainties, it has already been shown that the requirement of isotropy can be used to constrain the range of possible assumptions on the chemical composition of primary particles.

Good agreement of spectra from different zenith angle ranges has been found under the assumption of pure proton primaries, as well as for a mixture of protons and iron with a relatively large proton contribution at low energies and proton dominance at high energies. Under these assumptions the knee of the cosmic ray energy spectrum has been observed at energies between 3.97 and 4.20 PeV. The spectral index below the knee is about −2.7 and varies between −3.08 and −3.15 above the knee. Pure iron as primary particles can be excluded at a high confidence level below 25 PeV. Independent of the primary composition assumption a flattening of the energy spectrum with an index of about −3.0 has been observed above 30 PeV.

Zusammenfassung

IceTop ist ein Detektor am geographischen Südpol zum Nachweis von Luftschauern, Teilchenkaskaden in der Atmosphäre, die von hochenergetischen kosmischen Strahlen ausgelöst werden. IceTop ist die Oberflächenkomponente des Neutrinoteleskops IceCube. Seit der Fertigstellung im Dezember 2010 besteht IceTop aus 81 Detektorstationen auf einer Fläche von einem Quadratkilometer, auf der Eisoberfläche über IceCube. Diese Detektorstationen bestehen aus jeweils zwei eisgefüllten Tanks, mit denen Luftschauer nachgewiesen werden, indem das Čerenkov-Licht gemessen wird, das von geladenen Sekundärteilchen des Schauers im Eis erzeugt wird. Die vorliegende Dissertation umfasst eine Analyse von Daten, die im Jahr 2007 mit den 26 zu der Zeit installierten Stationen genommen wurden.

Dazu werden zunächst die Eigenschaften der Schauer, wie Position, Richtung und ein Maß für die Größe des Schauers aus den gemessenen Signalen rekonstruiert. Dabei wird eine Genauigkeit von bis zu 6 m bei der Bestimmung der Position des Schauerkerns und eine Richtungsauflösung von bis zu 0,3° erreicht. Die Schauergröße ist ein Maß für die Energie des Primärteilchens, und bei hohen Primärenergien wird eine Energieauflösung von etwa 10% erreicht, was vergleichbar mit ähnlichen Experimenten ist.

Im nächsten Schritt wird der Zusammenhang zwischen Primärenergie und Schauergröße aus Monte-Carlo-Simulationen von Luftschauern und des Detektors bestimmt, sowie Energieauflösung und Nachweiseffizienz. Hierbei wurde eine Annahme über die chemische Zusammensetzung der kosmischen Strahlung gemacht. Diese Informationen werden dann verwendet, um das Spektrum der gemessenen Schauergrößen zu entfalten und das Energiespektrum zu bestimmen. Dies wird getrennt für Schauer aus verschiedenen Zenitwinkelbereichen durchgeführt.

Das Resultat dieser Entfaltung hängt von der angenommenen Zusammensetzung der Primärteilchen ab. Die Ergebnisse, die aus der Entfaltung in verschiedenen Zenitwinkelintervallen gewonnen werden, müssen jedoch übereinstimmen, wenn man Isotropie der komischen Strahlung voraussetzt. Eine gleichzeitige Bestimmung von Masse und Energie der Primärteilchen ist mit der gewählten Methode aufgrund systematischer Unsicherheiten zwar nur eingeschränkt möglich, es wurde jedoch bereits gezeigt, dass die Voraussetzung der Isotropie kosmischer Strahlung ausgenutzt werden kann, um den Rahmen der möglichen Annahmen über die Zusammensetzung einzugrenzen.

Eine gute Übereinstimmung von Spektren aus verschiedenen Zenitwinkelbereichen wird unter der Annahme von reinen Protonen als Primärteilchen gefunden, sowie für eine Mischung aus Protonen und Eisen mit einem hohen Protonanteil bei niedrigen Energien und einer Mehrheit von Eisen bei hohen Energien. Unter diesen Annahmen ergibt sich eine Position des Knies im Spektrum der kosmischen Strahlung von 3,97 bis 4,20 PeV. Der spektrale Index unterhalb des Knies ist etwa −2,7 und oberhalb des Knies variiert

er zwischen −3,08 und −3,15. Reines Eisen auf der anderen Seite kann mit sehr großer Wahrscheinlichkeit ausgeschlossen werden. Unabhängig von der Annahme über die Zusammensetzung wird oberhalb von etwa 30 PeV ein Abflachen des Spektrums mit einem Index von etwa −3,0 beobachtet.

Contents

Introduction

Cosmic rays are charged particles constantly hitting the Earth's atmosphere from outer space at a rate of several thousand particles per square meter and second. Most of them are protons and light nuclei. Their energy spectrum is non-thermal and extends over many orders of magnitude with a steeply falling flux. The highest-energy cosmic rays have macroscopic energies of 1 Joule or more, many orders of magnitude higher than what is achieved by the most powerful man-made accelerators.

Cosmic rays have first been discovered in 1912 by the Austrian physicist Viktor Hess. He found out that the rate of ionization, which was attributed to natural radioactivity at ground level, increased during ascends with balloon and concluded that there had to be some ionizing radiation coming from outer space. The effects of cosmic rays, however, have already been observed thousands of years ago: auroras are fluorescent light emitted by nitrogen atoms excited by incident cosmic rays.

Since their discovery, cosmic rays have triggered various researches. Before the advent of modern particle accelerators they were the only source of high-energy particles. Anderson for example discovered the positron when studying the nature of cosmic rays. Furthermore, cosmic ray interactions in the upper atmosphere are the main source of radioactive ^{14}C atoms. Assuming that the flux of cosmic rays has been constant over time, the abundance of this isotope in organic material can be used to date archaeological artifacts using the method of radiocarbon dating.

One of the greatest problems in modern physics is the search for the origin of cosmic rays: which objects in space can accelerate particles to such enormous energies and what is the mechanism driving the acceleration? In the last few decades the field of astroparticle physics has developed with the goal of answering these questions. One of the main problems in the study of cosmic rays is that they are charged particles, which are deflected in cosmic magnetic fields, and thus unlike light do not point back to their origin. Instead, their arrival directions are isotropic to a high degree (apart from the very highest energy particles, which might show some anisotropy).

Methods to search for sources of cosmic rays include TeV γ-ray astronomy and the search for high energy cosmic neutrinos. Measurements of cosmic rays concentrate on the determination of the energy spectrum and mass composition. There are various theoretical models to describe acceleration and propagation of cosmic rays, which differ in their predictions of the spectrum and chemical composition of cosmic rays. Up to EeV energies the majority of cosmic rays is

considered to originate within our galaxy, but a transition to extragalactic cosmic rays could already start at lower energies. This make the energy range between 1 PeV and 1 EeV a particularly interesting field of study.

In this thesis a measurement of the cosmic ray energy spectrum between 1 PeV and 100 PeV was performed. In the introductory chapter, an overview over the phenomenology of charged cosmic rays and the air showers they initiate will be given. In Chapter 2 the IceCube Neutrino Observatory will be introduced with a focus on its surface component, IceTop, on which this work is based. The reconstruction of air shower properties from the measured signals will be the topic of Chapter 3. Since air showers are complex processes, Monte Carlo simulations are needed to relate reconstructed air shower characteristics to physical parameters of the primary particles. These simulations will be detailed in Chapter 4. An unfolding method described in Chapter 5 was then used to determine the cosmic ray energy spectrum from the measured data. In Chapter 6, systematic uncertainties will be studied and the results are presented in Chapter 7. Chapters 8 and 9 finally contain a discussion of the results in the context of the IceTop experiment and a summary of the work described in this thesis.

1. Cosmic rays and air showers

Since the discovery of cosmic rays by Victor Hess (1912) and the proof of the existence of air showers by Kohlhörster (Kohlhörster et al., 1938) and by Auger (Auger et al., 1939) many experiments have been conducted in order to determine their nature and origin. While the origin of cosmic rays remains speculative, we already have some knowledge on the nature of cosmic rays. The main questions cosmic ray physics are trying to answer concern the sources of cosmic rays, their source of power, and the actual mechanism accelerating the particles to energies exceeding 10^{20} eV.

In this chapter, a brief overview on the current knowledge about cosmic rays is given, mostly based on the books by Perkins (2003) and Gaisser (1990).

1.1. Energy spectrum and chemical composition

Up to energies of several 100 TeV, cosmic rays can be measured directly by satellite or balloon-borne experiments (see e. g. Furukawa et al., 2003; Asakimori et al., 1998) allowing a quite precise determination of their energy and mass on an event-by-event basis. At higher energies, fluxes are too low for such experiments and instead ground based detectors are used. Since Earth's atmosphere with a total depth of $1040\,\mathrm{g/cm^2}$ corresponds to roughly 12 hadronic interaction lengths (Nakamura et al., 2010), it is not transparent to cosmic rays. Thus, high energy particles initiate a cascade of particles called air shower that can reach the ground if the energy of the primary particle is high enough. Since such cascades can extend over a large area and because it is sufficient to sample a small part of the cascade, the effective area of a ground based air shower detector can be much larger than the actual detector area. The disadvantage of these experiments is that they rely on modeling of the particle cascade in the atmosphere. Furthermore, direct particle identification is not possible, and in the best case only primary mass groups can be resolved. Often, only the mean logarithmic mass is measured:

$$\langle \ln A \rangle = \sum_{i=1}^{N} n_i \ln A_i, \tag{1.1}$$

where the sum runs over N particle species i, n_i is the relative abundance of species i, and A_i is its nuclear mass number.

A current compilation of results on the all-particle cosmic ray energy spectrum

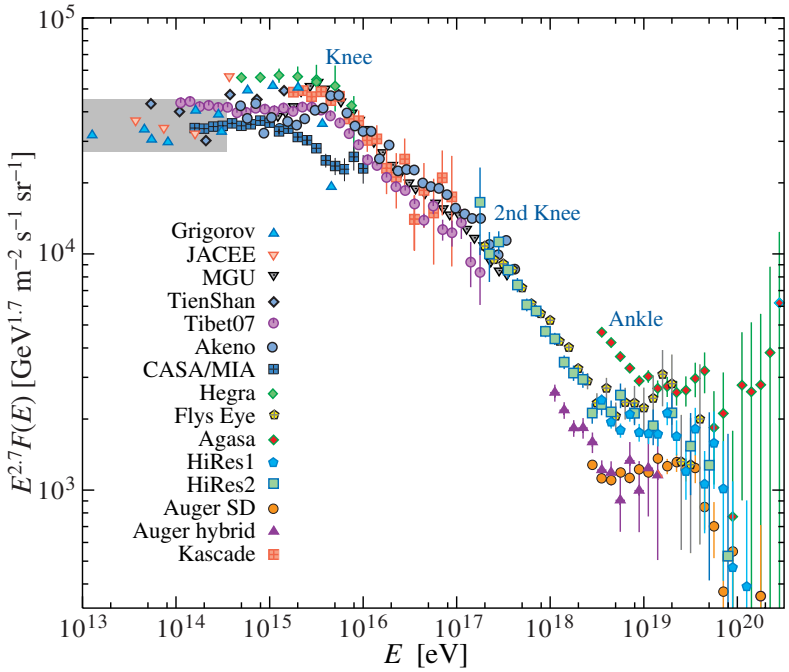

Figure 1.1.: Compilation of measurements of the energy spectrum of cosmic rays, from Nakamura et al. (2010). The flux has been weighted with $E^{2.7}$ to enhance features of the spectrum. The gray band at low energies indicates the range of direct measurements.

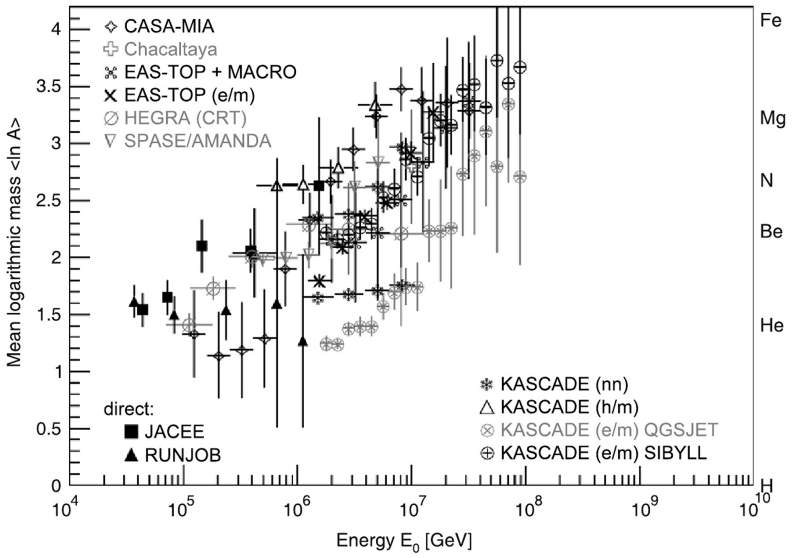

Figure 1.2.: Compilation of measurements of the chemical composition of cosmic rays, from Blümer et al. (2009).

is shown in Fig. 1.1. It roughly follows a power law

$$\frac{\mathrm{d}N}{\mathrm{d}E} \propto E^{\gamma} \tag{1.2}$$

with only few features. Therefore, cosmic rays have to be of non-thermal origin. The spectral index is $\gamma \approx -2.7$ up to the "knee" at about 4 PeV where it steepens to $\gamma \approx -3.1$. At the "ankle" around $10^{18.5}$ eV the spectrum flattens again, before data are consistent with a cut-off at about 5×10^{19} eV, which is often associated with the GZK effect (Greisen, 1966; Zatsepin and Kuz'min, 1966). This effect predicts a cut-off of the cosmic ray energy spectrum at the threshold energy for the production of Δ resonances of protons with cosmic microwave background photons,

$$p + \gamma_{\mathrm{CMB}} \rightarrow \Delta^{+} \rightarrow p/n + \pi^{0/+}. \tag{1.3}$$

At energies below 100 TeV cosmic rays mostly consist of protons and light nuclei with a small admixture of heavier nuclei. Only about 2% of all cosmic rays are electrons or positrons with energies below the TeV range. Above the knee composition begins to change getting heavier, see Fig. 1.2. Although systematic uncertainties are large, most experiments show that light elements cut off at energies of a few PeV while heavier elements persist up to more than 100 PeV. Recent experiments have revealed more structure in the all-particle spectrum in this energy range (e.g. Garyaka et al., 2008; Arteaga-Velázquez et al., 2010) and KASCADE-Grande has shown evidence for a "second knee" (Arteaga-Velázquez et al., 2010).

In the EeV energy range measurements from HiRes and Auger disagree on the composition. While the HiRes results (Abbasi et al., 2005) indicate that the composition becomes lighter toward higher energies, Auger observes a composition that becomes heavier again above 2×10^{18} eV (Abraham et al., 2010). Measurements of the composition in this energy range are important to discern different possible explanations of the ankle feature.

1.2. Sources, acceleration and propagation to Earth

Apart from particles up to a few GeV of energy which are associated with solar flares, the origin of cosmic rays is outside the solar system but otherwise generally unknown. Cosmic rays up to PeV energies, however, are considered to originate inside our galaxy, while cosmic rays of the highest energies are assumed to originate mainly outside our galaxy, accelerated for example in Active Galactic Nuclei or Gamma Ray Bursts.

1.2.1. Fermi acceleration

The underlying mechanism of acceleration in most source models is diffusive shock acceleration, also called first order Fermi acceleration.

In 1949 Fermi proposed a stochastic mechanism where particles gain energy in collisions with randomly moving magnetized clouds:

$$E_1 = (1 + \xi)E_0. \tag{1.4}$$

The energy gain ξ_{cloud} in this case is proportional to the square of the velocity of the supersonic (but sub-relativistic) velocity βc of the cloud, $\xi_{\text{cloud}} \sim \beta^2$.

A more efficient acceleration is achieved, if it occurs at shock fronts such as those created by a supernova explosion. All collisions of the highly relativistic particles with the sub-relativistically moving gas on the other side of the shock front are head on. The reason is that in the case of a shock front a reference frame exists in which the gas in front of and behind the shock converge (Reynolds, 2008). After a particle crosses the shock front it undergoes multiple elastic reflections on turbulent magnetic fields before crossing the shock front again. The average energy gain in these collisions is proportional to the velocity of the shock, $\xi_{\text{shock}} \sim \beta$. Therefore, this mechanism is called first order Fermi acceleration.

After N collisions a particle has the mean energy

$$E_N = (1 + \xi)^N E_0. \tag{1.5}$$

Given the probability P that the particle remains in the acceleration region for further acceleration, this leads to a power law energy spectrum,

$$N(E)\,\mathrm{d}E = E^{\ln(P)/\ln(1+\xi)-1}\mathrm{d}E = E^{-(s+1)}\mathrm{d}E. \tag{1.6}$$

For shock-wave acceleration, it turns out that typically $s \approx 1.1$, so that the index of the differential spectrum of the source is $\gamma \approx 2.1$. The steeper observed spectrum with $\gamma = 2.7$ could be explained by a rigidity dependent escape probability $1 - P$, which is in fact supported by measurements of abundances of different nuclei. Rigidity is defined as

$$R = \frac{p\,c}{Z\,e}, \tag{1.7}$$

with the particle momentum p and charge Ze. An alternative explanation could be interactions of cosmic rays with the interstellar medium during propagation.

1.2.2. Sources

Cosmic rays of energies above a few GeV originate outside our solar system, but there are indications from gamma ray measurements that their origin lies within our galaxy.

Shock waves of supernova remnants (SNR) have been discussed since a long

time as candidates for galactic sources of cosmic rays. If cosmic rays have a characteristic residence time in the galaxy of 10^7 years (which is indicated by some measurements, see next subsection), the power output by supernovae in the galaxy would large enough to account for the cosmic ray energy density $\rho_E \approx 1\,\mathrm{eV/cm^3}$. Only a few percent of their total power output would need to be converted to cosmic rays. Furthermore, Fermi acceleration at the supernova shock front is a very efficient energy converter that can yield the observed spectrum.

The maximum energy to which particles can be accelerated in SNR is determined by the strength of the shock, the magnetic field B present in the medium surrounding the shock front, and the time T_A for which acceleration is efficient:

$$E_{\max} \sim Ze\,B\,u_1\,T_A, \tag{1.8}$$

where u_1 is the velocity of the shock front and Ze is the charge of the particle being accelerated. The magnetic field strength determines the time it takes to deflect a particle back after it has crossed the shock front. Due to its expansion, the acceleration efficiency of an SNR decreases. Maximum energies are obtained significantly before the shock front has swept up its own mass. Gaisser (1990) concludes that this leads to maximum energies of the order of 100 TeV. However, recent simulations show that interactions between the particles being accelerated and the surrounding medium can amplify magnetic fields allowing for maximum energies in the knee region (Hillas, 2006). Figure 1.3 shows an X-ray image of Tycho's SNR. The thin outer layer of synchrotron radiation indicates that relativistic electrons gain energy in a small region around the shock front (Hillas, 2006).

Thus, one can assume that galactic accelerators are able to produce cosmic ray protons with energies up to several PeV and iron nuclei of $O(100\,\mathrm{PeV})$. Even though rapidly spinning young neutron stars could be thought of as accelerating particles to the highest energies observed, astrophysical sources of cosmic rays with even higher energies inside our galaxy are disfavored (Blümer et al., 2009):

- It would be hard to explain the apparent isotropy of cosmic rays to energies beyond 10^{19} eV.
- In the galactic magnetic field of typically $B = 3 \cdot 10^{-10}\,\mathrm{T}$, protons of $E = 10^{20}\,\mathrm{eV}$ have a gyroradius of $\rho \approx 30\,\mathrm{kpc}$, which corresponds to the diameter of our galaxy. The galactic magnetic field would thus be incapable of containing such particles, at least if they have a low charge. These particles thus escape from the galaxy on much shorter time scales than lower energy particles.

Active galactic nuclei (AGN) are particularly bright galaxy cores believed to consist of a super-heavy black hole accreting mass. Accretion is a very efficient mechanism to convert gravitational energy to radiation which leads to the extraordinary brightness of AGN. Together with the fact that their radiation spectra are non-thermal, this makes them very good candidates for the acceleration of cosmic rays to the highest energies. Many AGN like the core of galaxy M87, shown

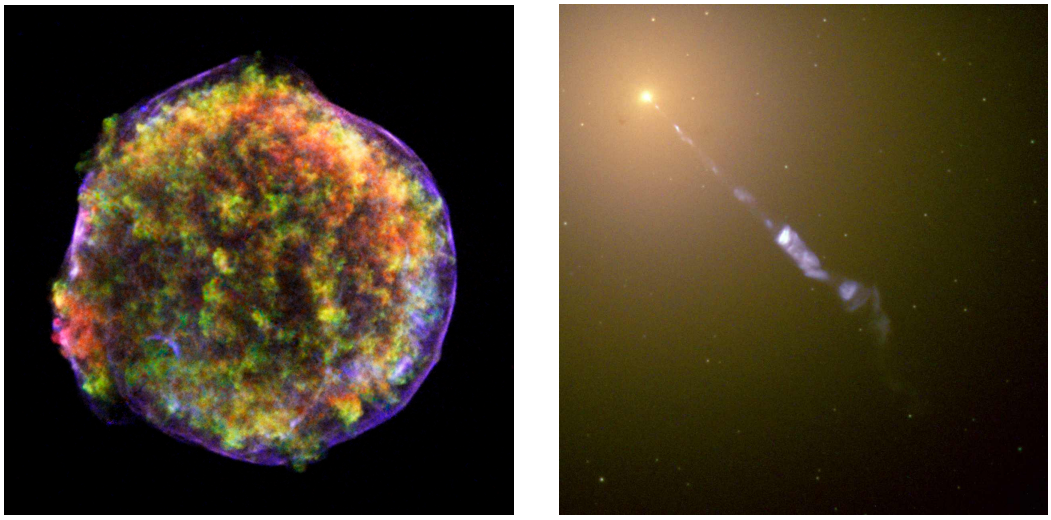

Figure 1.3.: *Left:* CHANDRA image of Tycho's SNR (Warren et al., 2005). The thin outer layer of strong synchrotron radiation suggests that relativistic electrons are being accelerated in this region. *Right:* Hubble image of the galaxy M87 and its huge jet (from `http://hubblesite.org/gallery/album/pr2000020a/`).

in Fig. 1.3, emit a huge jet. Shock waves in these jets are potential accelerators and therefore particularly interesting for cosmic ray physics.

Several experimental efforts are being undertaken in order to test their role as cosmic ray sources:

- in γ-ray astronomy, precise measurements of the spectral shape can help distinguishing leptonic from hadronic models;
- a neutrino signal from an AGN would be a clear evidence for the acceleration of hadrons;
- at the very highest energies, the reach of cosmic ray protons is limited by the GZK effect, while at the same time their deflection due to magnetic fields is relatively small so that point sources could be identifiable. Auger reported evidence for a correlation of ultra high energy cosmic rays with nearby AGN (Abraham et al., 2007).

1.2.3. Propagation in the galaxy

After their acceleration, cosmic rays spend $O(10^7)$ years in the galaxy, on average traversing some 5 to 10 $\mathrm{g/cm^2}$ equivalent of hydrogen. They are scattered by more or less random magnetic fields, which is the reason for their apparently isotropic arrival directions. In this section our current understanding of

cosmic ray propagation in the galaxy will be summarized, based on the review by Strong et al. (2007).

For a particular particle species, propagation in the galaxy can be described by a propagation equation of the general form:

$$\begin{aligned}\frac{\partial\psi(\boldsymbol{r},p,t)}{\partial t} &= q(\boldsymbol{r},p,t) + \boldsymbol{\nabla}\cdot(D_{xx}\boldsymbol{\nabla}\psi - \boldsymbol{V}\psi) \\ &\quad + \frac{\partial}{\partial p}p^2 D_{pp}\frac{\partial}{\partial p}\frac{1}{p^2}\psi - \frac{\partial}{\partial p}\left[\dot{p}\psi - \frac{p}{3}(\boldsymbol{\nabla}\cdot\boldsymbol{V})\psi\right] - \frac{1}{\tau_f}\psi - \frac{1}{\tau_r}\psi,\end{aligned} \tag{1.9}$$

where $\psi(\boldsymbol{r},p,t)$ is the cosmic-ray density per unit of particle momentum p at position $\boldsymbol{r}$ at time t. Furthermore,

- $q(\boldsymbol{r},p,t)$ is the source term, including primary sources, as well as spallation and decay contributions;
- D_{xx} is the spatial diffusion coefficient;
- $\boldsymbol{V}$ is the convection velocity;
- D_{pp} is the diffusion coefficient in momentum space;
- and τ_f and τ_r are the time scales for losses by fragmentation and radioactive decay.

Many observation can be described by simplified leaky-box models, where cosmic rays are assumed to stream freely inside the galaxy leaking out of it when they reach the boundaries. Diffusion and convection are replaced by a leakage term and an associated characteristic time. Energy gains and losses can often be neglected, assuming that the same energy per nucleon is kept in fragmentation processes (Gaisser, 1990). However, when interpreting results obtained with this kind of description, care must to be taken converting numerical results to physically meaningful quantities.

Magnetic fields play a crucial role in cosmic-ray propagation. Their strength and orientation can be probed remotely using radio polarization measurements especially of pulsars and the Zeeman effect at optical wavelengths. Zeeman splitting and Faraday rotation (change of the polarization vector of linearly polarized electromagnetic waves) are sensitive to the magnetic field component along the line of sight, whereas polarimetry of starlight or dust and synchrotron radiation are more sensitive to the perpendicular component. Furthermore, Faraday rotation is wavelength dependent so that the original polarization does not have to be known if the distance of the emitter can be determined. The galactic magnetic field has a strength of roughly $3\,\mu$G parallel to the spiral arms, but with large fluctuations (Han and Wielebinski, 2002).

Diffusion of cosmic rays results from particle scattering on random magnetohydrodynamic waves, which arise from perturbations of magnetized plasmas

(e. g. caused by streaming cosmic rays). At cosmic ray energies of 1 GeV per nucleon, typical values of the diffusion coefficient of $D_{xx} \sim O(10^{28}\,\mathrm{cm}^2/\mathrm{s})$, increasing with magnetic rigidity, are found. Additionally, convection of cosmic rays could occur and galactic winds, which are observed in many galaxies, suggest that convective or advective transport may be important (Strong et al., 2007). However, in our own galaxy, galactic winds seem to be confined to the galactic center region, and it is unclear whether they play a significant role in cosmic-ray transport. Furthermore, if cosmic rays scatter on random magnetic fields, stochastic acceleration as in second order Fermi acceleration can occur during propagation. This is also referred to as re-acceleration.

Most experimental input to the modeling of cosmic-ray propagation comes via observations of secondary cosmic rays. Secondary cosmic rays are nuclei that are produced as spallation products during propagation of primary particles which are accelerated at the source (Gaisser, 1990). Secondary cosmic rays can be measured by comparing the abundance of isotopes in cosmic rays to their abundance as end products of stellar nucleosynthesis. Most interesting are those nuclei that are practically missing from stellar matter but much more abundant in cosmic rays. Separation of individual nuclei or even isotopes is only possible in direct measurements and can therefore only be done at low energies compared to the knee where fluxes are large enough.

The cosmic-ray boron-to-carbon (B/C) ratio is a frequently used reference ratio, because boron only occurs as secondary cosmic rays. The grammage traversed by cosmic rays can be inferred from the measured B/C ratio because carbon, nitrogen, and oxygen are the main progenitors of boron and the production cross-sections are known.

Unstable secondary cosmic ray isotopes (most importantly ^{10}Be) on the other hand, act as radioactive clocks. The time cosmic rays spend inside the galaxy before observation can be inferred from their abundance. Combined with data from stable secondary cosmic rays, one can conclude that cosmic rays are not confined to the galactic disk, but also fill a galactic halo with a height of about 4 kpc.

Furthermore, K-capture is suppressed after acceleration because the nuclei are stripped of their electrons. Thus, the decay of isotopes that only decay through K-capture is only possible before acceleration. From the abundance of such nuclei in cosmic rays, which are produced in explosive nucleosynthesis (such as ^{59}Ni), the delay between synthesis and acceleration can be estimated to be $\geq 10^5$ years. This supports models in which supernovae accelerate existing interstellar material, rather than their own ejecta.

1.3. Cosmic rays at the knee and above

Up to PeV energies the cosmic ray energy spectrum follows a rather smooth power law. At 4 PeV the spectral index steepens from $\gamma \approx -2.7$ to $\gamma \approx -3.1$. This feature is called the “knee” and was first observed by Kulikov and Khristiansen (1959).

Understanding its origin is widely believed to be crucial in order to understand the origin of cosmic rays. The review by Hörandel (2004) gives a good overview of experimental results and theoretical models of the knee region.

The various models can (in principle) be distinguished with the help of measurements of the all-particle energy spectrum and the chemical composition of cosmic rays in the knee region and above. Unfortunately, fluxes are too low to be measured directly with current balloon or satellite-borne experiments. Indirect measurements at ground level have so far been unable to effectively discriminate between models.

Hörandel divides the theoretical models of the origin of the knee into four categories:

1. the origin of the knee is attributed to the acceleration process;
2. the knee is connected with leakage of cosmic rays from the galaxy;
3. interaction of cosmic rays with background particles are considered as origin for the knee;
4. the knee is not of astrophysical origin, but caused by a new type of interaction in air showers.

In the following a short summary of models in the four categories will be given.

1.3.1. Cosmic-ray acceleration

As described in subsection 1.2.2, acceleration in SNR shock fronts has a maximum energy for protons potentially in the knee region. Furthermore, according to Eq. (1.8), this energy limit increases with nuclear charge, possibly allowing for maximum energies of iron nuclei of $O(100\,\mathrm{PeV})$. Thus, if the knee is due to the maximum energy of supernova shock acceleration a knee with increasing energy $\propto Z$ should be found for individual particle species. Additionally, heavy elements are accelerated more efficiently and thus will have a harder spectrum. This would lead to an increasing mean logarithmic mass, $\langle \ln A \rangle$ (see Eq. 1.1). Such a scenario was first considered by Peters (1959, 1961), and is therefore also referred to as 'Peters Cycle'.

There are several variations of SNR shock modeling, including models where the magnetic fields are not parallel to the direction of the shock front expansion and models that consider acceleration by a variety of different flavors of supernovae.

A model by Stanev et al. (1993) considers two different galactic sources with different cutoff energies to describe the knee. The spectrum at energies above 100 PeV is described by introducing an additional extra-galactic component. A specific feature of the model is the relatively sharp knee, which was observed by early experiments like MSU and Akeno (Hörandel, 2004).

Erlykin and Wolfendale (2001) proposed a model in which, in addition to a background caused by many undefined sources, the structure around the knee

is caused by a recent and nearby supernova explosion. Main characteristic of their model is that the spectrum in the energy range above the knee cannot be described by a smooth power law. Recently observed structures in the spectrum in this energy range probably support this hypothesis.

All these models have in common that the position of the knee of individual components increases with nuclear charge Z and the mean logarithmic mass increases with energy. Around 100 PeV, iron should be the dominant component of cosmic rays. The phenomenological poly-gonato model (Hörandel, 2003) even predicts a considerable contribution from heavier nuclei up to uranium.

1.3.2. Leakage of cosmic rays from the galaxy

The second class of models attributes the knee to leakage of cosmic rays from the galaxy, differing in their description of propagation and leakage.

A basic assumption made by several models is that the galactic magnetic field can be described by a regular global field and a random component. It has been shown that at low energies propagation of cosmic rays could be dominated by diffusion in the random magnetic fields, while at high energies, drift in the global magnetic field could become dominant. This transition could be the origin of the cosmic ray knee, even if the source spectra are completely featureless power laws. Since diffusion and drift in magnetic fields depend on rigidity, the position of the knee for each primary particle species would be proportional to Z in such a scenario. Several variations of this basic idea exist, making different assumptions about the structure of magnetic fields inside the galaxy.

A model by Swordy (1995) uses power law input spectra with a rigidity dependent cutoff and combines it with cosmic-ray propagation using a Leaky Box model. Thus, in this model, the origin of the knee is assumed to be the acceleration mechanism, but its exact shape is determined by rigidity dependent leakage from the galaxy.

1.3.3. Interaction with background particles

Hörandel (2004) lists two classes of models attributing the knee to interactions of cosmic rays with background particles: photo-disintegration and interactions with background neutrinos.

Both, soft photons and optical and UV photon fields around compact galactic objects have been investigated based on an idea by Hillas (1979). The knee is then described as a combined effect of leakage of protons and photo-disintegration of heavier primaries, as well as energy losses due to pion photo-production depending on the energy of the photon field. In these models, $\langle \ln A \rangle$ first increases due to the increase of the onset of photo-disintegration with mass before secondary protons become dominant around 10^{17} eV.

Another model connects the origin of the knee with interactions of cosmic

rays with background neutrinos. The authors argue that the density of standard model neutrinos predicted by Big Bang cosmology is strongly increased due to gravitational clustering inside galaxies. Cosmic rays then lose energy via $p + \nu \rightarrow \nu + \Delta$ and $\Delta \rightarrow p + \pi$ above a threshold of $E_p = 3\,\mathrm{PeV}$ assuming a neutrino mass of $m_\nu = 100\,\mathrm{eV}$. Other candidates for such a process are hypothetical dark matter particles.

1.3.4. Particle physics

Kazanas and Nicolaidis (2001) investigate the possibility that a new particle physics process could be the origin of the knee. This process, which sets in above a certain threshold energy, transfers energy to a particle not detected by air shower experiments. This would lead to an underestimation of the primary energy by air shower experiments. In their article, Kazanas and Nicolaidis describe the proton-proton cross-section as a combination of a constant term to describe standard model processes and an additional part describing the new process above the threshold energy. The knee position of individual primaries in such a model would increase with primary mass since a certain minimum energy per nucleon is required for the new physics process to set in.

However, such a description is already severely limited by Tevatron data (Dixit et al., 2010). On the other hand, the authors also point out that at high energies, *pp* interactions may not be cleanly separable into a standard model and a "new physics" part, but that in every collision a certain amount of energy is lost due to new processes. In such a scenario the total cross section would not need to change drastically in order to explain the knee. Even at the LHC, a measurement of the total *pp* cross section alone could not rule out such a scenario. Instead, a direct search for missing energy would be required.

1.3.5. Combinations of effects

Most models described in the literature deal with individual aspects of cosmic-ray physics to explain the origin of the knee: acceleration, propagation, or interactions. It is very likely that the knee is in fact caused by a combination of different effects, but current experiments do not constrain possible scenarios very strongly. Given the weak experimental boundaries, Hörandel (2004) concludes that "acceleration in supernova remnants and diffusive propagation through the Galaxy seem to be very attractive models to understand the origin of the knee."

1.4. Air showers

When a cosmic-ray particle hits the Earth's atmosphere, it initiates a cascade of particles, which can reach the ground if the primary energy is high enough.

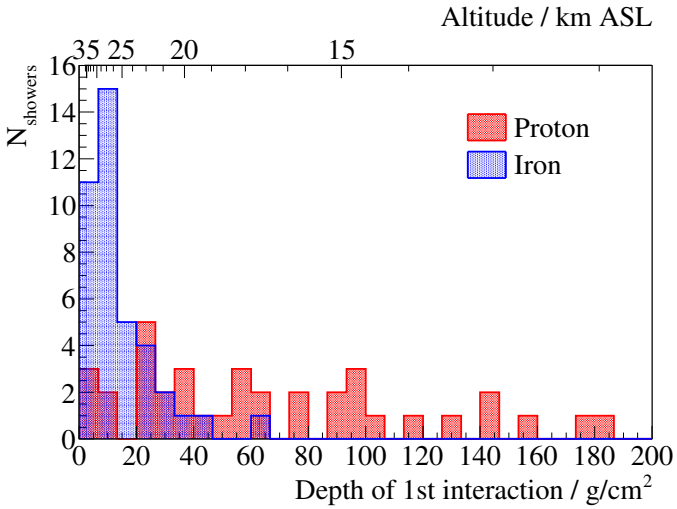

Figure 1.4.: Depth of the first interaction of simulated vertical 1 PeV proton and iron showers (40 events each).

The atmosphere, thus, acts as a large calorimeter. Its density profile can be approximately described by the barometric formula:

$$\rho(h) \approx \rho_0 e^{-h/h_0}, \tag{1.10}$$

with $\rho_0 \approx 1.225\,\mathrm{kg/m^3}$ and the scale height $h_0 \approx 8.4\,\mathrm{km}$. A very detailed account of processes in an air shower is given by Anchordoqui et al. (2004) and this section mostly follows their review article.

The atmospheric profile can be described by the vertical atmospheric depth,

$$X_v(h) = \int_h^\infty \rho(z)\mathrm{d}z = \rho_0 h_0\, e^{-h/h_0}, \tag{1.11}$$

which leads to a total overburden at sea level of $X_0 = 1040\,\mathrm{g/cm^2}$. The actual slant depth traversed by an air shower, which is the relevant quantity for particle interactions, increases with zenith angle as $X = X_v/\cos(\theta)$ up to zenith angles of $\theta \approx 70°$ (above that, the curvature of the atmosphere needs to be taken into account). Assuming a mean free path length of protons in air of $\lambda_I \approx 90\,\mathrm{g/cm^2}$ (Nakamura et al., 2010), Eq. (1.11) leads to a height of the first interaction, h_1, of

$$X_v(h_1) = \lambda_I \quad \Leftrightarrow \quad h_1 \approx 20.5\,\mathrm{km}. \tag{1.12}$$

The altitude of the first interaction increases with primary mass because of the increasing cross section. This is illustrated in Fig. 1.4, where the depth of the first interaction of simulated vertical 1 PeV proton and iron showers is shown.

The interaction of a high-energy cosmic-ray nucleus of mass number A and

energy E_0 with the atmosphere can be described as interactions of A independent nucleons with energy E_0/A because nuclear binding energies are small compared to the energy transfer in such an inelastic scattering. Despite the fact that this superposition model is only a simple approximation, it can be used to explain many general properties of an air shower (Gaisser, 1990).

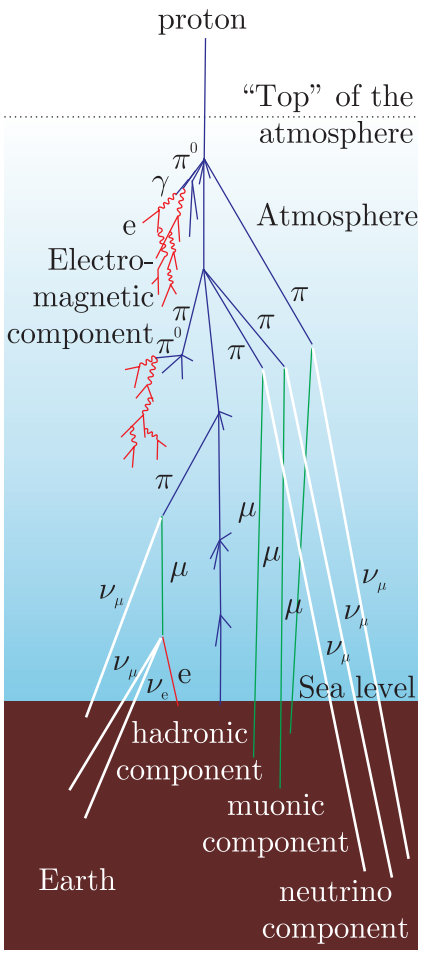

Figure 1.5.: Sketch of the development of an air shower, adapted from Kolanoski (2010).

The secondary particles that are created in the hadronic cascade (see Fig. 1.5) that develops in the atmosphere can be classified in three categories:

- a soft electromagnetic component;
- a hard muon component;
- and a hadronic component.

The hadronic component of an air shower consists mainly of pions, neutrons and protons. High energy hadrons (mostly pions) form the shower core with a radius of $\sim 30\,\mathrm{m}$, whereas hadrons of lower energies (mostly neutrons) have a very wide lateral distribution. This can be seen in Fig. 1.6 where the lateral distributions of different groups of particles in one single vertical 10 PeV proton shower are shown. Of course, in order to derive more quantitative numerical results, several showers would need to be simulated, but Figures 1.6 and 1.7 only serve to illustrate some general features of air showers.

The hadronic core constantly feeds the soft electromagnetic component of an air shower through the decay of neutral pions to two photons:

$$\pi^0 \to \gamma\,\gamma. \tag{1.13}$$

Since π^0 have a very short lifetime of $8.4 \cdot 10^{-17}\,\mathrm{s}$ (Nakamura et al., 2010) they almost always decay which makes the energy transfer from the hadronic to the electromagnetic component of an air shower very efficient. In fact, about one third of the hadronic energy is transferred to electromagnetic component in every hadronic interaction length λ_I (Gaisser, 1990). The photons produced in this way initiate electromagnetic sub-showers through e^+e^- pair production. This makes photons the most abundant particles in an air shower, followed by electrons and positron, which can be seen in Figures 1.6 and 1.7.

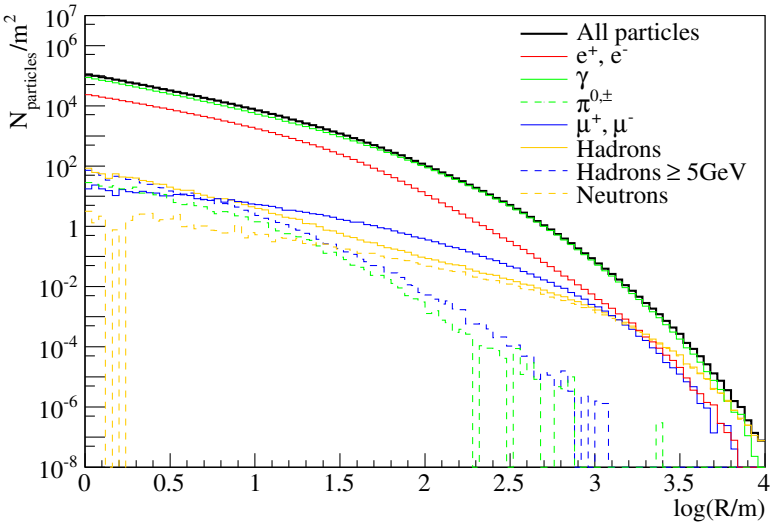

Figure 1.6.: Lateral distribution of different groups of secondary particles at the altitude of IceTop (2835 m) in a simulated vertical 10 PeV proton shower. While more detailed numerical results would require simulation of many air showers, this graph can serve to illustrate some basic properties of particle lateral distributions. The energy spectra of secondary particles are shown in Fig. 1.7.

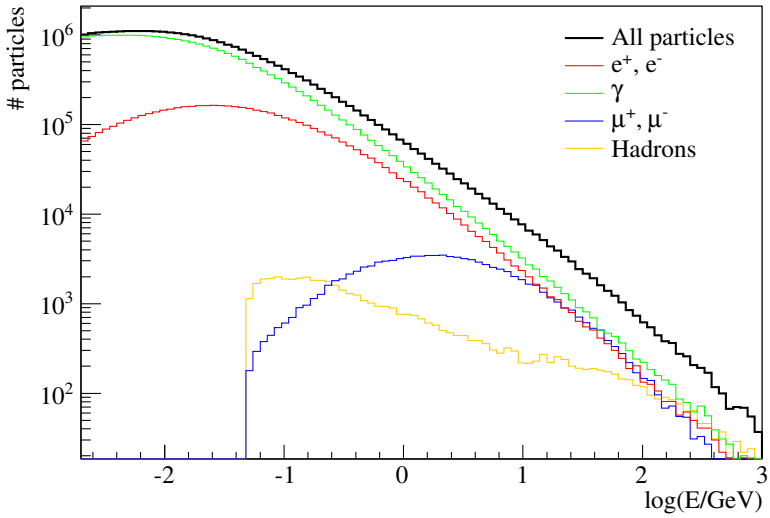

Figure 1.7.: Energy spectra of different groups of secondary particles in a simulated vertical 10 PeV proton shower at the altitude of IceTop (2835 m). The lateral distributions of particles are shown in Fig. 1.6.

Muons in air showers are mostly produced in the decay of charged kaons and pions,

$$K^{\pm}, \pi^{\pm} \rightarrow \mu^{\pm} + \overset{(-)}{\nu}_{\mu}. \tag{1.14}$$

Together with neutrinos they form the hard component of an air shower because they penetrate very deeply.

Muons of TeV energies are produced in the first few interactions, and are able to reach depths of more than 1 km w.e. (kilometers water equivalent). Due to the relatively long mean lifetime of charged pions of $2.6 \cdot 10^{-8}$ s (Nakamura et al., 2010), muon production at high altitudes is governed by the interplay of the decay of high-energy charged pions and their interaction. Since heavier primary nuclei interact at higher altitudes, the mean free path of pions is longer (due to the lower air density) than at lower altitudes. This increases the probability that a pion decays instead of interacting, which leads to an increasing number of high energy muons with increasing primary mass. On the other hand, those high-energy mesons that interact will produce further secondary mesons forming the hadronic core of the air shower. The number of muons above a certain energy can be parametrized by the Elbert formula, and scales with the primary mass as (Gaisser, 1990):

$$N_{\mu}(> E_{\mu}) \propto A^{0.243}. \tag{1.15}$$

High energy muons form a strongly collimated muon bundle.

Lower energy muons, on the other hand, are produced much deeper in the atmosphere by low-energy charged pions ($E \lesssim 100\,\mathrm{GeV}$), which almost always decay. Since muons are relatively unaffected by multiple scattering, their lateral distribution is governed by the lateral and angular spread of the parent pions. Furthermore, muons do not multiply as the electromagnetic component of an air shower, which leads to relatively low total numbers. Based on theoretical calculations, Gaisser (1990) gives a moderate primary mass dependence of the number of low-energy muons:

$$N_{\mu}(E_{\mu} > 1\,\mathrm{GeV}) \propto A^{1-p_{\mu}} \tag{1.16}$$

with $p_{\mu} \approx 0.86$ obtained from Monte Carlo simulations. Unlike other components of an air shower, the energy spectrum of muons peaks at relatively high energies of more than 1 GeV, as seen in Fig. 1.7.

The longitudinal development of the number of electrons N_e in an air shower can be described by the Gaisser-Hillas profile:

$$N_e(X) = N_{e,\max}\left(\frac{X - X_1}{X_{\max} - X_1}\right)^{\frac{X_{\max} - X_1}{\lambda}} \exp\left(\frac{X_{\max} - X}{\lambda}\right), \qquad X \geq X_1, \tag{1.17}$$

where X is the slant depth, X_1 is the slant depth of the first interaction, $X_{\max}$ is the depth shower maximum, $N_{e,\max}$ is the electron number at this depth,

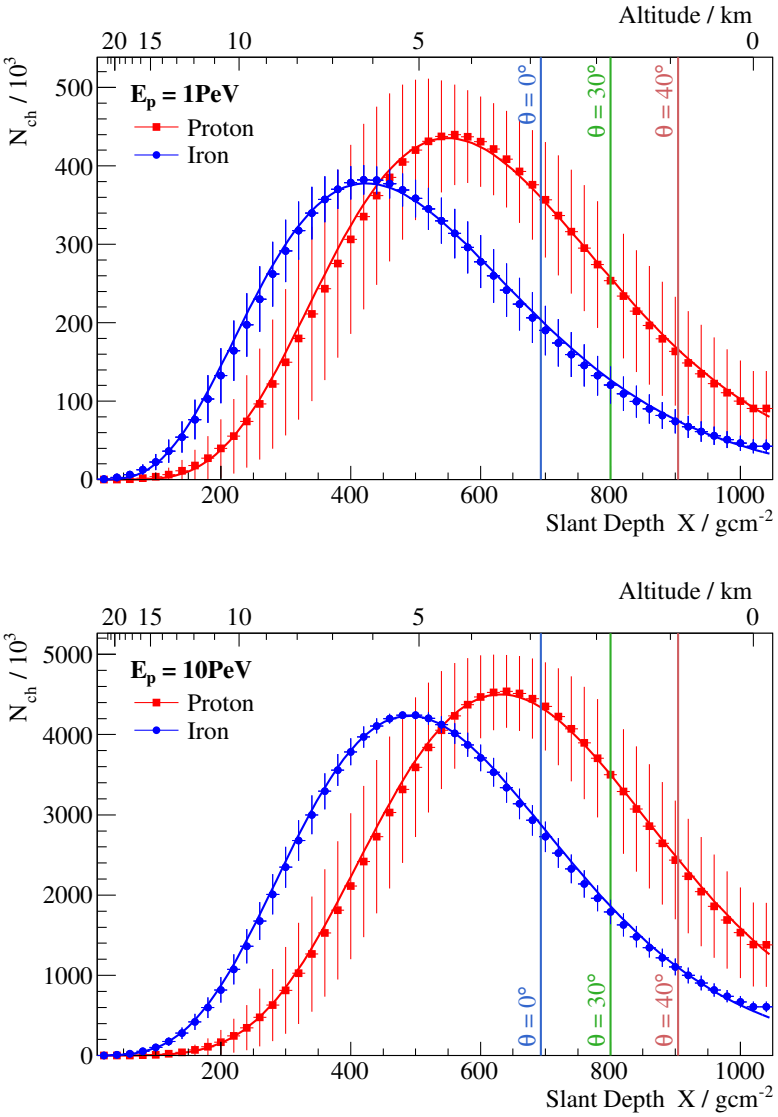

Figure 1.8.: Longitudinal development of simulated vertical proton and iron showers with primary energies of 1 PeV (top) and 10 PeV (bottom). Shown is the number of charges particles as a function of slant depth. The upper horizontal axis gives the corresponding altitude in kilometers. In each case several showers were simulated and the error bars give the spread of the longitudinal profiles. The solid lines are fits of the Gaisser-Hillas profile (1.17). The vertical lines indicate the slant depth of the IceTop array (which is at an altitude of 2835 m) for three different angles of incidence.

and $\lambda \approx 70\,\mathrm{g/cm^2}$ is an effective radiation length. As seen in Fig. 1.8, shower development can be described by three phases: the growth phase during which the particle number increases; the shower maximum; and the tail, where particles lose energy due to ionization losses and are eventually absorbed or decay.

Iron showers develop faster than proton initiated showers, which have their shower maximum deeper in the atmosphere. Furthermore, fluctuations of the overall shower development, which are mostly caused by variations of the altitude of first interaction, are smaller for heavier primaries. These differences can be understood in the framework of the superposition model by the fact that to first approximation a primary particle of mass A initiates A independent air showers of primary energy E_0/A, leading to approximately $X_{\max} \propto \ln(E_0/A)$. This increased initial particle multiplicity reduces the fluctuations of shower development.

The vertical lines in Fig. 1.8 indicate the slant depth traversed by air showers with different zenith angles before reaching the IceTop detector (introduced in Chapter 2), which is located at an altitude of 2835 m. Effectively, measuring the particle numbers in air showers of different zenith angles corresponds to measurements at different altitudes. Since the shower maximum of air showers with primary energies $E_p \lesssim 100\,\mathrm{PeV}$ is above the altitude of IceTop, inclined showers are attenuated by the atmosphere. This attenuation depends on primary mass, which will be discussed in more detail in Section 5.5.

The lateral distribution of secondary particles in air showers (see Fig. 1.6) is due to Coulomb scattering of charged particles off nuclei in the atmosphere. Kamata and Nishimura (1958) and later Greisen (1960) give a theoretical description of the lateral distribution of charged particles in an electromagnetic shower, known as the NKG formula:

$$\rho(R) = \frac{N_e}{r_M^2}\, C \left(\frac{r}{r_M}\right)^{s_{\mathrm{NKG}}-2} \left(1 + \frac{r}{r_M}\right)^{s_{\mathrm{NKG}}-4.5}, \tag{1.18}$$

where N_e is the total number of electrons, r_M is the Molière radius (which has a value of $r_M \approx 105\,\mathrm{m}$ at an altitude of 3 km), and

$$C = \frac{\Gamma(4.5 - s_{\mathrm{NKG}})}{2\pi\Gamma(s_{\mathrm{NKG}})\Gamma(4.5 - 2s_{\mathrm{NKG}})}. \tag{1.19}$$

The parameter

$$s_{\mathrm{NKG}} = 3\left(1 + \frac{2\ln(E_0/\varepsilon_0)}{t}\right)^{-1} \tag{1.20}$$

characterizes the stage of shower development in terms of the slant depth in radiation lengths x_0, $t = X/x_0$, with the primary energy E_0 and the critical energy ε_0 below which particles no longer multiply but are absorbed. It is called the "age parameter". While this formula was derived for electromagnetic showers, it can

be extended to hadronic cascades using a generalized form of the age parameter,

$$s = 3\left(1 + \frac{2\xi}{t}\right)^{-1}, \tag{1.21}$$

where ξ is a floating parameter to describe differences between the theoretical model of an electromagnetic shower and a hadronic shower. Experiments which sample the lateral density distribution of charged particles at discrete distances can determine the total number of charged particles in a shower from a fit of the NKG function (1.18) to the measured data. It should be noted that, while the electromagnetic component of an air shower is most abundant, its lateral density distribution falls more steeply than that of hadrons and muons. This leads to an enhancement of the relative abundance of hadrons and muons in the periphery of an air shower (see Fig. 1.6).

1.5. Air shower detection techniques

Since fluxes are too low, all experiments measuring cosmic rays in the knee region and beyond employ ground based detectors. The most commonly used techniques and some recent experiments will be summarized in this section, which is based on the review by Blümer et al. (2009).

1.5.1. Ground based particle detectors

The classic tool to detect extensive air showers are arrays of scintillators, which detect charged secondary particles at ground level. Most signals are created by electrons and positrons, and a few converted photons. Due to the large number of particles in an air shower, sparse arrays covering only a small fraction of the area are sufficient. From the lateral distribution of the density of charged particles, which can be fit for example with the NKG function (1.18), the location of the shower core, and the total number of charged particles in the shower can be determined. Using Monte Carlo simulations of air showers, the primary energy can be inferred from these quantities. The direction of the shower can be inferred from a measurement of the signal times.

In a similar fashion, secondary particles at ground level can be detected by arrays of water Cherenkov detectors. These consist of water or ice filled tanks, which detect the Cherenkov light emitted by relativistic charged particles traversing the detector medium. Because these detectors are relatively thick with a height of typically ~ 1 m (compared to a few centimeters in the case of scintillators), they can efficiently detect inclined or even horizontal air showers, leading to a larger acceptance than in the case of scintillator arrays. Additionally, the conversion probability of photons is increased so that photons, which constitute the majority of particles in an air shower, are detected more efficiently. More details will be

given in Chapter 2, where the IceTop detector is described, which makes use of this technique.

Often, such arrays are combined with additional particle detectors that are covered with an absorber of several radiation lengths, in order to suppress the electromagnetic component of air showers. Signals in these detectors are mostly due to muons and the measurements can be used to determine the primary mass, as discussed in the previous section. Alternatively, deep underground detectors can be used to measure high-energy muons, as in the combination of EAS-TOP and MACRO (Aglietta et al., 2004) or in the case of IceTop and IceCube (Ahrens et al., 2001).

1.5.2. Cherenkov and fluorescence light detection

Since an air shower consists of highly relativistic charged particles, about one third of all particles in the shower, most of them electrons and positrons, emit Cherenkov light in the forward direction. This light is emitted in a narrow cone, due to the maximum Cherenkov angle of about 1.3° at sea level. There are two kinds of detectors for Cherenkov radiation in the atmosphere.

Light integrating detectors are arrays of photomultiplier tubes facing upward to measure the lateral distribution of Cherenkov photons emitted by an air shower. This technique was pioneered by the AIROBICC experiment on La Palma. From a parametrization of the lateral distribution of Cherenkov light the primary energy and the shower age can be inferred. The latter allows to determine the primary mass.

The other method uses imaging telescopes to map the development of the shower by not only counting the number of Cherenkov photons arriving at the detector but also registering their arrival direction. This technique is most commonly used in TeV γ-ray astronomy, which will not be covered in this thesis.

A different approach uses imaging telescopes to measure the fluorescence light emitted by nitrogen atoms in the atmosphere. Nitrogen atoms in the atmosphere are excited by passing relativistic charged particles. In contrast to Cherenkov light, fluorescence light is emitted isotropically, allowing observation of the shower from the side from long distances Thus, a measurement of the longitudinal development of air showers above primary energies of 10^{17} eV is possible (at lower energies the fluorescence light yield is too low). This allows a direct determination of the shower maximum X_{max} and thus a determination of the primary mass. Furthermore, the energy measurement is calorimetric because the complete development of the air shower can be observed, albeit afflicted with a 15% systematic uncertainty on the calibration of the fluorescence light yield.

The disadvantage of both Cherenkov and fluorescence light measurements is that they can only be performed in clear moonless nights, which limits the duty cycle to roughly 10%.

1.5.3. Radio

Several mechanisms for the emission of radio-frequency electromagnetic radiation from air showers have been predicted theoretically. Radio emission from air showers has first been discovered experimentally in the 1960s. One possibility is the emission of coherent Cherenkov light by electromagnetic cascades, also known as the Askaryan effect. This is mostly effective in dense media. In the atmosphere, radio frequency waves can also be emitted by charged particles being deflected in the Earth's magnetic field. This is known as the geosynchrotron effect.

Different experiments to measure air showers using radio-frequency electromagnetic waves are currently being planned or in the prototype phase, for example at the site of the Pierre Auger Observatory (Blümer et al., 2009) or at the South Pole (Abbasi et al., 2011b). The quantitative description of radio emission has not yet been fully understood. Experimental difficulties include the triggering of radio arrays (Schröder, 2010).

1.5.4. Some recent experiments

Most of the techniques described above are currently used by various experiments to study cosmic rays in the energy range around the knee and above. In this subsection, a selection of a few experiments will be described.

KASCADE-Grande

The KASCADE-Grande experiment (Apel et al., 2010a) is the successor of KASCADE (KArlsruhe Shower Core and Array DEtector, Antoni et al., 2003), located near Karlsruhe in the valley of the river Rhine in Germany at 110 m a.s.l. This altitude corresponds to an average atmospheric depth of 1022 g/cm^2. KASCADE comprises 252 detector stations arranged on a square grid with 13 m spacing, covering an area of $200 \times 200\,\mathrm{m}^2$. Each station consists of a scintillator detector to detect all charged particles and an additional detector shielded by 10 cm of lead and 4 cm of iron to detect muons with a threshold of about 230 MeV. The central detector of KASCADE contains a hadronic calorimeter and underground muon detectors. In this part of the detector, muons can be measured at additional thresholds of 490 MeV, 800 MeV and 2400 MeV.

KASCADE-Grande extends the original array with 37 additional scintillator detector stations arranged on an irregular triangular grid with an average spacing of 137 m on a total area of about $700 \times 700\,\mathrm{m}^2$. In addition, eight scintillator stations (*Piccolo*) are used as a fast trigger of KASCADE in case the shower core is in the Grande area. KASCADE-Grande can reconstruct the shower core position with an accuracy between 5 and 8 m and the direction with an accuracy of up to 0.8°.

KASCADE-Grande also acts as a test bed for research and development of radio air shower detection (LOPES, Apel et al., 2010b).

IceTop and KASCADE-Grande have a similar detector spacing and size and thus cover a similar range of primary energies. The main differences are the altitude, detector technology and the detectable muon energies.

Tunka-133

The Tunka experiment (Antokhonov et al., 2010; Kuzmichev, 2011) is an air shower array in the Tunka Valley near lake Baikal in Siberia, at an altitude of 675 m a.s.l. Tunka is a light-integrating Cherenkov detector. In its current configuration it consists of 133 upward facing PMTs contained in 50 cm diameter metallic cylinders. The PMTs are arranged in 19 clusters which are arranged on a grid with 85 m distance between the clusters covering roughly $1\,\mathrm{km}^2$. The light integrating technique allows a good energy resolution of 15% and an angular resolution of 0.1 to 0.3°. A fit of the Cherenkov light lateral distribution allows the reconstruction of the shower core with an accuracy of 10 m. Furthermore it is sensitive to X_{max} with an uncertainty between 20 and $25\,\mathrm{g/cm}^2$ allowing a measurement of the primary composition.

GAMMA

GAMMA (Garyaka et al., 2008) is an air shower array located at Mount Aragats in Armenia at an altitude of 3200 m a.s.l. It consists of 33 plastic scintillator detectors at the surface, each with an area of $1\,\mathrm{m}^2$. They are arranged in five concentric circles with radii between 20 and 100 m. In addition, a densely instrumented "carpet" of $150\,\mathrm{m}^2$ of muon detectors is located below $2.3\,\mathrm{kg/cm}^2$ of concrete and rock in an underground muon hall. The energy threshold for muons of this installation is about 4 GeV. GAMMA determines zenith angles with an accuracy of 1.5° and achieves an energy resolution of 10 to 15% and a core resolution of about 1 m.

The basic detection principles of GAMMA are very similar to those of KASCADE and the arrays are similar in size. The main difference is the altitude, which in case of GAMMA is closer to that of IceTop.

Tibet-III

The Tibet air shower array is located at Yangbajing in Tibet, China, at an altitude of 4300 m a.s.l. (Amenomori et al., 2008). In its third stage of extension, it consists of 789 scintillator detectors, which are 3 cm thick and each have an area of $0.5\,\mathrm{m}^2$. They are covered with a 5 mm layer of lead in order to increase the sensitivity by converting photons in electromagnetic showers. In the main part of the array, detectors have a spacing of 7.5 m covering an area of $36\,900\,\mathrm{m}^2$. The 92 outer detectors have a spacing of 15 m. The high altitude allows for a very low energy threshold of only a few TeV. Above 100 TeV shower directions can be reconstructed with an accuracy better than 0.2°. The core resolution is 5 m and shower size

reconstruction accuracy is 5%. Tibet-III covers the primary energy range from 10^{14} to 10^{17} eV.

2. IceCube and IceTop

IceTop is an air shower array at the geographic South Pole and the surface component of the IceCube Observatory (Achterberg et al., 2006) shown in Fig. 2.1. It covers an area of 1 km^2 above the cubic kilometer IceCube neutrino telescope in the ice. Detector construction started in 2004 and was completed in December 2010.

2.1. IceCube and the IceTop air shower array

2.1.1. IceCube

The IceCube neutrino telescope uses roughly 1 km^3 of instrumented volume deep in the South Polar ice to detect charged particles via Cherenkov radiation. It consists of 4680 light sensors called Digital Optical Modules (DOMs, see section 2.1.3) on 78 strings between 1450 and 2450 m depth. The strings which each contain 60 DOMs are arranged on a triangular grid with a spacing of 125 m. Additionally, the central part of IceCube is instrumented with eight additional strings (Schulz, 2010). The 60 DOMs on these strings have a smaller spacing than on the other strings and are arranged at depths between 1760 and 2450 m with no modules between 1850 and 2100 m depth, where the optical properties of the ice are impaired by a layer of dust (Ackermann et al., 2006). This densely instrumented part is called DeepCore and has a significantly lower energy threshold than the rest of IceCube.

The main objective of IceCube is the detection of high-energy cosmic neutrinos. Neutrinos can be detected via the Cherenkov light produced by charged leptons created in charged current neutrino interactions. Because the ice at the depth of IceCube is very clear with absorption lengths of the order of 200 m, Cherenkov light can be detected at large distances from the particle track.

Besides high energy cosmic neutrino searches, IceCube is also sensitive to various kinds of new physics, such as magnetic monopoles, WIMPs, or Kaluza-Klein Dark Matter (Anchordoqui and Montaruli, 2010).

2.1.2. IceTop

The surface component of IceCube is the IceTop air shower array. It consist of 81 detector stations covering an area of 1 km^2 above the neutrino telescope in the ice. The stations are mostly located close to IceCube strings, except for three

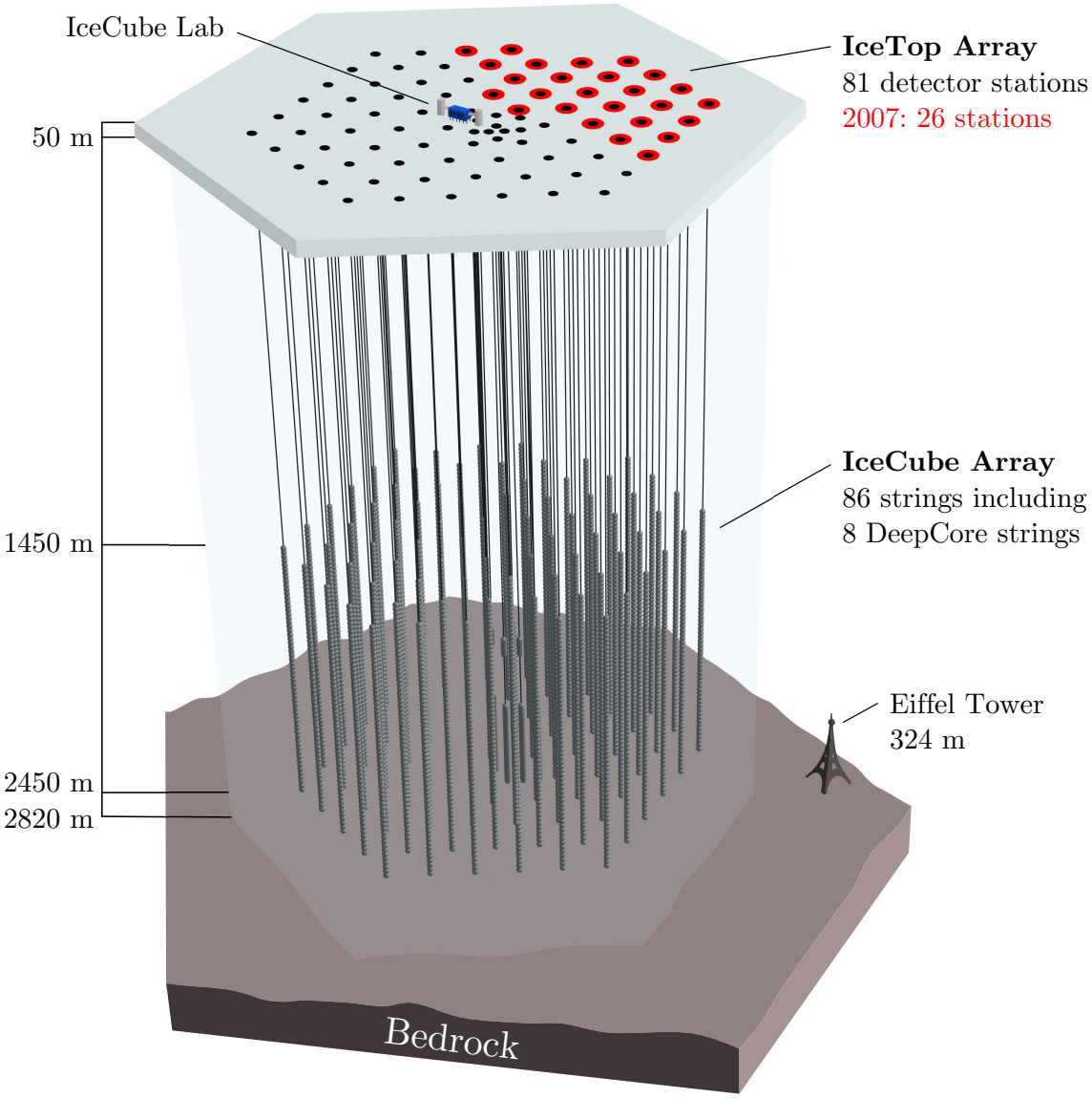

Figure 2.1.: The IceCube Observatory. The black dots at the surface indicate the locations of IceCube strings, and the locations of IceTop stations installed in 2007 are highlighted in red. The IceCube data acquisition systems are located in the IceCube Lab in the center of the array at the surface.

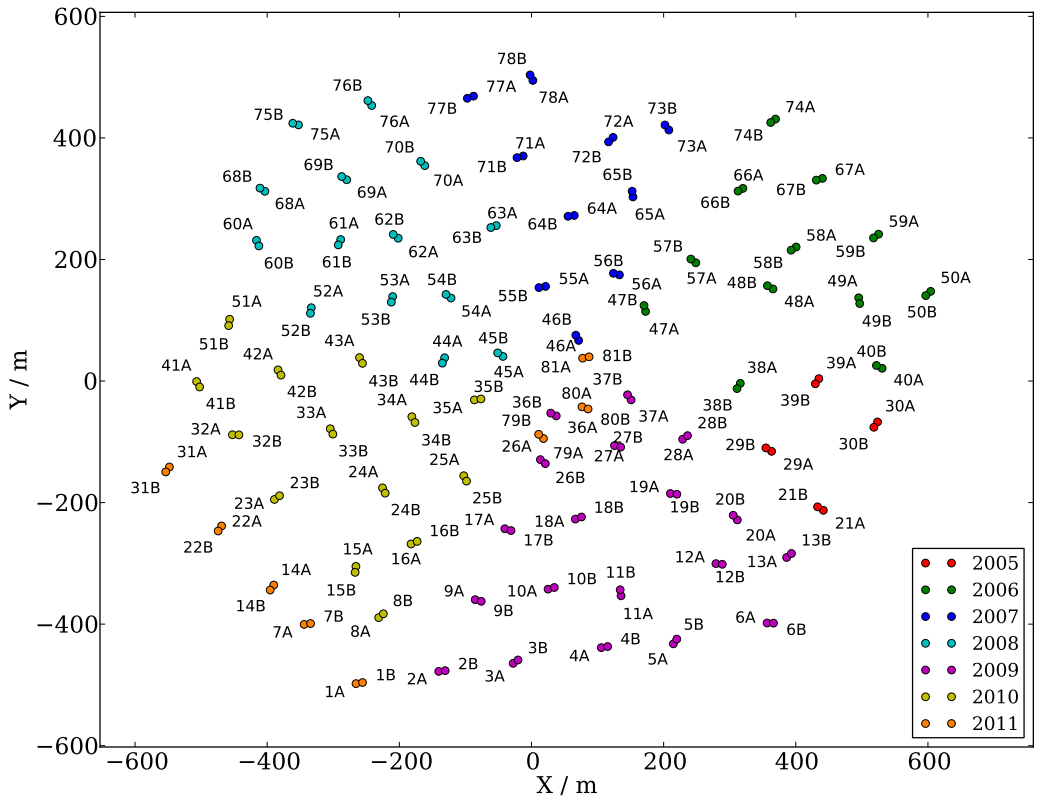

Figure 2.2.: Locations of IceTop tanks and their year of deployment. IceTop stations are located next to IceCube string and consist of two tanks, A and B. The irregularity of the array is due to practical reasons, because tank locations were constrained by surface cabling and IceCube drilling operations.

stations located at the center of the array with a smaller spacing, in order to lower the energy threshold. Each station consist of two ice filled tanks separated by 10 m to detect air shower particles using Cherenkov light created in the tanks' ice. Having two tanks per station makes air shower reconstruction more robust against signal fluctuations and allows a measurement of these fluctuations (Kislat, 2007). Figure 2.2 shows the locations of IceTop tanks and the year they were deployed.

IceTop is designed to detect air showers in the primary energy range between about 500 TeV and 1 EeV (Ahrens et al., 2001). Because of the thickness of the antarctic glacier, IceTop is located at an altitude of about 2835 m above sea level. This corresponds to an average atmospheric depth of 695 g/cm^2, which is close to the shower maximum in the energy range of interest — for proton showers at about 550 g/cm^2 at 1 PeV to 720 g/cm^2 at 1 EeV (Gaisser, 1990). Close to shower maximum, shower density fluctuations are smaller than at other stages of shower development. Furthermore, at shower maximum electromagnetic particles are most abundant, whereas only TeV muons are able to reach the deep IceCube

detector. Measuring coincident events in IceTop and IceCube, therefore, allows a good separation of the electromagnetic and the muon component of an air shower. The ratio of these two components is highly sensitive to primary mass (Gaisser, 1990) and thus allows a measurement of cosmic-ray composition.

The analysis presented in this thesis is based on data taken in 2007. At that time IceTop consisted of 26 stations, highlighted in red in Fig. 2.1, with a fiducial area of 0.218 km^2.

Figure 2.3 is a schematic sketch of the components of an IceTop tank. A tank has an inner radius of 91 cm and is filled with ice up to a height of 90 cm. In the final configuration of IceTop with 81 stations covering an area of 1 km^2, a fraction of $4.4 \cdot 10^{-4}$ of the fiducial area are thus covered with detectors. A tank is equipped with two Digital Optical Modules to detect Cherenkov light emitted by charged particles in the ice. The two DOMs are placed at the top of the ice facing downward, separated by 58 cm. The photomultiplier tubes inside the DOMs are operated at two different gains, in 2007 at $5 \cdot 10^6$ (high-gain DOMs) and $5 \cdot 10^5$ (low-gain DOMs[1]), to enhance the dynamic range. This results in a linear range for signals from 1 up to more than 10^5 photoelectrons. The DOMs on every IceCube string are numbered 1 to 60, with number 1 at the top of the string, while the IceTop DOMs are numbered 61 to 64, where 61 and 63 are high-gain DOMs.

In most tanks, the inner surface is coated with a diffusely reflective Zirconium liner, in order to increase the light yield at the photo tubes. Only the tanks of the first four stations deployed in the 2004/05 austral summer contain a Tyvek bag instead. The Tyvek has a larger reflectivity which results in a larger light yield, but also in an undesirable time stretch of pulses. On top of the ice, there is a 40 cm layer of perlite as a thermal insulation and to keep light from entering the tanks. The tanks are deployed in trenches, which are filled with snow after deployment, such that their tops are on equal level with the surrounding snow, as seen in the photograph in Fig. 2.4. This is done in order to protect the ice inside the tank from large temperature variations, and to avoid a pile-up of drifting snow.

An important goal of the deployment of IceTop is the creation of a large block of clear ice without air bubbles or cracks. To achieve this, after the tanks are filled, the water is being degassed and circulated continuously by a special device called Freeze Control Unit in order to remove dissolved gas. It takes about 50 days until the water in a tank is completely frozen.

2.1.3. Digital Optical Modules and data acquisition

Both in IceCube and IceTop, Cherenkov light is detected by so called Digital Optical Modules (DOMs, Abbasi et al., 2009). A DOM consists of a 10" Hamamatsu photomultiplier tube (PMT, Abbasi et al., 2010) and electronic circuitry, contained

[1] The gain of the low-gain DOMs was changed to 10^5 in 2008 in order to increase the dynamic range.

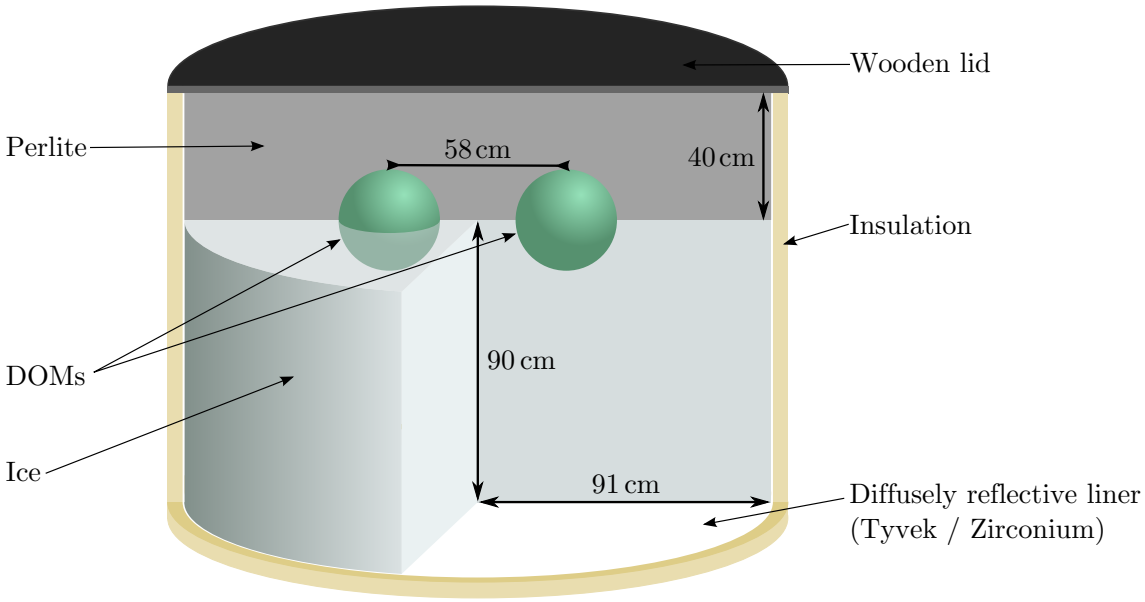

Figure 2.3.: Cross-section of an IceTop tank. It is filled with ice to a height of 90 cm, and two DOMs record Cherenkov light emitted in the ice.

Figure 2.4.: Photograph of an IceTop station. The tanks are deployed in a trench, which is backfilled with snow after deployment is complete, in order to avoid build-up of drifting snow. The metal frame on top of the tank will hold a sunshade during freezing and will later be removed.

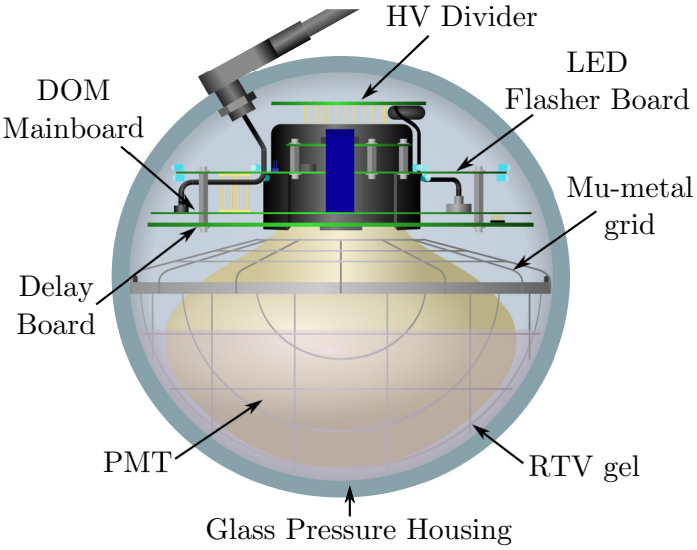

Figure 2.5.: Schematic of an IceCube Digital Optical Module.

inside a 32 cm glass pressure sphere, as shown in Fig. 2.5. The PMT is shielded from Earth's magnetic field by a mu-metal grid.

Data taking, triggering, digitization and communication with the surface are controlled by a FPGA (Field Programmable Gate Array) on the DOM mainboard with an embedded CPU, so that the DOM firmware can be updated remotely. Timing of the DOM is controlled by a free-running 20 MHz oscillator which is synchronized with the master clock in the counting house. In addition, the flasher board in a DOM is equipped with calibrated LEDs, used in studies of the optical properties of the deep ice. They are not used in IceTop. A detailed description of the Digital Optical Modules can be found in Abbasi et al. (2009).

Readout and digitization.

Readout of a DOM is triggered when the voltage at the PMT surpasses a programmable threshold. In IceTop, thresholds of all DOMs are optimized such that they correspond to a signal charge of about 23 pe (Waldenmaier, 2010). In order to capture part of the waveform before the actual trigger, signals are delayed by 75 ns before they reach the data capture electronics (but not before the trigger discriminator).

After triggering, the output of the PMT is sampled by a custom-made integrated circuit called 'Analog Transient Waveform Digitizer' (ATWD) in 3.3 ns wide bins for a total of 128 bins. This corresponds to a total sampling time of about 422 ns. Each ATWD has four channels, three of which are used for regular data taking. These three channels are equipped with pre-amplifiers of different gains, nominally 0.25, 2 and 16. To minimize dead-time, a DOM is equipped with two ATWDs which are used alternatingly. After the analog sampling, signals are

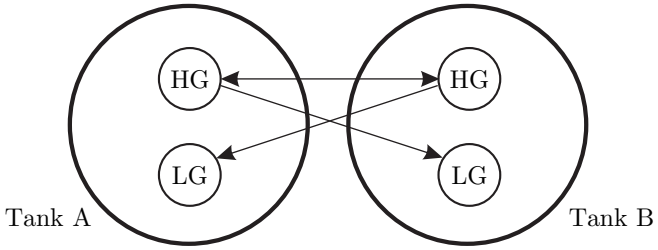

Figure 2.6.: Schematic of the Local Coincidence configuration in IceTop.

digitized with 10 bit precision. Due to the three different gain channels, a DOM has an effective resolution of 16 bits.

In parallel, signals are recorded and digitized continuously by an untriggered 10-bit fast analog-digital converter (fADC) at a rate of 40 MHz. The result is stored in a ring-buffer for 6.4 μs and is read out upon a trigger. This additional waveform information was not used in this analysis.

Local Coincidence and triggering.

The complete, digitized waveform is only transmitted to the surface, if the DOM receives a 'Local Coincidence' signal from a neighboring DOM within a ±1 μs time window around the trigger time. Otherwise, only a coarse charge and time stamp, called 'Soft Local Coincidence Hit' (SLC), is transmitted. The Soft Local Coincidence feature was only introduced in 2009 when data taking with the 59-string IceCube detector started. Therefore, SLC hits were not available in this analysis. The IceTop local coincidence condition requires a trigger of the high-gain DOM in the other tank of the station, as shown in Fig. 2.6 This implies, that station signals always consist of a pulse in the high-gain DOMs of both tanks, and optionally additional pulses in low-gain DOMs.

In the central counting house (IceCube Lab), events are then built from the individual DOM signals. An event is only stored permanently if one of several trigger conditions is met. For air shower physics, the IceTop Simple Multiplicity Trigger (SMT) is used, which requires 6 hits in IceTop DOMs within 6 μs. The readout window then starts 10 μs before the trigger window and lasts until 10 μs after the last of the 6 hits.

All triggered events were stored permanently on tape. However, IceCube standard data processing was only performed on a filtered subset of data which were transmitted via satellite to the central IceCube data storage in the north. In 2007, in order to save bandwidth, events with less than 16 participating DOMs[2] were prescaled by a factor of 5 by transmitting only every fifth event. In this analysis events with less than 16 DOMs, therefore, had to be weighted accordingly. Events with 16 or more DOMs were transmitted at a rate of 0.9 Hz and the smaller, prescaled events at a rate of 2.5 Hz.

[2]This was changed in 2008, requiring 8 full stations, instead of 16 DOMs.

Droop.

The high voltage circuits of the PMT are decoupled from the DOM mainboard using a wide-band pulse transformer (Abbasi et al., 2009). Droop is an undershoot of the waveform after large pulses caused by this transformer. Choosing the time constants of the transformer is a compromise between loss of precision in high-frequency signals, and droop after large signal amplitudes. The pedestals of the ATWD and fADC are set to ~10% of the maximum scale, to permit waveforms with below-baseline excursions.

The droop effect can be described by an impulse response with two time constants $\tau_{1,2}$ (Roucelle, 2007a),

$$\delta(t) \rightarrow \delta(t) - N\left((1-f)e^{-t/\tau_1} + f\,e^{-t/\tau_2}\right), \tag{2.1}$$

where N is a normalization constant. The droop constants f, τ_1, and τ_2 have been measured in the laboratory as a function of DOM temperature. This, in principle, allows to correct for the droop effect, which, however, was not done in IceTop. Droop is included in the detector simulation, though.

The transformers in DOMs deployed in the first 16 stations have short time constants leading to a strong droop effect (often referred to as "droopy" DOMs), whereas DOMs deployed later have larger time constants reducing droop ("non-droopy" DOMs).

Since droop was not corrected for in experimental data, it needs to be taken into account in simulation, where the same model (2.1) was used. However, since the droop constants are temperature dependent, and temperature variations at the South Pole throughout the year are significant (DOM mainboard temperatures vary between −20° C and −40° C throughout the year), this is a potential source of systematic error. While the tank calibration (see section 2.3.2) mitigates variations of the droop to some extent, a remaining systematic uncertainty had to be taken into account in the analysis.

2.1.4. Physics goals of IceTop

IceTop as an air shower experiment, can make use of the deep IceCube muon detector, forming a three-dimensional air shower array. Besides its cosmic ray physics program, it also serves as a veto and a source of calibration for IceCube.

Cosmic-ray energy spectrum.

Grid spacing and size of IceTop allow measurement of cosmic ray air showers in the energy range between about 500 TeV and 1 EeV. The lower limit is determined by the distance between stations, and will be even lower when making use of the more densely instrumented central part. Above 1 EeV event numbers will

be too small due to the steeply falling cosmic ray energy spectrum. The all-particle energy spectrum in this energy range has already been measured by several experiments. However, the measurements are not in good agreement, and systematic uncertainties are large (see Fig. 1.1). At the lower energy end, IceTop will have an overlap with direct measurements of balloon and satellite experiments. At high energies, it will overlap with experiments like Auger or HiRes.

In the energy range accessible to IceTop, a transition from galactic cosmic rays as the dominant component to extragalactic cosmic rays is expected. The well-established knee feature around 4 PeV is often associated with the cut-off of light components of galactic cosmic rays. A second knee is expected at the cut-off of the galactic iron component, and some measurements indicate the existence of this feature.

Every new measurement in this energy range with a new detector in a different location can help reducing systematic uncertainties and can verify or falsify general features of the spectrum. One of the goals of IceTop is a high statistics measurement of the all-particle cosmic ray energy spectrum, in order to scrutinize its features. In addition, measuring the all-particle energy spectrum and comparing the results to other experiments, is a good way to verify overall performance of the detector, data acquisition systems and reconstruction algorithms. This is particularly important at the early stage the IceTop experiment is still in.

Composition of cosmic rays.

The main goal of IceTop, is the determination of the primary mass composition as a function of energy. Measuring coincident events in IceTop and IceCube allows to separate high energy muons and electromagnetic component of air showers (Ahrens et al., 2001).

In interactions of heavy nuclei with the Earth's atmosphere, the pion multiplicity is higher than in proton-air interactions. The ratio between charged and neutral pions is the approximately independent of primary mass. Since this happens at high altitudes, where density is low, charged pions rather decay to muons than interact with air nuclei. This leads to a larger multiplicity of high energy muons for heavier primary nuclei.

Furthermore, the interaction cross section increases with the mass of the primary particle, and thus, the first interaction occurs at higher altitudes. In addition, to first approximation nuclei with mass A and energy E_0 can be considered as a superposition of A nucleons with energy E_0/A. Therefore, interactions of heavier primary particles lead to larger multiplicities and lower average energies of secondary particles. All of these effects lead to a faster development of air showers initiated by heavier primary nuclei. Thus, at detector level, air showers initiated by heavy primaries will be at a later stage of development ("older" showers), than those initiated by lighter particles ("younger" showers).

Therefore, the ratio between electromagnetic and muon component of an air

shower is highly sensitive to primary mass. Muon multiplicities have been used to determine primary mass in other experiments, like KASCADE, as well. However, muons at the surface are mostly muons in the GeV range created at later stages of shower development. IceTop is the first experiment that can make use of a km^3-scale underground muon detector to detect TeV muons from the first interactions. It, therefore, provides a systematically different way of measuring primary composition extending the measurements by EAS-TOP and MACRO into the PeV energy region.

Additionally, methods are being developed to detect muons in signals of the IceTop surface detectors (Lucke, 2008; Birr, 2010). These signals are caused predominantly by GeV muons. Furthermore, differences in shower development described above, can be exploited when comparing data obtained with the IceTop array from different zenith angles. This method has first been described by Klepser (2008), and is also used in this thesis.

Being able to measure cosmic ray composition in several, systematically independent ways, will allow a reduction of systematic uncertainties, and maybe even give input to the modeling of high energy cosmic-ray interactions.

Solar physics.

During solar flares, the sun emits particles in the MV to GV rigidity range. Due to the low geomagnetic cutoff at South Pole, IceTop is able to detect these particles. While air showers of such low energies will not trigger the IceTop array, some particles will still reach the ground. These trigger individual IceTop DOMs at high rates. Therefore, short term variations can be measured at a high statistical precision (Abbasi et al., 2008).

In addition to the discriminator used for the air shower trigger, each DOM contains a second discriminator that can be used for solar physics. Setting these additional discriminators to a range of different thresholds corresponds to different energy thresholds for the measurement of secondary particles. From these data, not only rates of particles emitted in solar flares, but also their energy spectrum can be inferred.

Particle physics.

Conventional muon bundles have a diameter of a few tens of meters, which is small compared to the string spacing of IceCube. Therefore, IceCube cannot distinguish individual muons in bundle. However, it is possible to separate individual muons with a high transverse momentum of several GeV from the bundle, if the separation between muon and muon bundle is larger than 150 m (Gerhardt et al., 2009). Such muons are typically produced in cosmic ray interactions, where heavy quarks are produced when a high-energy parton interacts with a nucleus of the atmosphere. Using IceTop to reconstruct the energy of the primary particle, and IceCube to measure the transverse momentum of the muon, the lateral

separation spectrum of muons can be measured in an energy range not accessible to current collider experiments.

Calibration and veto for IceCube.

In case of coincident events in IceTop and IceCube, the direction of the event can be reconstructed independently from the air shower and the muon bundle. Comparison of the two results can be used for cross-calibration of the directional reconstruction of the two sub-detectors (Ahrens et al., 2001).

Furthermore, IceTop can be used as a veto in neutrino searches. While standard neutrino analyses in IceCube use the Earth as a filter, this becomes inefficient when searching for neutrinos of PeV and higher energies, since their mean free path in Earth is shorter than the Earth's radius. In this energy range, neutrinos from above the horizon can be studied. The main background of such neutrino events are muon bundles from cosmic ray air showers. This background can, to some extent, be suppressed by using IceTop as a veto (Auffenberg, 2010; Berghaus, 2010).

2.2. Signals in the IceTop detector

Due to their thickness, IceTop tanks not only count charged particles but measure the energy deposited inside the tank volume, which depends on incident particle species and energy. Signal development in IceTop tanks has been studied in detail by several people (Klepser, 2008; Lucke, 2008; Melzig, 2011; Kislat et al., 2007) and the results will be summarized here.

The detection principle is based on the emission of Cherenkov light by relativistic charged particles. If a particle traverses a dielectric at a velocity $\beta c > c/n$ light is emitted coherently at an angle

$$\theta_c = \arccos \frac{1}{n\beta}. \tag{2.2}$$

Due to the refractive index of ice of $n \approx 1.3$ (Lide, 1967), the maximum Cherenkov angle is $\theta_{c,\max} \approx 40^\circ$ for highly relativistic particles, and the Cherenkov threshold energy in terms of particle rest mass m_0 is $E \approx 1.57\, m_0 c^2$. Because $\beta < 1$ the Cherenkov angle is $\theta_c < \theta_{c,\max}$ and therefore most light is emitted downward for a near vertical air shower.

Therefore, the Cherenkov light needs to be reflected by the bottom of the tank and the tank walls before it can be detected by the DOM. In fact, simulations showed that on average photons are reflected 6 times (in case of the Zirconium liner) before they reach a PMT (Lucke, 2008). Furthermore, based on the fact that waveforms measured in IceTop tanks have a characteristic decay time $\tau = 26.5\,\text{ns}$ (in case of Zirconium liner), one can estimate an effective absorption length

$$\lambda_{\text{abs,eff}} = \tau \frac{n}{c} \approx 26.5 \cdot \frac{1.3}{3.3}\,\text{m} = 10.4\,\text{m}. \tag{2.3}$$

Here, the time distribution of Cherenkov light emission was neglected, since a vertical particle traveling at the speed of light only needs about 3 ns to traverse a tank.

Due to their energy distribution, most muons registered in IceTop tanks are close to minimally ionizing (Nakamura et al., 2010). Thus, their energy loss is very continuous, without stochastic losses due to bremsstrahlung, and practically constant within a tank. Therefore, above their Cherenkov threshold the light yield of muons increases only very slowly with energy and it scales linearly with track length inside the tank. Even muons below their Cherenkov threshold are able to produce a small amount of light in the tank, for instance through δ-electrons and if they decay inside the tank, the decay electron can be above Cherenkov threshold.

Electrons and positrons, on the other hand, initiate electromagnetic showers inside the tank, which has a height in terms of radiation lengths of about

$$t = 90\,\text{cm}\,\frac{\rho_{\text{ice}}}{x_0} = 90\,\text{cm} \cdot \frac{0.92\,\text{g/cm}^3}{36.08\,\text{g/cm}^2} \approx 2.3 \tag{2.4}$$

with the density of ice of $\rho_{\text{ice}} = 0.92\,\text{g/cm}^3$ and the radiation length in water of $x_0 = 36.08\,\text{g/cm}^2$. This leads to a considerable energy dependence of the light yield of electrons. The same is true for photons. However, since they do not carry electric charge they have a chance of

$$p = \exp\left(-\tfrac{7}{9} \cdot 2.3\right) \approx 0.17 \tag{2.5}$$

in the high energy limit to pass the tank undetected. On the other hand, photons are the most abundant particles in air showers and therefore the dominant source of light in the tanks. A comparison of the light yield of muons and electrons as a function of energy can be found in Fig. 2.7.

Since the nuclear interaction length in water of $\lambda_I = 83.6\,\text{g/cm}^2$ (Nakamura et al., 2010) roughly corresponds to the column depth of a tank, roughly 63% of all nucleons will initiate hadronic showers. Therefore, the qualitative behavior of the light yield of nucleons is similar to that of electromagnetic particles. This means that IceTop tanks are also sensitive to neutrons.

2.3. Detector calibration

2.3.1. Calibration of DOM electronics and PMT

Calibration of PMT gain and electronic components of a DOM are performed by a software called 'DOM-cal' running on the DOM CPU (Achterberg et al., 2006)

during special calibration runs. In 2007, 15 DOM-cal runs were conducted.

Charge calibration.

The analog-to-digital converter of the ATWD in every bin in each signal channel is calibrated for both ATWDs, by varying the ATWD bias voltage and measuring the response. A linear fit is then applied to the resulting amplitudes.

The ATWD front-end amplifiers are then calibrated in a two-step process. First, the channel with the 16× pre-amplifier is calibrated by injecting artificial single photoelectron-like pulses, and comparing the measured pulse height to the known true pulse amplitude. The other channels are then calibrated consecutively relative to the highest-gain channel using light injected into the PMT with a LED. The gain of the next channel is then the ratio of the pulse integrals in the two channels times the gain of the previously calibrated channel.

Finally, the gain of the PMT is calibrated making use of electrons from beta decays of radioactive isotopes contaminating the glass pressure sphere. These electrons lead to a rate of single-photoelectron pulses. The charge distribution obtained from these pulses can be described by a Gaussian single-photoelectron peak and a contribution at low charges attributed to backscattering of the primary photoelectron at the first dynode leading to a reduced production of secondaries (Abbasi et al., 2010). The relation between high voltage setting and single-photoelectron peak is determined by varying the bias voltage between 1200 and 1900 V.

Timing calibration.

The master clock of the IceCube experiment is a GPS-controlled clock in the IceCube Lab. The local 20 MHz oscillator of each DOM is synchronized with this master clock in a procedure called "reciprocal active pulsing calibration" (RAPcal, Abbasi et al., 2009). This works by sending a precisely timed bi-polar pulse from the data acquisition system at the surface to the DOM, which responds after a fixed delay, by sending a pulse identical to the original pulse back to the surface. The one-way propagation time on the up to 3 km long cables can then be obtained from the roundtrip time and the known idle period. In this way a timing precision of 1 ns RMS or less can be achieved.

2.3.2. Calibration of the IceTop tanks

The methods described in the previous section allow a conversion of the ADC counts measured by the DOM into a number of photoelectrons. However, the detected charge is not comparable between different tanks, because the tanks have different optical properties. Therefore, signals created by near vertical muons are used to calibrate tanks in a uniform way, and tank signals are then expressed in terms of 'Vertical Equivalent Muons' (VEM).

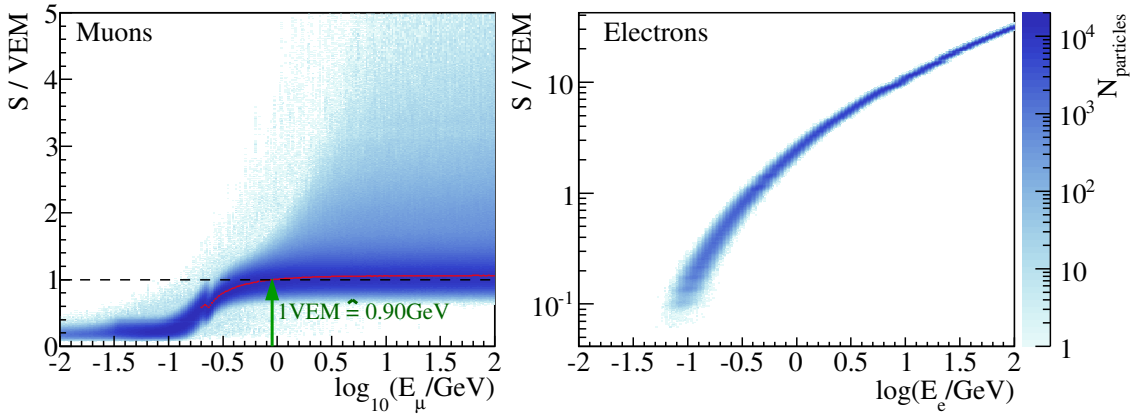

Figure 2.7.: *Left:* Simulation of the tank response to vertical muons with energies between 10 MeV and 100 GeV. A muon of $E_\mu = 900$ MeV generates an average signal of 1 VEM as defined in the VEM calibration procedure. The cut-off at low energies is due to the trigger threshold. The discontinuity around $\log(E_\mu/\mathrm{GeV}) = -0.6$ is a digitization artifact that has been removed in later versions of the simulation code. *Right:* Light yield of vertical electrons. Note the logarithmic vertical scale. In contrast to muons the amount of Cherenkov light produced by electrons and their secondary particles increases strongly with energy.

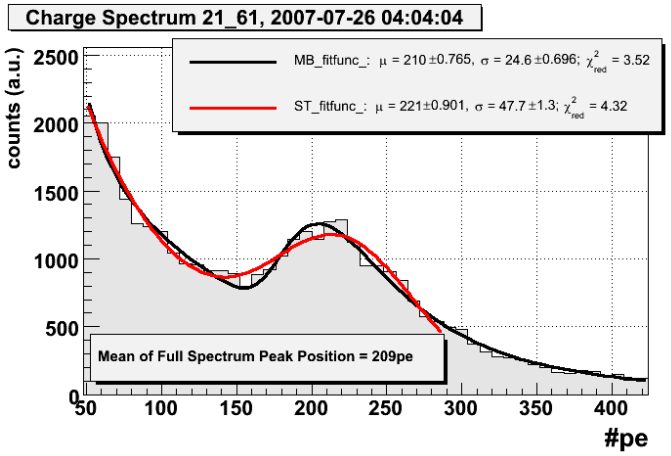

Figure 2.8.: Muon calibration spectrum of DOM 21-61, taken on July 26, 2007. Figure from Demirörs (2007).

This calibration was performed during special calibration runs, carried out roughly every two weeks[3]. During those runs all gains were set to 10^7 and no local coincidence was required. In this way, charge spectra were collected created by the natural spectrum of particles, energies and zenith angles. Since muons are highly abundant and the light they create per track length is almost constant they create a peak in these charge spectra. Figure 2.8 is the muon calibration spectrum of DOM 21-61 taken on July 26, 2007. The charge distribution from muons can be best described by a Landau peak due to vertical muons and a step function caused by 'edge-clipping' muons. On top of that, there is an exponentially falling background from electromagnetic particles (Beimforde, 2006). In 2007, two functions were used to fit the muon spectra (Demirörs, 2008). The first was the sum of an approximation of the Landau distribution for the muon peak, and two exponential functions to describe the electromagnetic background:

$$f_{\mathrm{MB}}(x) = \frac{p_0}{\sqrt{2\pi}\,p_2} \exp\left(-\frac{1}{2}\left(\frac{x-p_1}{p_2} + \exp\left(-\frac{x-p_1}{p_2}\right)\right)\right) + \exp(p_3 + p_4 \cdot x) + \exp(p_5 + p_6 \cdot x). \tag{2.6}$$

In the second function, the muon peak was assumed to be Gaussian, and the background was described by a single exponential function:

$$f_{\mathrm{ST}}(x) = p_0 \exp\left(-\frac{1}{2}\left(\frac{x-p_1}{p_2}\right)^2\right) + \exp(p_3 + p_4 \cdot x). \tag{2.7}$$

The muon peak position of each of these functions was determined numerically and the two values were averaged.

Measurements triggered with an external scintillator telescope placed on top of the tanks, which retricted the range of incident zenith angles to a maximum of about 17°, showed a 5% lower peak position. Therefore, 1 VEM was then defined as the number of photoelectrons that corresponded to 95% of the muon peak. This number corresponds to about 120 pe for the Zirconium lined tanks and 200 pe for the Tyvek bag tanks. Simulations showed that a vertical muon of 900 MeV energy creates a signal of 1 VEM, see Fig. 2.7. However, this relation is arbitrary since it depends on the definition of VEM, which includes the choice of fit functions (2.6) and (2.7) and the 95% scaling factor.

2.4. Environmental conditions at South Pole

Since cosmic ray measurements with IceTop use the Earth's atmosphere as a converter medium, variations of the atmosphere will affect air shower measurements.

[3]This procedure has been changed in 2009. Since then, muon calibration data are taken during normal data taking runs.

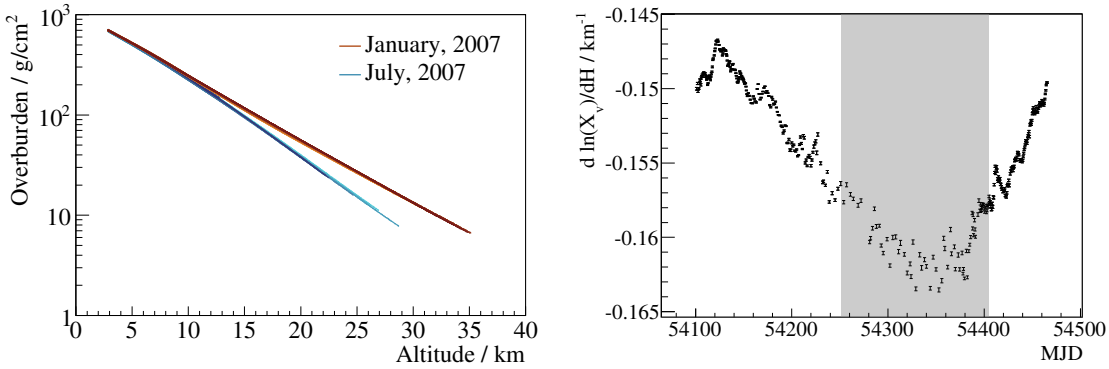

(a) (b)

Figure 2.9.: (a) Atmosphere profiles measured in the daily balloon soundings in January and in July 2007. (b) Slope of atmosphere profiles in 2007. A small $\mathrm{d}\ln(X_v)/\mathrm{d}H$ corresponds to a dense atmosphere. The gray shaded area indicates the time when the data using in this thesis were taken.

The South Pole atmosphere undergoes a pronounced annual cycle. In the winter months, May to October, when the sun is below the horizon, the air is much colder than in summer, with surface temperatures ranging from −20° C down to −70° C. Therefore, in winter the atmosphere is much denser than in summer, as can be seen in Fig. 2.9(a). To illustrate this cycle, the development of the slope of simple exponential fits of such atmosphere profiles throughout the year 2007 is shown in Fig. 2.9(b). The overburden $X_v(h)$ (see Eq. (1.11)) was determined from the air pressure $p(h)$ measured in the balloon flights as a function of altitude h:

$$X_v(h) = p(h)/g(h) \tag{2.8}$$

with the gravitational acceleration $g(h)$ at altitude h,

$$g(h) = G_N \frac{M_\oplus}{\left(R_\oplus^P + h\right)^2}, \tag{2.9}$$

where G_N is the gravitational constant, $M_\oplus = 5.974 \cdot 10^{24}\,\mathrm{kg}$ is Earth's mass, and $R_\oplus^P = 6.357 \cdot 10^6\,\mathrm{m}$ is the polar radius of the Earth.

In contrast to the strong annual variation of the density profile, there is no cyclic variation of ground pressure. Instead changes happen on a much shorter time scale, as seen in Fig. 2.10. The average atmospheric pressure at South Pole is about 680 hPa, in the time period studied in this thesis, the average pressure was 681.0 hPa. An increase in air pressure leads to a stronger attenuation of air showers, which in turn increases the energy threshold of IceTop. Accordingly, event rates are anti-correlated to air pressure, which is clearly seen for the rate in

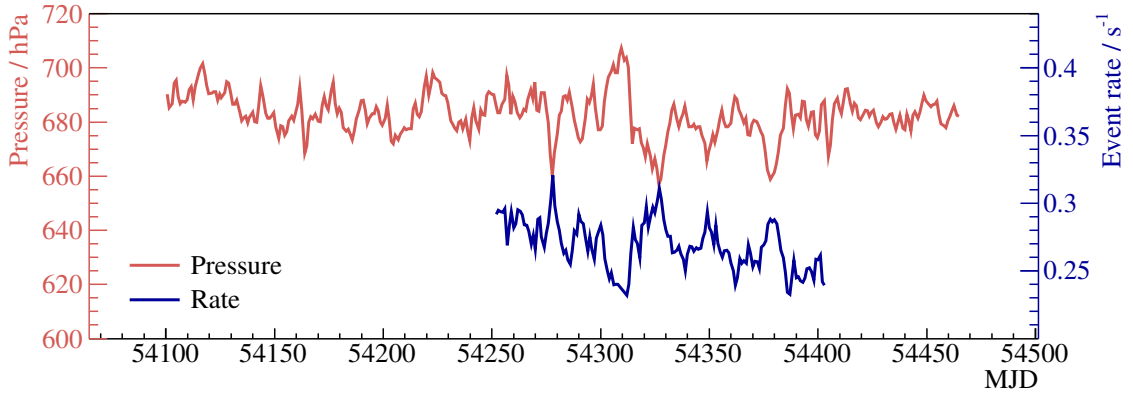

Figure 2.10.: Ground pressure at South Pole between January 1 and December 31, 2007, compared to the event rate in the final event sample used in this thesis. Pressure and rate are clearly anti-correlated.

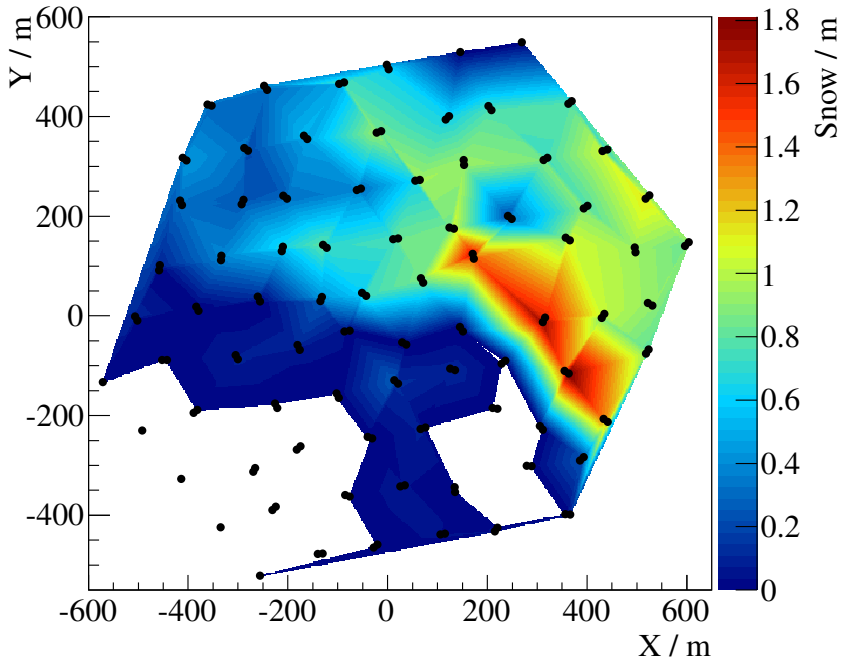

Figure 2.11.: Distribution of snow heights on top of IceTop tanks measured in January, 2011, and interpolated between tanks.

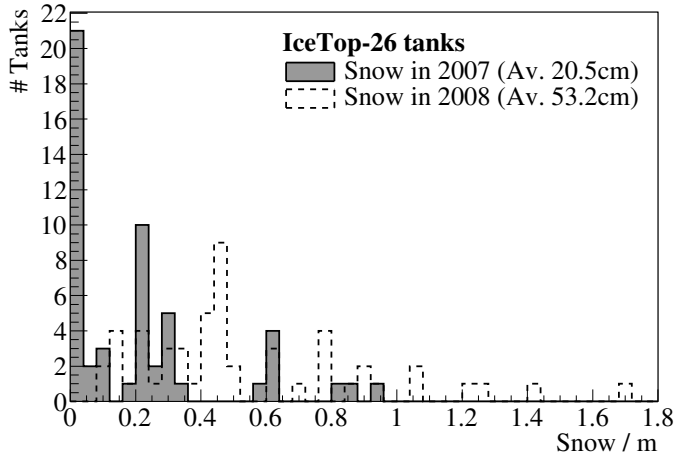

Figure 2.12.: Snow heights on top IceTop tanks of the first 26 stations in January 2007 and January 2008. Within one year the average snow height increased from 20.5 cm to 53.2 cm.

the final sample of this thesis shown in the figure.

An additional decrease of the event rate throughout the measurement period can be observed. It has no counterpart in the pressure development and is most likely due to the accumulation of snow on top of IceTop tanks. While precipitation at South Pole only amounts to about 2 cm per year, there is a significant amount of snow accumulation due to drift. On average, the snow height on top of the tanks increases by 20 cm every year. However, accumulation strongly depends on surrounding terrain and buildings. Katabatic air flows lead to a relatively constant wind with an average speed of 10 kts (in 2007) from one predominant wind direction. This causes an increased accumulation of snow leeward of buildings and slopes. Figure 2.11 shows the distribution of snow on top of IceTop stations in January, 2011.

In January 2007, there were on average 20.5 cm of snow on top of IceTop tanks (see Fig. 2.12). The 10 newly deployed stations were free of snow. On top of most other stations there were between 20 and 30 cm of snow, apart from 4 stations close to buildings with 60 to 90 cm snow height.

Measurements of snow depths are only made once per year. By January 2008, the average snow depths on top of the 26 stations operated in 2007 had increased to 53.2 cm. Assuming constant growth, the average snow depth in August 2007, in the middle of the time when data used in this thesis were taken, can be estimated to be 39 cm.

Depending on depth, the snow has a density of 0.35 to 0.4 g/cm^3. Thus, 20.5 cm correspond to about 1.2% of the total atmospheric depth. While muons are practically unaffected by snow, electrons and photons lose energy in it (Melzig, 2011). This leads to an effective attenuation of air shower signals, with an attenuation length of about 1.5 m (Andeen, 2011b).

3. Air shower reconstruction

3.1. Dataset and data selection

3.1.1. Run selection

The analysis in this thesis is based on IceTop data taken between June 1 and October 31, 2007, comprising IceCube data taking runs 107973 to 109628. In this analysis only those runs were used that fulfilled the following quality criteria, according to the official IceTop good run list (Tilav, 2007):

- No IceTop DOMs failed or encountered any problems such as unusual or unstable rates during the run or were missing entirely in the run configuration. In 2007, there were no permanently disabled IceTop DOMs.
- Trigger and filter rates after pressure correction were stable and within ±5 % agreement with the previous good run. Pressure correction was done by fitting the relation between ground pressure p and rate R with an exponential function, $R(p) \sim \exp(-\beta p)$, yielding a barometric coefficient $\beta = 0.0077/\text{mbar}$ (Tilav et al., 2009). Then, rates were corrected to the average South Pole ground pressure of 680 mbar:

$$R_{\text{corrected}} = R \exp\Big(\beta\,(p - 680\,\text{mbar})\Big). \tag{3.1}$$

- In addition, specifically for this analysis, run durations were required to be 30 min or longer. A normal data taking run lasted 8 hours, and nearly all runs that were aborted after a short time encountered some kind of problem.

In total, 527 runs containing data from $3.5 \cdot 10^7$ triggered IceTop events fulfilled these criteria.

3.1.2. Pulse extraction

A typical waveform recorded by IceTop is shown in Fig. 3.1. In the first step of data processing recorded ADC counts are converted to voltages using the calibration data acquired during the DOM-cal runs. From the three ATWD channels the one with the highest unsaturated gain was chosen. Then, the baseline of the waveform (horizontal blue line), determined by averaging the voltage in bins 83 to 123 (highlighted part of the baseline), was subtracted. This baseline can be

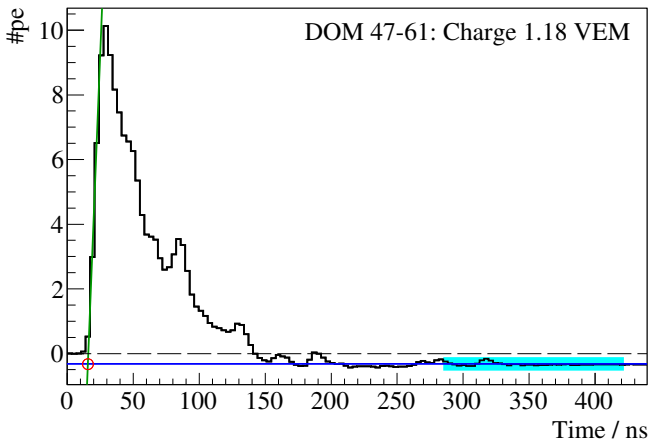

Figure 3.1.: Example of an IceTop waveform calibrated to photo electrons per nanosecond. Indicated in the figure are the baseline (horizontal blue line), the range of bins from which baseline is determined (highlighted in cyan), 'leading edge' (green line), and pulse time (red circle).

substantially below zero due to droop. Finally, the integrated charge of the waveform was converted to VEM, in this example waveform $S = 1.18\,\mathrm{VEM}$. The pulse time was determined from the 'leading edge' by extrapolating the largest increase of the waveform between adjacent bins before the maximum (green line) of the waveform to the baseline, indicated by the red circle.

In case both high and low gain DOM of a tank triggered, the charge from the low gain DOM was used if the charge in the high gain DOM surpassed a threshold determined during VEM calibration in order to avoid saturation. The pulse time was always taken from the high gain DOM.

3.1.3. Event cleaning and retriggering

Event cleaning. Before further processing events were cleaned based on a few simple checks. In case both DOMs of a tank triggered, the tank signal was rejected, if the time difference between the two pulses was greater than 40 ns. Furthermore, a maximum time difference between signals in tanks A and B of

$$|t_A - t_B| < \frac{|\boldsymbol{x_A} - \boldsymbol{x_B}|}{c} + 200\,\mathrm{ns} \tag{3.2}$$

was required. Here, $\boldsymbol{x_{A,B}}$ and $t_{A,B}$ are position and signal time of tank A and B, respectively. Finally, stations were grouped in clusters, such that any pair of stations i and j in the cluster fulfilled the condition

$$|t_i - t_j| < \frac{|\boldsymbol{x_i} - \boldsymbol{x_j}|}{c} + 200\,\mathrm{ns}. \tag{3.3}$$

The station position $\boldsymbol{x_i}$ is the center of the line connecting its two tanks, and t_i is the average time of the tank signals. In each event, only the largest cluster of stations was kept. The time tolerance of 200 ns in both cases was introduced to allow for fluctuations of the shower front and shower front curvature. This selection was done in order to remove obviously unrelated pulses from events. It only affects about 4% of events, where on average 2.3 tanks are removed.

Charge-based retriggering. In order to reduce uncertainties due to the description of the detector threshold in Monte Carlo, all pulses were retriggered to a common threshold based on registered charge. This step was motivated by a discrepancy of charge thresholds between experimental and simulated data discussed in Section 4.6.2. All pulses with a charge below $S_{\text{thr}} = 0.3\,\text{VEM}$ were removed, and afterwards the local coincidence conditions (see Section 2.1.3) were re-evaluated, discarding all pulses that no longer fulfilled this condition. This procedure was applied to both experimental and simulated data.

3.1.4. Event selection and livetime

For further processing, $N_{\text{tot}} = 8\,895\,205$ events were selected where at least five stations had triggered. Events which fulfilled this condition but had less than 16 DOMs read out were reweighted in the analysis according to the prescale factor of 5 (see Section 2.1.3). For each selected event the shower was reconstructed and further cuts were applied, based on the reconstruction results, as described in Section 3.4.

The effective livetime was calculated by fitting the distribution of time differences between events, Δt, with an exponential function,

$$N(\Delta t) = N_0 \exp(-\Delta t/\tau). \tag{3.4}$$

The selected runs have a total effective livetime of

$$T = N_{\text{tot}} \cdot \tau = (3274.0 \pm 1.9)\,\text{hours}, \tag{3.5}$$

which corresponds to 89.4 % of the selected 153 days period. The statistical uncertainty on the livetime was included in the statistical error of the resulting flux.

3.2. Likelihood reconstruction of air showers

From the signals measured by IceTop, the following properties of an air shower can be determined using a likelihood fit:

- zenith and azimuth angles θ and ϕ;

- shower core position $\boldsymbol{x}_c$;
- and shower size S_{ref} at reference radius R_{ref}.

In general, shower size and core position are determined from the lateral distribution of measured charges, and the shower direction is determined from signal times. The air shower reconstruction procedures used by IceTop have mainly been developed by Klepser (2008).

3.2.1. Lateral distribution function

IceTop tanks are not only sensitive to the number of charged particles, but also detect photons. Furthermore, the signal generated by a particle when it traverses the tank also depends on incident particle energy and direction (see Section 2.2). Therefore, the NKG function (1.18) is not appropriate to describe the lateral signal distribution in IceTop tanks. Instead, the signal charge expectation value in an IceTop tank at distance R from the shower axis can be described by an empirical lateral distribution function found in Monte Carlo simulations:

$$S(R) = S_{\mathrm{ref}} \cdot \left(\frac{R}{R_{\mathrm{ref}}}\right)^{-\beta-\kappa\log(R/R_{\mathrm{ref}})} . \tag{3.6}$$

For the logarithm of the signal, $\log S(R)$, this is a second order polynomial in $\log(R)$:

$$\log S(R) = \log(S_{\mathrm{ref}}/\mathrm{VEM}) - \beta\log\left(\frac{R}{R_{\mathrm{ref}}}\right) - \kappa\log^2\left(\frac{R}{R_{\mathrm{ref}}}\right). \tag{3.7}$$

This function behaves unphysically at distances $R \lesssim 1\,\mathrm{m}$, since it has a maximum at a radius of this order, whose exact location depends on the parameters of the shower. However, as discussed later in Subsection 3.2.3, all pulses that are closer to the core than 11 m were removed during the fit procedure.

The free parameters of this lateral distribution function are:

- the shower size S_{ref} at reference radius R_{ref};
- the slope of the lateral distribution function $-\beta$ at R_{ref};
- and the curvature parameter κ.

Parameter κ was fixed to the value 0.303, as determined in Monte Carlo simulations, and it was verified that this does not impair reconstruction quality. Primary mass and energy dependence of κ are still to be studied, and making it a free parameter might improve reconstruction quality at high energies, especially for the full configuration of IceTop. Thus, the lateral distribution function depends explicitly on two parameters, S_{ref} and β, and implicitly on four more parameters, namely the shower core position (x_c, y_c) and direction θ and ϕ, because R depends on these values.

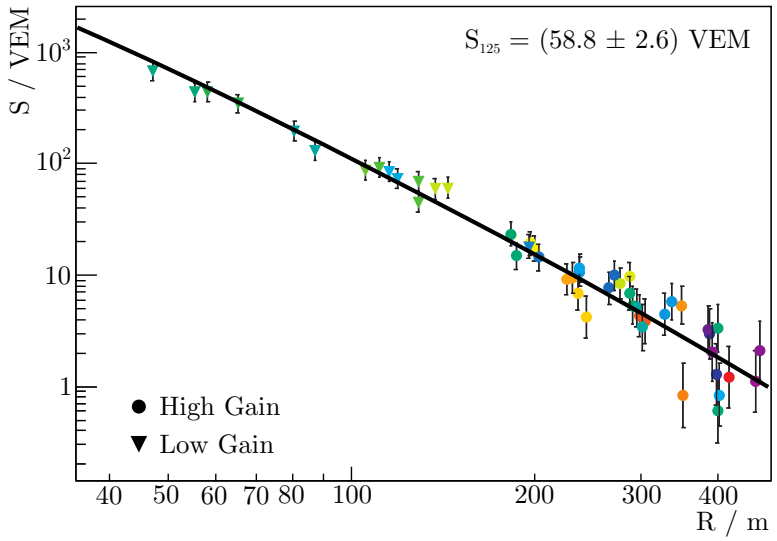

Figure 3.2.: An example of a lateral fit. Each point corresponds to the signal measured in an IceTop tank. The horizontal axis represents the distance to the reconstructed shower axis. The colors represent signal times with red corresponding to early and blue to late pulses.

For a given shower geometry, the fit of (3.7) can approximately be considered equivalent to a linear least squares fit of a straight line (details on the likelihood function are covered in Subsection 3.2.3). For a fixed core position and shower direction, R_i are constant and because κ is also constant in the fit, one can define

$$y_i = \log S_i + \kappa \log^2\left(\frac{R_i}{R_{\text{ref}}}\right). \tag{3.8}$$

Thus, the lateral distribution function can be rewritten as:

$$y_i = \log S_i + \kappa \log^2\left(\frac{R_i}{R_{\text{ref}}}\right) = \log S_{\text{ref}} - \beta \log\left(\frac{R_i}{R_{\text{ref}}}\right). \tag{3.9}$$

The covariance of S_{ref} and β is then:

$$\text{cov}(S_{\text{ref}}, \beta) = \frac{\sum_{i=1}^{N} \log(R_i/R_{\text{ref}})/\sigma_i^2}{\left(\sum_{i=1}^{N} \log(R_i/R_{\text{ref}})/\sigma_i^2\right)^2 - \sum_{i=1}^{N}\left(\log^2(R_i/R_{\text{ref}})/\sigma_i^2\right)\sum_{i=1}^{N} 1/\sigma_i^2}. \tag{3.10}$$

It vanishes if

$$\log R_{\text{ref}} = \frac{1}{\sum_{i=1}^{N} \frac{1}{\sigma_i^2}} \sum_{i=1}^{N} \frac{1}{\sigma_i^2} \log(R_i), \tag{3.11}$$

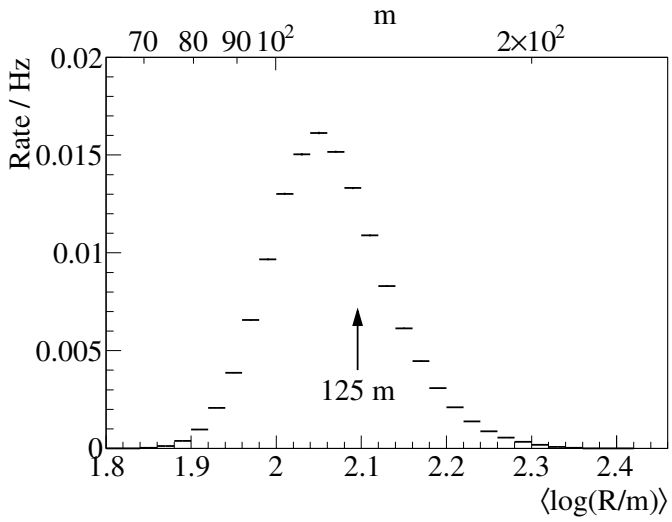

Figure 3.3.: Mean logarithm of radii of pulses participating in the lateral fit for showers in the given dataset with $S(R = 125\,\mathrm{m}) \geq 1\,\mathrm{VEM}$.

which in the case of constant $\sigma_i = \sigma$ corresponds to

$$\log R_{\mathrm{ref}} = \frac{1}{N} \sum_{i=1}^{N} \log R_i = \langle \log R \rangle. \tag{3.12}$$

The distribution of $\langle \log R \rangle$ of showers with $S(R = 125\,\mathrm{m}) \geq 1\,\mathrm{VEM}$ in the given dataset is shown in Fig. 3.3. In order to minimize the correlation between S_{ref} and β, the reference radius was fixed at $R_{\mathrm{ref}} = 125\,\mathrm{m}$, which is close to the peak position in the figure. This value was first suggested by Ochab (2007) based on a study of fit stability, in which IceTop was split into two sub-arrays consisting only of A and B tanks of the IceTop stations, respectively.

Figure 3.2 shows an example lateral fit of an event that triggered 25 stations. The reconstructed shower size was $S_{125} = (58.8 \pm 2.6)\,\mathrm{VEM}$.

3.2.2. Description of the shower front

Zenith and azimuth angle θ and ϕ of an air shower can be reconstructed from the arrival times of tank signals. These are determined by the shower direction and the geometrical shape of the shower front. In the reconstruction used in this thesis expectation values of signal times were parametrized as

$$t(\boldsymbol{x}) = t_0 + \tfrac{1}{c}(\boldsymbol{x_c} - \boldsymbol{x}) \cdot \boldsymbol{n} + \Delta t(R) \tag{3.13}$$

with

$$\Delta t(R) = a\,R^2 + b\left(\exp\left(-\frac{R^2}{2\,\sigma^2}\right) - 1\right). \tag{3.14}$$

Here, t_0 is the time, at which the shower core reaches ground, where ground is defined as the $\sqrt{S}$-weighted average of participating tank altitudes. Furthermore, $\boldsymbol{x_c}$ is the core position on the ground, and $\boldsymbol{n}$ is the unit vector in shower direction. Δt is the time residual with respect to a plane perpendicular to the shower axis through $\boldsymbol{x_c}$.

The form (3.14) of $\Delta t(R)$ and the constants

$$a = 4.823 \cdot 10^{-4}\,\mathrm{ns/m^2}, \qquad b = -19.41\,\mathrm{ns}, \quad \text{and} \quad \sigma = 83.5\,\mathrm{m} \tag{3.15}$$

were determined in a study of experimental data (Waldenmaier, 2007) and were not varied in the fit. Energy and mass dependence of these parameters remain to be studied and provide the possibility for further improvement of reconstruction quality and sensitivity to parameters of the primary particle.

The fit of signal times consequently had five free parameters:

- shower arrival time t_0;
- shower direction θ and ϕ;
- and core position (x_c, y_c).

3.2.3. The likelihood fit

The objective of the likelihood reconstruction is to find a set of parameters (S_{125}, β, t_0, $\boldsymbol{x_c}$, θ, ϕ) that best describe the measured data given the model functions described in the previous subsections. Given a set of parameter values, the likelihood function L describes the probability to measure the given set of data points. In an iterative procedure this function is maximized with respect to the model parameters. This is conventionally done by minimizing $\mathcal{L} = -\ln L$ to improve numerical stability.

The negative log-likelihood function for IceTop air shower reconstruction consisted of three terms,

$$\mathcal{L} = \mathcal{L}_S + \mathcal{L}_0 + \mathcal{L}_t. \tag{3.16}$$

The first term,

$$\mathcal{L}_S = -\sum_i \frac{(\log S_i - \log S_i^{\mathrm{fit}})^2}{2\,\sigma_S^2(S_i^{\mathrm{fit}})} - \sum_i \ln\Big(\sigma_S(S_i^{\mathrm{fit}})\Big), \tag{3.17}$$

describes the probability to measure the tank signals S_i given the expectation values S_i^{fit} at the tank locations determined by the lateral distribution function (3.6). The sums run over all tanks that triggered. A normal distribution with standard deviation σ_S of $\log S_i$ around the expectation value is assumed, as determined in a study of signal fluctuations in experimental and simulated data, see next

subsection. The second term in $\mathcal{L}_S$ accounts for the normalization of the log-normal distribution of charges. This is necessary, since σ_S depends on the charge expectation value, and to correctly normalize the three terms in Eq. (3.16).

The next term of the log-likelihood function (3.16),

$$\mathcal{L}_0 = -\sum_j \log\left(1 - (P_j^{\text{hit}})^{2-\xi}\right), \tag{3.18}$$

accounts for all stations that did not trigger, over which the sum runs. The probability that a tank in station j did not trigger is given by

$$P_j^{\text{hit}} = \frac{1}{\sqrt{2\pi}\,\sigma_S(S_j^{\text{fit}})} \int_{\log S_{\text{thr}}}^{\infty} \exp\left(-\frac{(\log S_j - \log S_j^{\text{fit}})^2}{2\,\sigma_S^2(S_j^{\text{fit}})}\right) \mathrm{d}\log S_j. \tag{3.19}$$

The lower integration limit was determined by the charge threshold, which was fixed to $S_{\text{thr}} = 0.3\,\text{VEM}$ through the retriggering described in subsection 3.1.3. In the analysis, the signal expectation value S_j^{fit} was evaluated for each station at the center of the line connecting its two tanks. The power of the hit probability in (3.18), $2 - \xi$, with $0 \leq \xi \leq 1$, depends on the degree of correlation of signal fluctuations in the tanks of a station. There is a natural correlation of the tanks due to the similar signal expectation values, but assuming that their signal fluctuations are uncorrelated, $\xi = 0$ was chosen. This, of course, is an approximation, and the possible systematic error introduced through this assumption is discussed in Section 6.3.1.

The third term in (3.16) describes the probabilities to measure the given signal times,

$$\mathcal{L}_t = -\sum_i \left[\frac{(t_i - t_i^{\text{fit}})^2}{2\,\sigma_t^2(R_i)} - \ln\left(\sigma_t(R_i)/\text{ns}\right)\right]. \tag{3.20}$$

Here, t_i are the measured signal times, $t_i^{\text{fit}} = t(R_i)$ is the signal time expectation value at the radius of tank i according to (3.13), and σ_t are radius dependent RMS time fluctuations found in experimental data (Waldenmaier, 2007),

$$\sigma_t(R) = 2.92\,\text{ns} + 3.77 \cdot 10^{-4}\,\text{ns} \cdot (R/\text{m})^2. \tag{3.21}$$

The second term in (3.20) is again a normalization term, similar to that in $\mathcal{L}_S$.

3.2.4. Charge fluctuations

Fluctuations of signal charges have been studied in detail, both in experimental and simulated data. To study signal fluctuations in experimental data, signals measured in the two tanks of a station were compared. In simulation, two different approaches were used. In one study, the full IceTop array was simulated, and,

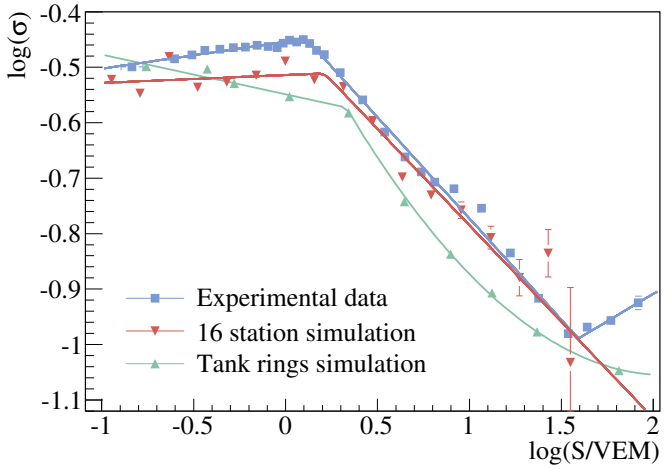

Figure 3.4.: Fluctuations of signal charges measured in experimental and simulated data (Kislat, 2007). In the analysis, the parametrization obtained from the 'tank rings' simulation was used.

like in experimental data, charges in the two tanks of a station were compared. In the second Monte Carlo study, tanks were arranged on circles, with shower cores at the center of this idealized array. Charges were found to be log-normally distributed around their expectation values, with the standard deviation shown in Fig. 3.4, taken from the ring-shaped array simulation (Kislat, 2007):

$$\sigma_S(S) = \begin{cases} 0.283 \cdot (S/\mathrm{VEM})^{-0.072} & S < 2.13\,\mathrm{VEM} \\ 10^{-0.372-0.661\log(S/\mathrm{VEM})-0.160\log^2(S/\mathrm{VEM})} & 2.13\,\mathrm{VEM} \le S < 119\,\mathrm{VEM} \\ 0.0881 & 119\,\mathrm{VEM} \le S \end{cases}. \tag{3.22}$$

Agreement between simulated and experimental data is acceptable. The flattening below 1 PeV is a truncation effect introduced by the trigger threshold. Signals fluctuating downward in this charge region will no longer trigger the tank, and therefore local coincidence will no longer be fulfilled.

3.2.5. Fit procedure

Starting from a seed for the seven air shower parameters, the negative log-likelihood function (3.16) was minimized using an iterative numerical procedure. Initial values for shower direction, core position and arrival time were determined using analytic first guess methods described in the next section. An initial value for S_{125} was determined from the measured tank signals S_i,

$$\log(S_{125}^{\mathrm{start}}/\mathrm{VEM}) = \sum_i \left[\log(S_i/\mathrm{VEM}) + \beta \log\left(\frac{R_i^{\mathrm{start}}}{125\,\mathrm{m}}\right) + \kappa \log^2\left(\frac{R_i^{\mathrm{start}}}{125\,\mathrm{m}}\right) \right], \tag{3.23}$$

where R_i^{start} is the distance of tank i from the shower axis determined in first guess reconstructions. For β, an empirically determined average value of $\beta^{\text{start}} = 3$ was used as the seed.

Starting from these numbers the global minimum of $\mathcal{L}$ with respect to the air shower parameters was found in several steps using the MINUIT program. In the first step, only the parameters S_{125}, β, and core position of the lateral charge distribution (3.6) were fitted, fixing shower direction and time t_0. Then, all pulses that were closer than 11 m to the reconstructed core position were removed and the minimization was repeated. This was iterated until no more pulses were removed. The rationale behind this step was that very large pulses tended to unnaturally attract reconstructed core positions. Removing these pulses resulted in a flatter distribution of reconstructed cores.

In the next step, t_0 and shower direction (θ, ϕ) were freed and S_{125}, β, and core position (x_c, y_c) were restricted to ±3 standard deviations around their best fit values from the first step. Both lateral charge and time distribution were fitted.

In the final iteration, t_0, θ and ϕ were fixed again, and all other parameters released. Only β remained limited to $1.5 \leq \theta < 5$.

3.3. First guess methods

To determine initial values for core position and shower direction, simple, analytical first guess algorithms were used.

3.3.1. Core center-of-gravity

As a starting value for the position of the shower core, the center-of-gravity of tank pulses, defined as their $\sqrt{S}$-weighted average position was used:

$$\boldsymbol{x}_{\text{COG}} = \frac{\sum_i \sqrt{S_i}\,\boldsymbol{x}_i}{\sum_i \sqrt{S_i}}. \tag{3.24}$$

The sums run over all tanks. In the likelihood fit, the z-coordinate of the shower core remained fixed to the value obtained in this calculation. It varied by about 3 m, corresponding to the variation of tank altitudes in the 26-station IceTop array.

For larger configurations of IceTop it turned out that air shower reconstruction can be improved by limiting the number of tanks that actually contribute in the calculation to the 7 tanks with the largest signal (Feusels, 2010).

3.3.2. Plane fit

To determine initial values for t_0 and shower direction, a plane perpendicular to the shower axis moving in the direction of the air shower at the speed of light was

fitted to the signal times. This is a linear least squares problem that can be solved analytically. The χ^2 is given by

$$\chi^2(n_x, n_y, t_0) = \sum_i \frac{\left(t_i - t_0 + (n_x x_i + n_y y_i)/c\right)^2}{\sigma_i^2}, \tag{3.25}$$

with the unit vector $\boldsymbol{n} = \left(n_x, n_y, -\sqrt{1 - n_x^2 - n_y^2}\right)$ in direction of movement of the shower. The sum runs over all tank signals with times t_i, positions (x_i, y_i), and time uncertainties $\sigma_i = \sigma = 5\,\text{ns}$.

This calculation was performed in two iterations. In the first step, all tanks were assumed to be at the same altitude. Then, a correction for tank altitude,

$$t_i^{\text{corrected}} = t_i + \frac{z_i - \langle z \rangle}{c} \cos\theta \tag{3.26}$$

with the average tank altitude $\langle z \rangle$ was performed, and the calculation was repeated using these corrected signal times.

3.4. Event selection

Based on the reconstruction results, several cuts were applied in order to guarantee a good reconstruction quality in the final event sample.

- The slope parameter β had to be in the range $2.0 \leq \beta < 4.5$ because most events with a value of β outside this range were badly reconstructed. The removed events had predominantly small shower sizes with $S_{125} < 1\,\text{VEM}$ corresponding to primary energies $E \lesssim 1\,\text{PeV}$, as is apparent from Fig. 3.5.

- The reconstruction uncertainty on the core position had to fulfill

$$\sigma_c = \sqrt{\sigma_x^2 + \sigma_y^2} < 20\,\text{m}, \tag{3.27}$$

  where σ_x and σ_y the fit errors of the core position (x_c, y_c). This cut removes the tail of most badly reconstructed events and affects only about 7% of events with $N_{\text{station}} > 5$.

- Both, reconstructed core and center-of-gravity core position (3.24) had to be 50 m inside the array boundary. Furthermore, it was required that the station with the largest signal was not on the border of the array. The array boundary was defined by the polygon through the stations at the corners of the array. This containment cut defines a fiducial area of

$$A_{\text{cut}} = 1.22 \cdot 10^5\,\text{m}^2. \tag{3.28}$$

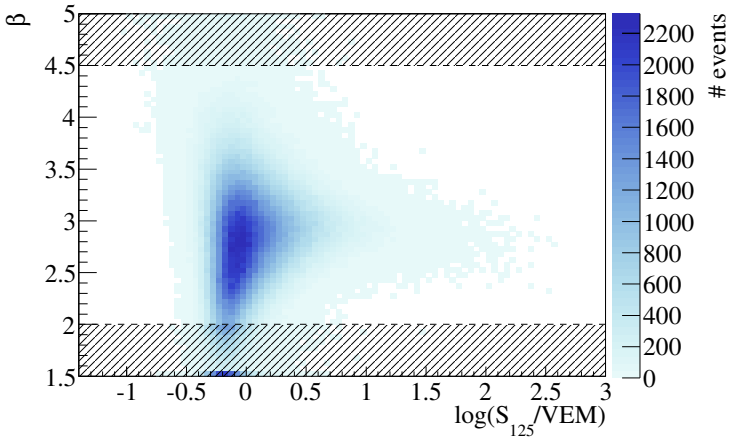

Figure 3.5.: Distribution of β as a function of shower size S_{125}. The shaded regions were removed by the cut $2 \leq \beta < 4.5$ (see text). Most of the removed events had a shower size $S_{125} < 1$ VEM.

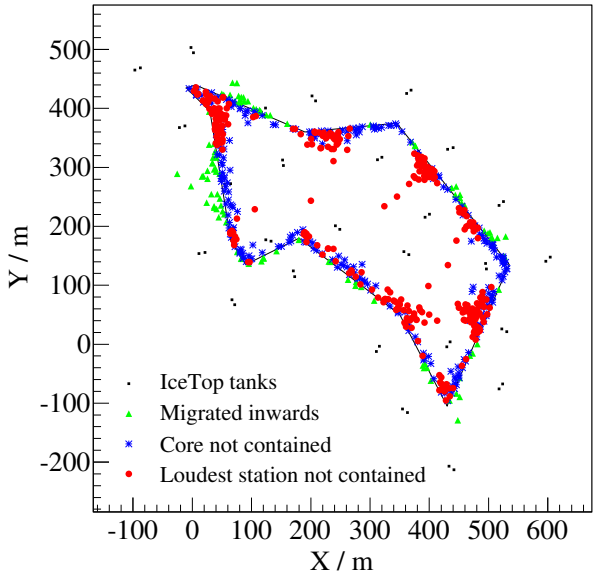

Figure 3.6.: Effect of containment cut on simulated air showers. Shown are the true core positions of showers whose reconstructed core position or center-of-gravity (3.24) was not contained (blue stars) inside the cut area (black line), or where the station with the largest signal ('loudest station') was on the border of the array (red circles). Furthermore, showers outside the cut area that passed all cuts due to a bad core reconstruction are shown as green triangles. The small black dots represent the IceTop tanks.

The effect of these conservative containment criteria on simulated air showers is illustrated in Fig. 3.6.

Passing rates for these cuts and differences between experimental and simulated data will be discussed in Section 4.7.

3.5. Shower size spectra

The main primary energy related shower property used in this analysis was the shower size S_{125}. Shower size spectra were obtained from data in three zenith angle ranges, equidistant in $\sec(\theta)$:

$$\Omega_1 : 0^\circ \leq \theta < 30^\circ, \qquad \Omega_2 : 30^\circ \leq \theta < 40^\circ, \quad \text{and} \quad \Omega_3 : 40^\circ \leq \theta < 46^\circ. \tag{3.29}$$

Given the atmospheric depth of IceTop of about 690 g/cm^2, a shower with a zenith angle of 46° traverses a slant depth of 993 g/cm^2 before reaching IceTop. This almost corresponds to detection at sea level in case of vertical incidence.

Rates were calculated as

$$\frac{\mathrm{d}^6 N}{\mathrm{d}\log S_{125}\,\mathrm{d}A_\perp\,\mathrm{d}\Omega\,\mathrm{d}t} = \frac{\sum_{i=1}^{N} w_i}{\Delta\log S_{125}\cdot A_{\mathrm{cut}}\,\frac{1}{2}(\cos\theta_{k,1}+\cos\theta_{k,2})\cdot 2\pi\,\Delta\cos\theta\cdot T}, \tag{3.30}$$

where $A_\perp$ is the area in the plane perpendicular to the shower axis. Furthermore:

- $w_i = 5$ for events that triggered less than 16 DOMs, and $w_i = 1$ for all larger events;
- $\Delta\log S_{125} = 0.05$ is the bin width;
- A_{cut} is the fiducial area according to Eq. (3.28);
- $2\pi\,\Delta\cos\theta = 2\pi(\cos\theta_{k,1} - \cos\theta_{k,2})$ is the solid angle of zenith angle range Ω_k;
- $\theta_{k,1}$ and $\theta_{k,2}$ are the angles limiting zenith angle range Ω_k;
- and T is the livetime according to Eq. (3.5).

Figure 3.7 shows the results. In the top row all showers with $\theta < 46^\circ$ were used and in the bottom row showers were divided into the three zenith angle ranges defined in Eq. (3.29). Fluxes in more inclined zenith angle ranges appear lower than in steeper ones because inclined showers are attenuated by the additional overburden and therefore the spectra are shifted toward lower values of S_{125}.

On the right-hand side of Fig. 3.7, the same spectra are shown weighted with $S_{125}^{1.5}$. In this representation a feature is visible in the range $1.4 \lesssim \log S_{125} \lesssim 2$, which is not compatible with the assumption of a single power law. The "bump"

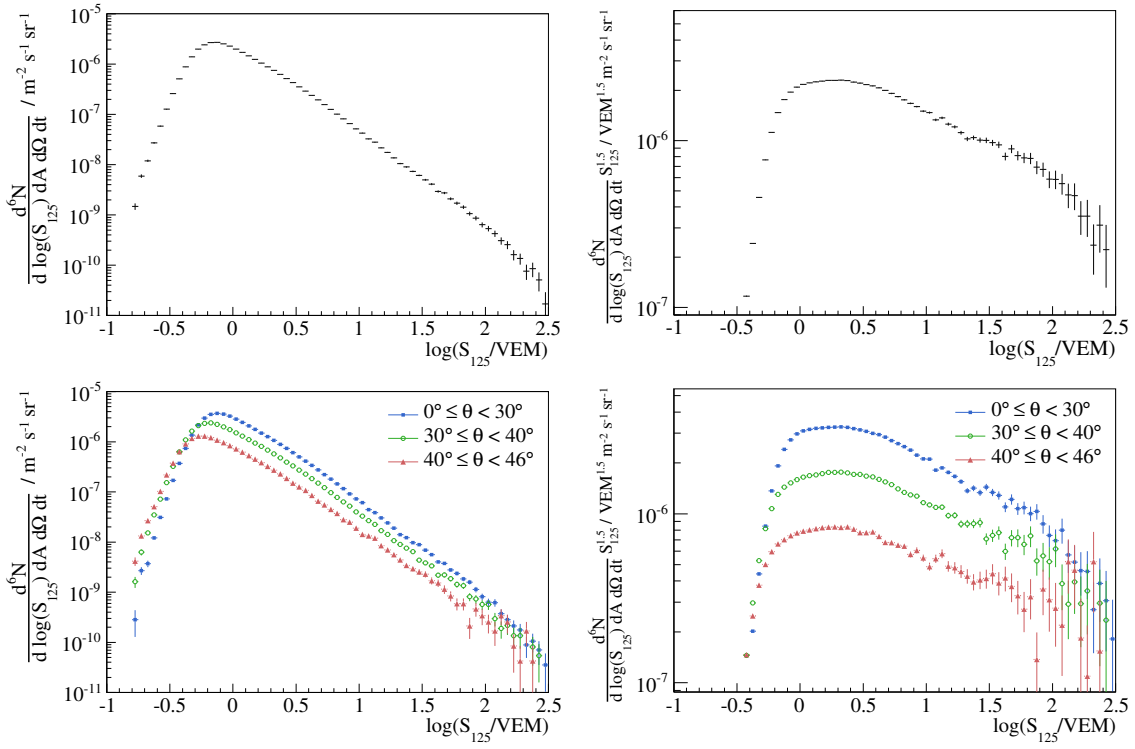

Figure 3.7.: *Top left:* Shower size spectrum obtained from showers with reconstructed zenith angles $0° \leq \theta < 46°$. *Top right:* The same spectra as on the left weighted with $S_{125}^{1.5}$ in order to existing features visible. *Bottom row:* Shower size spectra as above but split into three zenith angle intervals defined in Eq. (3.29).

is visible in the spectrum from all zenith angles as well as the individual spectra from different zenith angle intervals, although it is not very significant in the more inclined ranges due to lack of statistics.

For a simple comparison, the spectra from the different zenith interval in the range $0.5 \leq \log S_{125} < 2.0$ were fit with power laws. These yielded the following spectral indices α_k in the zenith ranges Ω_k:

$$\alpha_1 = -1.884 \pm 0.005, \qquad \alpha_2 = -1.849 \pm 0.009, \quad \text{and} \quad \alpha_3 = -1.818 \pm 0.018. \tag{3.31}$$

Spectra obtained in steeper zenith angle ranges have a larger spectral index than those from more inclined showers. This can be explained by the fact that for higher energy showers the shower maximum is closer to the detector level, leading to less attenuation of showers with increasing slant depth. Additionally, the zenith angular behavior is influenced by primary composition and a change in composition can have an impact on the spectral indices in different zenith angle ranges.

The S_{125} threshold decreases with increasing zenith angle. This is a simple geometrical effect: S_{125} is measured at a distance of 125 m to the shower core in a plane perpendicular to the shower axis. In this frame, distances between stations are decreased by a factor of $\cos\theta$, allowing smaller showers to pass the 5 station requirement.

4. Simulation of air showers and the IceTop detector

Air showers are complex processes, and therefore one has to rely on Monte Carlo simulations in order to relate measured air shower parameters to properties of the primary particle. First, the physical events, i. e. the air showers, were simulated using the software package CORSIKA (Heck et al., 1998). The output is a list of secondary particles at ground level, which were then fed into a detailed simulation of the IceTop detector.

4.1. Air shower simulations with CORSIKA

CORSIKA was used to simulate the development of air showers in the atmosphere. Hadronic interactions with an energy in the laboratory frame above 80 GeV were simulated using SIBYLL 2.1 (Fletcher et al., 1994, 1999), and FLUKA 2008.3 (Fassò et al., 2005; Battistoni et al., 2007) was used for lower energies. The electromagnetic component of air showers was simulated using the EGS code (Nelson et al., 1985).

CORSIKA offers the possibility to reduce computing time and storage requirements by a process called thinning. During the simulation, particles below a certain threshold are only tracked with an energy dependent probability and are then given an appropriate weight. Thinned air showers need special treatment in order not to introduce artificial fluctuations. Since these studies were not yet available, thinning was not applied in this thesis.

In total, about $3 \cdot 10^5$ proton and iron induced air showers with primary energies following an E^{-1} spectrum between 100 TeV and 100 PeV were simulated. In addition, smaller samples of intermediate mass primaries, ${}^{4}_{2}\mathrm{He}$, ${}^{7}_{14}\mathrm{N}$, and ${}^{14}_{28}\mathrm{Si}$, were produced. The reason for choosing iron as the heaviest nucleus is twofold. On the one hand all nuclei heavier than iron are believed to make only a minor contribution to the total flux, on the other hand, there is a technical limitation in the CORSIKA program which does not allow simulation of heavier primaries. Zenith angles were sampled according to

$$\mathrm{d}N \propto \cos\theta \sin\theta \, \mathrm{d}\theta \tag{4.1}$$

up to $\theta = 56°$, which is ideal for the simulation of a flat detector like IceTop and an isotropic flux (see Section 4.5).

Particles were tracked until they either reached the observation altitude of

Table 4.1.: Cutoff energies for particle tracking in CORSIKA. Particles were tracked until they either reached the detector plane or their energy was below the cutoff given in the table.

Particle type	Cutoff energy [GeV]
$e^{\pm}$	0.01
γ	0.002
$\mu^{\pm}$, hadrons	0.05

2835 m above sea level, or their energy dropped below a cutoff energy that depended on particle type. The cutoff energies were chosen based on a simulation study of particle light yield in IceTop tanks (Kislat et al., 2007), and correspond to the energy below which particles would not create any light in a tank according to these parametrizations. The cutoff energies are listed in table 4.1.

The atmosphere model in CORSIKA consists of 78.1% N_2, 21.0% O_2 and 0.9% Ar. The atmospheric profile was modeled according to a parametrization of the atmosphere of July 1, 1997, based on the MSIS-90-E model (Hedin, 1991, CORSIKA atmosphere model 12). This model has a total atmospheric overburden at the altitude of IceTop of 692.9 g/cm^2, which is close to the average overburden during data taking (690.7 g/cm^2), and its profile is that of a South Pole winter atmosphere.

The magnetic field was set according to the International Geomagnetic Reference Field (IGRF, Finlay et al., 2010) to an average value between June and October 2007 for a location 89° 59′ South[1] on the prime meridian at an elevation of 2835 m. This lead to the following components of the magnetic field[2]:

$$\begin{aligned} \text{Horizontal:} &\quad 16.59\,\text{nT} \\ \text{Vertical:} &\quad -52.79\,\text{nT} \end{aligned}$$

and an angle of −119° between detector x-axis which points toward Grid East[3] and magnetic north (i. e. the direction to the arctic magnetic pole). The negative sign of the vertical component means that the magnetic field lines point upward, since they point away from the antarctic magnetic pole.

For systematic checks, small samples of air showers were simulated using the high energy interaction models QGSJET-II (Ostapchenko, 2006a,b) and EPOS 1.99 (Werner et al., 2006). Furthermore, one dataset using CORSIKA atmosphere parametrization 13 (October 31, 1997), was produced. This parametrization has a total overburden of 704.4 g/cm^2, and its profile corresponds to the transition

[1] The IGRF parametrization fails to compute magnetic fields at 90° South.

[2] Calculated using the web interface at `http://www.ngdc.noaa.gov/geomagmodels/IGRFWMM.jsp`

[3] At South Pole, directions are given in grid coordinates, where Grid North points along the prime meridian toward Greenwich and Grid South in the opposite direction.

period between winter and summer. Unfortunately, none of the atmosphere models in CORSIKA has a lower overburden than the true average.

4.2. High-energy hadronic interaction models

One of the most problematic sources of systematic error in the analysis of air showers is the modeling of high-energy hadronic interactions. There are several reasons for this. Most importantly, the highest-energy cosmic ray interactions cannot be achieved by man-made colliders (of course, LHC will significantly extend the available energy range). Another important problem is that the results from proton-proton collisions at collider must be extrapolated to proton-Air or nucleon-Air interactions. Furthermore, interactions with pion projectiles play an important role. Physical models are employed to extrapolate experimental results to higher energies (Anchordoqui and Montaruli, 2010).

Scattering amplitudes are usually determined in the eikonal approximation and total cross-sections are calculated using the optical theorem. The main difference between models comes from the ansatz that is used for the eikonal function. An important role in this respect plays the assumed parton distribution in the plane perpendicular to the collision axis. In QGSJET a Gaussian profile function is used. SIBYLL, on the other hand, bases the transverse density on the Fourier transform of the proton electric form factor, which leads to a harder form factor. This leads to smaller particle multiplicities in the case of SIBYLL, which in air shower simulations mostly influences the number of muons at the detector level. In both of these models, energy conservation is only taken into account after determining the number of elementary interactions. Hadronization is based on string fragmentation models.

In EPOS, a different approach is chosen. As in SIBYLL and QGSJET, the number of elementary interactions is fixed from the scattering amplitude. However, energy conservation is taken into account at the parton level (Pierog, 2008). Additionally, hadronization is not based on string fragmentation but a statistical approach.

While the total cross-section predicted by the used models is relatively similar, multiplicities start to diverge above around 100 TeV primary energies. QGSJET predicts the highest multiplicities and EPOS the lowest ones.

4.3. Resampling

The simulated air showers were sampled on a circular area of 1200 m radius around the center of the 26-station IceTop array. This area proved large enough to allow for an accurate determination of effective area even at the highest energies, as shown in Fig. 4.1.

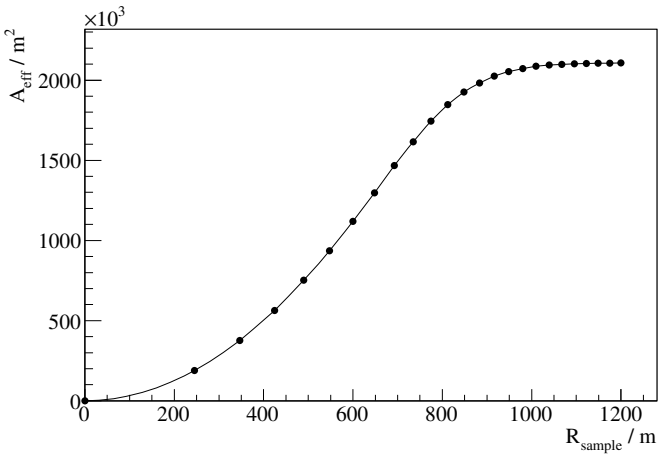

Figure 4.1.: The effective area determined from Monte Carlo simulations of 100 PeV proton showers, as a function of the radius of the sampling area. In this study no containment was required. After applying the containment cuts (see Section 3.4) the systematic error on the effective area due to the limited sampling area will be even smaller because the cuts very efficiently discard events outside the detector area (which is much smaller than the sampling region).

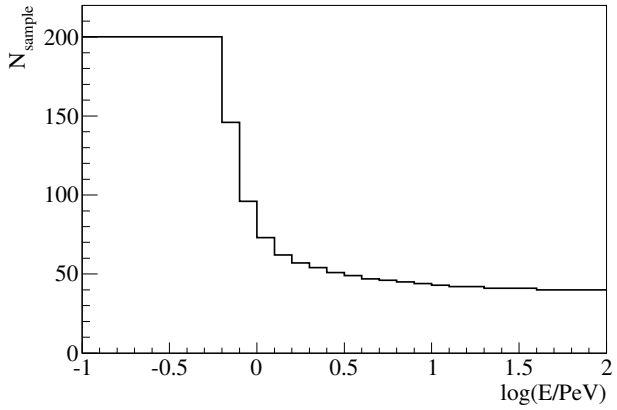

Figure 4.2.: Ideal resampling number in each primary energy bin, determined such that showers would appear once in the final sample. The number of resamplings was limited to 200 times.

In order to increase simulation efficiency and because shower simulation took much longer than detector simulation, every shower was sampled several times inside this sampling area. The number of samples was chosen for each primary energy bin (there were 10 bins per decade in energy) such that on average a shower would only appear once in the final sample (i. e. after applying the cuts described in Section 3.4) in order to avoid unnatural fluctuations. However, it was limited to at most 200 samples. At low energies, only showers with a larger-than-average size will trigger the array, while others will not. Therefore, the average number of times a showers is in the final sample in that regime is strongly decreased by those showers that do not trigger at all, whereas others could remain in the final sample too often.

The resulting numbers are shown in Fig. 4.2. They were determined resampling a subset of proton showers 200 times each. Using the same numbers for iron induced showers should be safe since their shower size for a given primary energy is in general smaller than proton induced showers as will be shown later.

4.4. Simulation of the IceTop detector

Detector simulation started with the simulation of the light yield inside the IceTop tanks, taking the secondary particles output by CORSIKA as input. Then, the PMT, DOM electronics, and trigger were simulated. Calibration constants (e. g. VEM calibration, single photoelectron calibration, and ADC calibration) and detector status information such as PMT gains were the same as those used in experimental data on August 8, 2007. The output format of the simulation was identical to experimental data, and the same reconstruction procedures and quality cuts as in experimental data were applied.

4.4.1. Simulation of IceTop tanks

The amount of light detected by a DOM when particles traverse IceTop tanks was simulated using Geant4 (Agostinelli et al., 2003; Allison et al., 2006). The IceTop tank simulation is described in detail by Melzig (2011). It included simulation of all physical processes inside the ice, tank material, snow surrounding the tanks, and the air above them (the CORSIKA simulation stopped above the snow). However, Cherenkov photons were not tracked through the ice of the tank to the DOMs, but only the number of emitted Cherenkov photons was calculated in order to save CPU time. The number of emitted Cherenkov photons was calculated by integrating

$$\frac{\mathrm{d}N}{\mathrm{d}x} = 2\pi\alpha z^2 \int_{\lambda_1}^{\lambda_2} \left(1 - \frac{1}{n^2\beta^2}\right) \frac{\mathrm{d}\lambda}{\lambda} \tag{4.2}$$

along the tracks of charged particles. Here, α is the fine structure constant, z and β are the charge of the particle and its velocity, and $n = 1.32$ is the refraction index of ice. The integral runs over the sensitive range of the PMTs, $\lambda_1 = 300\,\mathrm{nm}$ and $\lambda_2 = 650\,\mathrm{nm}$. The actual number of Cherenkov photons was then drawn from a Poisson distribution with mean value given by Eq. (4.2). Using Geant4 simulations that included full Cherenkov photon tracking, it was shown that the number of detected photoelectrons is proportional to the number of emitted Cherenkov photons, independent of particle type, energy, incident position, and direction (Melzig, 2011).

The arrival times of Cherenkov photons were distributed according to an exponential function after their emission. The time constants are different for Tyvek ($\tau_{\mathrm{Tyvek}} = 42.0\,\mathrm{ns}$) and Zirconium lined tanks ($\tau_{\mathrm{Zirconium}} = 26.5\,\mathrm{ns}$) due to the different reflectivities of the liners (see Section 2.1.2). These numbers were optimized in order to match the waveform shapes observed in experimental data (Lucke, 2008).

The IceTop tanks were modeled as a cylindrical plastic container with an inner diameter of 1.86 m and a wall thickness of 5 mm. For snow and ice, pure H_2O with a density of $0.38\,\mathrm{g/cm^2}$ and $0.92\,\mathrm{g/cm^3}$, respectively, was used. The DOMs were modeled as 33.02 cm diameter glass spheres, filled with an effective DOM material consisting of SiO_2 with a density of $0.2\,\mathrm{g/cm^3}$. On top of the ice, there was a 40 cm thick layer of perlite, which was modeled as a mixture of 92.92% air and 7.08% perlite, due to the granularity of the material. The chemical and physical properties of perlite were taken from the manufacturer's description[4]. The tanks were surrounded by snow and the snow cover on top of them corresponded to the individually measured amount of snow on top of each tank.

In order to save CPU time, only those particles were inserted into the Geant4 simulation whose trajectory did not miss a tank by more than 30 cm. Furthermore, once the total charge inside a tank surpassed a saturation threshold of 2000 VEM, particles in this tank were no longer simulated, but only counted. The total charge inside that tank was then scaled according to the ratio between total particle number and tracked particle number. This significantly reduced the time needed to simulate tank signals in the vicinity of the shower core.

4.4.2. Simulation of DOMs and triggers

In the next step, the photoelectrons were injected into the simulation of the PMT. Its response was simulated by superimposing Gaussian single-photoelectron waveforms with an RMS of 2.2 ns. Their charge was drawn according to the measured single-photoelectron charge distribution (Abbasi et al., 2010).

The DOM electronics were simulated (Roucelle, 2007b) by first convoluting the output of the PMT with a response function due to the limited spectral response of the electronics, mostly caused by the coupling transformer. Individual responses

[4] `http://www.silbrico.com/ryolex.htm`, retrieved 13 May 2011

for the different signal paths to the discriminator, the ATWDs and the FADC were used[5]. Then, discriminators and local coincidence conditions between DOMs were simulated, and if conditions were fulfilled, the signals were digitized using the measured ADC calibration constants. Droop was applied to the digitized waveforms[6] according to Eq. (2.1).

For simplicity, only the IceTop SMT trigger described in Section 2.1.3, and the 'global throughput trigger' that defines the overall trigger window were simulated. All other IceCube triggers were not relevant for the analysis presented here. The prescale for showers with less than 16 DOMs was not applied to the simulated data.

4.4.3. Calibration of the simulated tanks

The complete detector simulation chain including the Geant4 simulation of the tank and the simulation of the PMT and the electronics was calibrated using vertical muons in the same way as the real tanks. Proton induced air showers with an $E^{-2.7}$ primary energy spectrum and energies between 3 GeV and 30 TeV, and zenith angles up to 65° were simulated. These showers do not have enough energy to trigger the IceTop array, since only few particles actually reach ground, but can still produce a signal in individual tanks. A shower resampling method developed by Van Overloop (2010) was used in order to improve sampling efficiency.

The relation between 1 VEM and number of photoelectrons was taken from the calibration of the real tanks and used as an input to the simulation. Then, in the calibration procedure the ratio between the number of photoelectrons and the number of emitted Cherenkov photons was found:

- As an ansatz for this ratio, the number of Cherenkov photons emitted by a 4 GeV muon was estimated to correspond to 1 VEM. Using this relation, the emitted Cherenkov photons in the tank simulation can be converted to a number of photoelectrons before the PMT is simulated.

- Then, the tank response to low energy air showers was simulated to obtain muon spectra as in experimental data. The same functions as used in data, Equations (2.6) and (2.7), were used to determine the position of the VEM peak.

[5]For the discriminator and the ATWD paths the same response functions were used but measurements showed that they are different (David, 2009). Future versions of the simulation software will take this into account.

[6]Naturally, droop should be applied to analog waveforms, but both digitization and droop are linear operations and their order should not matter. The chosen order was based on performance considerations. In future versions of the simulation software, the natural order will be used, because otherwise digitization artifacts are introduced, that are not visible in experimental data.

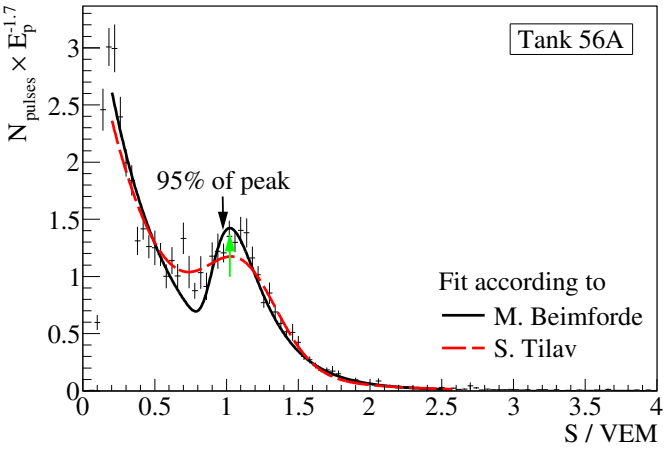

Figure 4.3.: Example of a simulated single tank charge spectrum used to calibrate the simulation after applying the calibration constant. The lines are fits of functions (2.6) and (2.7).

- From the ratio between the observed peak position and the expected peak position (taken from the calibration of the real tanks), a correction factor was obtained.

In this way, the ratio between the number of emitted Cherenkov photons and photoelectrons was found. An example of a simulated muon spectrum after calibration can be found in Fig. 4.3.

However, Cherenkov emission is the same for all simulated tanks. At the same time, 1 VEM is defined in the same way for all tanks. Therefore, 1 VEM corresponds to a number of Cherenkov photons that is independent of the tank. Thus, in air shower simulations, the number of emitted Cherenkov photons in a tank was then first converted to VEM. Then, this number was converted to a number of photoelectrons at each DOM, based on the DOM's individual VEM calibration. These photoelectrons were then fed into the PMT simulation.

4.5. Reweighting simulations to realistic fluxes

Air showers were simulated according to an E^{-1} spectrum in order to obtain a good coverage of the whole energy range. However, from previous experiments it is known that the flux in the energy range of interest has a spectral index changing from roughly 2.7 to 3.1. Therefore, the simulated events were reweighted based on their primary energy.

The generated flux is given by

$$\frac{\mathrm{d}^6 N^{\mathrm{gen}}}{\mathrm{d}E\,\mathrm{d}A\,\mathrm{d}\theta\,\mathrm{d}\phi\,\mathrm{d}t} \propto E^{-1}\cos\theta\sin\theta, \tag{4.3}$$

which corresponds to an isotropic E^{-1} flux,

$$\frac{\mathrm{d}^6 N^{\mathrm{gen}}}{\mathrm{d}\log E\,\mathrm{d}A\,\mathrm{d}\Omega\,\mathrm{d}t} = I\,\cos\theta, \tag{4.4}$$

where $\mathrm{d}\Omega = \sin\theta\,\mathrm{d}\theta\,\mathrm{d}\phi$. The factor $\cos\theta$ on the right is needed because the area perpendicular to the incident direction is $A_\perp = A\cos\theta$. In order to renormalize the generated events in all energy bins to a common flux, the normalization constant I_j must be determined for each energy bin j by integrating the simulated flux. The total number of events generated in bin j is

$$\begin{aligned} N_j^{\mathrm{gen}} &= I_j \int\limits_{\Delta\log E} \mathrm{d}\log E \iint\limits_{A_{\mathrm{gen}}} \mathrm{d}A \int\limits_{\cos\theta_{\mathrm{max}}}^{1} \mathrm{d}\cos\theta \int\limits_0^{2\pi} \mathrm{d}\phi \int\limits_0^{\tau} \mathrm{d}t\,\cos\theta \\ &= I_j\,\Delta\log E\,A_{\mathrm{gen}}\,2\pi\,\tau\,\frac{1}{2}\Big(1-\cos^2\theta_{\mathrm{max}}\Big) \\ &= I_j \Delta\log E\,A_{\mathrm{gen}}\frac{1}{2}(1+\cos\theta_{\mathrm{max}})\,\Omega_{\mathrm{gen}}\,\tau. \end{aligned} \tag{4.5}$$

And thus,

$$\frac{\mathrm{d}^6 N^{\mathrm{gen}}}{\mathrm{d}\log E\,\mathrm{d}A\,\mathrm{d}\Omega\,\mathrm{d}t} = \frac{N_j^{\mathrm{gen}}}{\Delta\log E\,A_{\mathrm{gen}}\frac{1}{2}(1+\cos\theta_{\mathrm{max}})\,\Omega_{\mathrm{gen}}\,\tau}\,\cos\theta, \tag{4.6}$$

with

- the number of events N_j^{gen} generated in bin j;
- the bin width, which is $\Delta\log E = 0.1$ for all energy bins;
- the solid angle in which events were generated, $\Omega_{\mathrm{gen}} = 2\pi\Big(1-\cos\theta_{\mathrm{max}}\Big)$;
- the sampling area $A_{\mathrm{gen}} = \pi\Big(1200\,\mathrm{m}\Big)^2$;
- the maximum simulated zenith angle, $\theta_{\mathrm{max}} = 56°$, and thus $\Omega_{\mathrm{gen}} \approx 0.88\pi$;
- and an arbitrary livetime τ, which acts as a scaling factor and has to be the same for all energy bins.

Good choices of the scaling factor τ are

- the experimental livetime, $\tau = T$, so that event numbers in the experiment can be compared to weighted event numbers in simulation;
- or $\tau = 1$, so that rates in simulation can be compared to experimental event rates.

The latter was chosen for all comparisons between data and simulation in this thesis (Section 4.6). In the determination of the detector response in Chapter 5 the overall normalization of the simulation will cancel out, and $\tau = 1$ was chosen there as well.

Thus, for an isotropic model flux, event weights thus only depend on primary energy. They were determined as the ratio between model flux and generated flux:

$$\begin{aligned} w(E) &= \frac{\frac{\mathrm{d}^6 N^{\mathrm{model}}}{\mathrm{d}\log E\,\mathrm{d}A_\perp\,\mathrm{d}\Omega\,\mathrm{d}t}(E)}{\frac{\mathrm{d}^6 N^{\mathrm{gen}}}{\mathrm{d}\log E\,\mathrm{d}A_\perp\,\mathrm{d}\Omega\,\mathrm{d}t}(E)} \\ &= \frac{\mathrm{d}^6 N^{\mathrm{model}}}{\mathrm{d}\log E\,\mathrm{d}A_\perp\,\mathrm{d}\Omega\,\mathrm{d}t}(E) \cdot \frac{\Delta\log E\, A_{\mathrm{gen}} \frac{1}{2}\left(1+\cos 56^\circ\right)\Omega_{\mathrm{gen}}}{N_i^{\mathrm{gen}}}. \end{aligned} \tag{4.7}$$

In the following, five different flux models used in this thesis will be presented.

4.5.1. Individual primaries

For comparisons of data and Monte Carlo (see Section 4.6), proton and iron primaries were individually reweighted to a flux (Ter-Antonyan and Haroyan, 2000):

$$\frac{\mathrm{d}N}{\mathrm{d}\log E} = I_0 \left(\frac{E}{1\,\mathrm{PeV}}\right)^{\gamma_1+1} \left(1+\left(\frac{E}{E_{\mathrm{knee}}}\right)^{\varepsilon}\right)^{(\gamma_2-\gamma_1)/\varepsilon}. \tag{4.8}$$

The parameters were obtained from a fit of experimental data averages (Hörandel, 2003) in the energy range from 100 TeV to100 PeV:

$$\begin{aligned} I_0 &= (5.62 \pm 0.21) \cdot 10^{-6}\,\mathrm{m}^{-2}\,\mathrm{s}^{-1}\,\mathrm{sr}^{-1}, \\ E_{\mathrm{knee}} &= (3.4 \pm 1.5)\,\mathrm{PeV}, \\ \gamma_1 &= 2.663 \pm 0.021, \\ \Delta\gamma &= \gamma_2 - \gamma_1 = -0.38 \pm 0.06. \end{aligned} \tag{4.9}$$

The parameter describing the sharpness of the knee was fixed to $\varepsilon = 2.1$, as given in the paper by Hörandel.

4.5.2. Two-component model

In addition to pure proton and iron, simulations of different primary particles were combined to three mixed composition assumptions. Proton and iron were combined according to a parametrization (Klepser, 2008) of Glasstetter's "two-component" model (Glasstetter et al., 1999), as an example of a simple mixed

composition. The proton flux was converted to the form (4.8) with

$$\begin{aligned} I_0 &= 3.89 \cdot 10^{-6}\,\mathrm{m}^{-2}\,\mathrm{s}^{-1}\,\mathrm{sr}^{-1}, \\ E_{\mathrm{knee}} &= 4.1\,\mathrm{PeV}, \\ \gamma_1 &= -2.67, \\ \Delta\gamma &= \gamma_2 - \gamma_1 = -0.72. \end{aligned} \tag{4.10}$$

For the sharpness of the knee $\varepsilon = 2.1$ was used as above since it could not be determined from Glasstetter's paper. The iron flux was taken directly from the paper by Glasstetter,

$$\frac{\mathrm{d}N^{\mathrm{Fe}}}{\mathrm{d}\log E} = 1.95 \cdot 10^{-6}\,\mathrm{m}^{-2}\,\mathrm{s}^{-1}\,\mathrm{sr}^{-1} \cdot \left(\frac{E}{1\,\mathrm{PeV}}\right)^{-1.69}. \tag{4.11}$$

The contributions from proton and iron to the total flux are shown in Fig. 4.4(a).

4.5.3. Poly-gonato model

In the poly-gonato model, the all-particle cosmic ray energy spectrum is modeled as the sum of individual spectra of all elements from hydrogen to uranium, each parametrized by Eq. (4.8). In the paper, both mass and rigidity-dependent knee positions are considered; as well as two options for the change in spectral index above the knee. For the simulations in this thesis, a rigidity-dependent knee, $E^Z_{\mathrm{knee}} = Z \cdot E^{\mathrm{Proton}}_{\mathrm{knee}}$, with $E^{\mathrm{Proton}}_{\mathrm{knee}} = 4.49\,\mathrm{PeV}$, combined with a common change in spectral index, $\Delta\gamma = 2.10$, for all elements was chosen since these options yielded the best fit according to Hörandel's paper. The smoothness parameter of the knee was set to $\varepsilon = 1.90$ as found in the paper. To simplify simulations, elements were divided into five groups and their combined spectra were fitted with function (4.8) except for pure proton for which the parameters were taken directly from the paper. Each group was then represented by a single element. This element was chosen by calculating the average nuclear charge in each group weighted with the flux at 1 PeV,

$$\langle Z \rangle_{\mathrm{weighted}} = \frac{\sum_i Z_i \cdot I_0^{(i)}}{\sum_i I_0^{(i)}}, \tag{4.12}$$

and then selecting the element with the closest Z. The results are given in table 4.2 and the contribution of the five elements to the total flux is illustrated in Fig. 4.4(b). Figure 4.5 compares the mean logarithmic mass $\langle \ln A \rangle$ (see Eq. (1.1)) of the two models which is the most relevant quantity when unfolding the energy spectrum. Clearly, the poly-gonato model yields a heavier composition than the two-component parametrization.

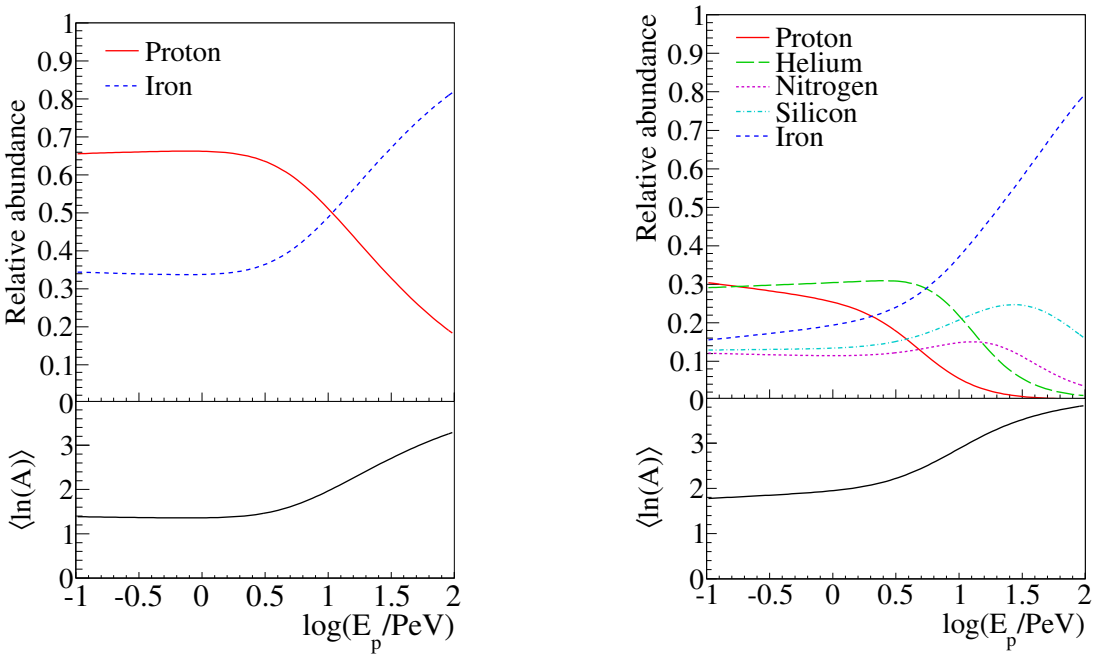

(a) Two-components (b) Poly-gonato

Figure 4.4.: Contributions of individual elements to the total flux in the two composition models used in this thesis. In the lower panels the mean logarithmic mass (see Eq. (1.1)) of the components used these parametrizations is shown.

Table 4.2.: Flux parameters of five elemental groups used in the simulation. The parameters were obtained from the model by (Hörandel, 2003) as described in the text. Each group was represented by a single element, in order to simplify simulations. I_0 is given in $10^{-6}\,\mathrm{m}^{-2}\,\mathrm{s}^{-1}\,\mathrm{sr}^{-1}$, and E_{knee} in PeV.

Group	I_0	$-\gamma_1$	$-\Delta\gamma$	E_{knee}	ε	$\langle Z\rangle_{\mathrm{weighted}}$	Representative
^{1}H	1.49	1.71	2.10	4.49	1.90	1.0	Proton
^{2}He – ^{4}Be	1.71	1.63	2.09	9.43	1.85	2.07	$^{2}_{4}$He
^{5}B – ^{9}F	0.633	1.68	2.10	32.29	1.85	7.13	$^{7}_{14}$N
^{10}Ne – ^{22}Ti	0.741	1.64	2.04	63.51	1.82	13.89	$^{14}_{28}$Si
^{23}V – ^{92}U	1.07	1.56	1.21	94.21	2.00	26.59	$^{26}_{56}$Fe

4.5.4. IceTop-IceCube coincident events

Finally, results from a measurement of IceTop-IceCube coincident events with the 40 string detector (Andeen, 2011b) were used. In this measurement, three primary particle groups were assumed: proton, iron, and an equal mixture of helium and oxygen. Their contributions to the total flux are listed in table 4.3. Since the energy range of these measurements was relatively limited, an extrapolation was used in order to build a response matrix that spans the whole energy range from 100 TeV to 100 PeV. Because composition in these results is almost constant in the lowest two energy bins, a constant composition was also assumed for $\log(E/\mathrm{GeV}) < 6.3$. For energies above the highest measured bin, $\ln(A)$ was assumed to increase linearly from bin to bin, with $\Delta \ln(A) = 0.244$ taken from the last two measured bins, until pure iron is reached at 100 PeV. The contribution of the He + O mixture was assumed to decrease linearly to 0 and the proton to iron ratio was chosen accordingly. This simple extrapolation and the limited range of measurements available will of course have an influence on the resulting energy spectrum, and results obtained with this composition will need to be treated with care. Furthermore, oxygen was substituted with the simulated nitrogen primaries in order to save CPU time and data storage.

4.5.5. Total flux in data analysis

In the unfolding analysis in Chapter 5, proton and iron fluxes were reweighted to a featureless E^{-3} flux with $I_0 = 5.47 \cdot 10^{-6}\,\mathrm{m^{-2}\,s^{-1}\,sr^{-1}}$ in order to reduce potential biases which could arise if a flux with features such as the knee is used as an input. Also, in the case of the two-component composition assumption, the Poly-gonato parametrization, and the IceCube 40 string results the total flux (i. e. the sum of the individual components' fluxes) was rescaled to the same E^{-3} flux.

4.6. Comparisons between simulated and experimental data

Monte Carlo simulations were used to derive the primary energy and efficiencies from the reconstructed quantities. Physical processes and the detector need to be modeled accurately in order for the relations obtained from Monte Carlo simulations to be meaningful and this agreement needs to be verified at various levels. For these comparisons, three primary mass assumptions and fluxes were used:

- Pure proton and pure iron individually, each weighted with the flux according to equations (4.8) and (4.9);
- A mixture of proton and iron according to the two-component model with the corresponding total flux.

Table 4.3.: Contribution of individual elemental groups to the all-particle flux resulting from the analysis described in Andeen (2011b). The numbers in the table are updated results to be published (Abbasi et al., 2011a; Andeen, 2011a). Extrapolation was necessary in order to build a large enough response matrix, for details see text.

Energy range $\log(E_p/\mathrm{GeV})$	$\langle \ln A \rangle$	Proton	Helium + Oxygen	Iron
4.9 – 6.3*	2.407	34%	13%	53%
6.3 – 6.5	2.407	34%	13%	53%
6.5 – 6.7	2.398	36%	9%	55%
6.7 – 6.9	2.508	35%	5%	60%
6.9 – 7.1	2.733	21%	22%	56%
7.1 – 7.3	3.106	15%	17%	69%
7.3 – 7.5	3.350	12%	10%	78%
7.5 – 7.7*	3.594	8%	6%	86%
7.7 – 7.9*	3.838	3%	3%	94%
7.9 – 8.1*	4.025	0%	0%	100%

* Extrapolation

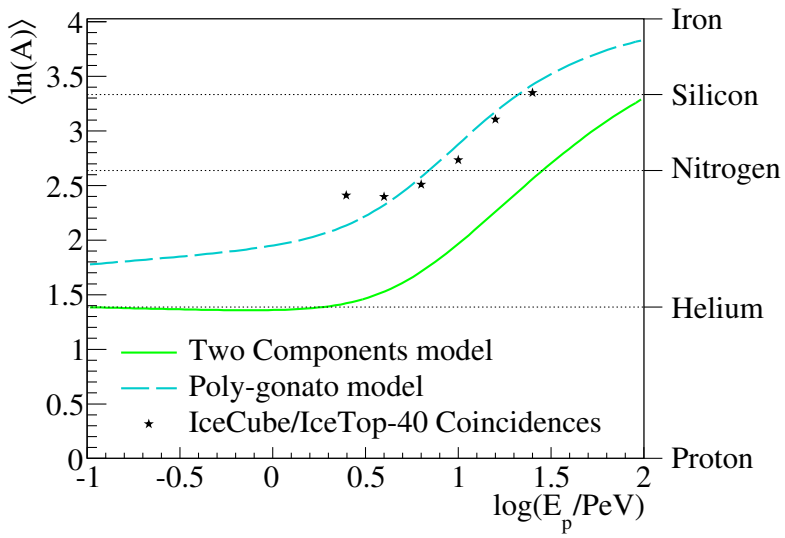

Figure 4.5.: Comparison of the mean logarithmic mass of the two-component and poly-gonato parametrizations used in this analysis. The black points are the measurements by K. Andeen (Andeen, 2011b; Abbasi et al., 2011a).

The simulated and measured showers were reconstructed and all cuts listed in Section 3.4 were applied, unless noted otherwise in some special cases. Furthermore,

$$\log(S_{125}/\mathrm{VEM}) \geq 1.0 \tag{4.13}$$

was required in order to avoid normalization problems due to a possible discrepancy in the threshold region which will be shown later in subsection 4.6.2. Since all of the observables shown here depend on the primary energy and mass spectrum, complete agreement between data and simulation cannot be required. However, all observed differences need to be scrutinized and explained.

An important point to note about these comparisons is that, due to the normalization of the simulation to a model flux (rather than to the observed number of events in data), a disagreement in the overall rate between data and simulation can arise. Most importantly, in all distributions iron showers show much lower rates than proton showers, despite the normalization to the same primary flux. This is caused by the fact that iron showers have smaller shower sizes and a larger energy threshold. This does not constitute a problem or disagreement. The only important question is whether the ratio between data and simulation is constant as a function of the observed quantity.

4.6.1. Measured quantities

At the lowest level, those quantities that can be measured directly and do not require reconstruction were compared to their simulated equivalents.

DOM occupancy. Participation of individual DOMs in air shower events depends on the location of the tank inside the array, the snow cover on top of the tank, and is different for high and low gain DOMs. Tanks at the corners of the array have a lower rate than those in the center. Snow attenuates electromagnetic particles reducing the rate of DOMs with a large snow cover. Finally, high gain DOMs have a higher rate than low gain DOMs due to the exponentially falling signal charge spectrum. Thus, the DOM occupancy shown in Fig. 4.6 is a good measure of how well these effects are reproduced by simulation. The ratio between data and simulation is plotted in the lower panel. The transition between high and low gain DOMs has some deficiencies (see next paragraph) leading to too large rates of high gain DOMs whereas low gain rates are underestimated. The overall rates, however, seem in good agreement between experiment and simulation, as will be shown in the next paragraph. Apart from that, rates in individual high gain DOMs (odd numbered) are well reproduced by simulation since the ratios are mostly flat, with some variation in the low gain DOMs (even numbers). The rates in case of iron are much lower than for proton (for both high-gain and low-gain DOMs), despite the identical primary energy spectra, due to stronger attenuation in the atmosphere of showers initiated by heavier primaries.

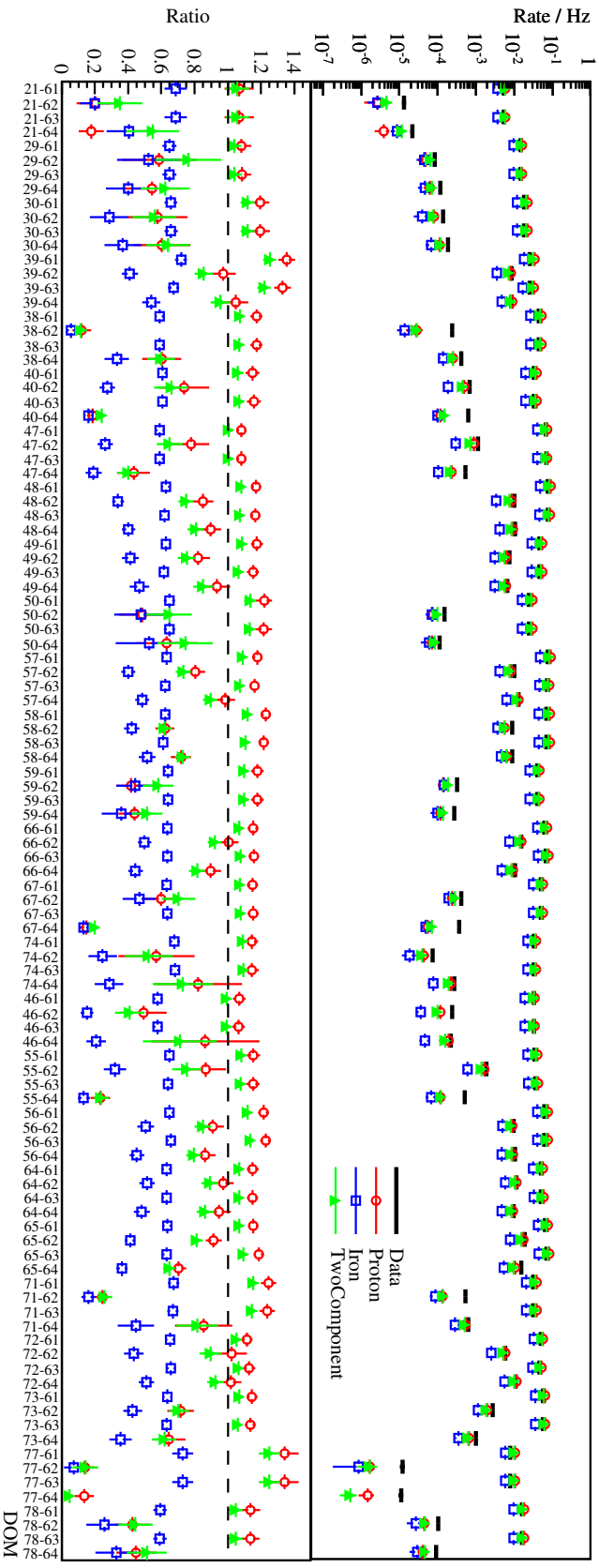

Figure 4.6.: Rates at which individual DOMs participate in air shower events in the final sample in data and simulation.

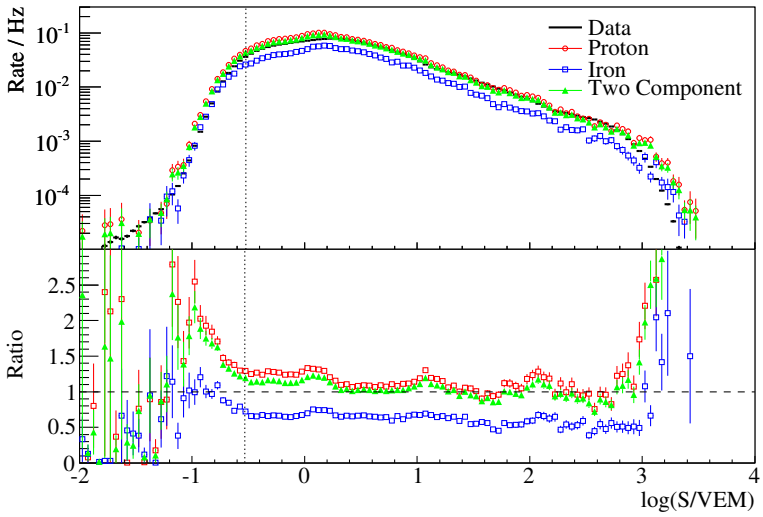

Figure 4.7.: Measured charge distribution in data and Monte Carlo simulation. The vertical dotted line at $S = 0.3$ VEM indicates the threshold of the charge-based retriggering (see Section 3.1.3).

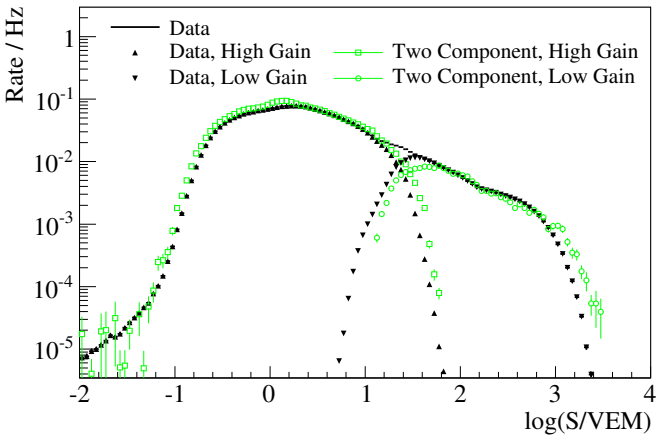

Figure 4.8.: Charge distribution in high and low gain DOMs in experimental data and the two-component simulation.

Signal charge spectrum. Since the energy reconstruction is based on the measured charges at each station, a realistic simulation is of particular importance. The signal size spectrum is determined by the spectrum of secondary particles and the IceTop tanks and electronics. Thus, a comparison between data and simulation, shown in Fig. 4.7, can give important information about the overall description of the detector. The best agreement in the overall rate, which is most visible in the ratio between data and simulation in the lower panel in the figure, is obtained for the mixed composition. In the case of pure proton, rates in the simulation are too large whereas they are too low in case of pure iron.

Starting at $S \sim 10^3$ VEM, a discrepancy in the saturation behavior between data and simulation is visible, independent of primary mass assumption. Since this analysis was limited to primary energies below 100 PeV, the impact of this discrepancy on the inferred primary energy is less than 2.5% (see Section 6.2.3).

The charge threshold below $\log(S/\mathrm{VEM}) = -0.5$ is too low in simulation which is one of the reasons for introducing the charge-based retriggering described in Section 3.1.3. There is some disagreement in the charge spectrum between $\log(S/\mathrm{VEM}) = -0.5$ and $\log(S/\mathrm{VEM}) = 0$ which improved slightly after retriggering at $S = 0.3$ VEM due to the re-evaluation of the local coincidence condition.

The feature in the ratio between simulation and data at $\log(S/\mathrm{VEM}) \approx 1$ is most likely related to an issue with the transition between high and low gain DOMs. As is apparent from Fig. 4.8, this transition happens at larger charges in simulated than in experimental data. At $\log(S/\mathrm{VEM}) \approx 2$ there is a feature in the ratio between data and simulation which can be related to the transition between two ATWD channels. There are known problems with the cross-calibration of these channels in the DOM firmware (Tilav, 2011). However, both of these features have only a minor influence on the overall charge spectrum.

Number of tanks per event. The number of tanks that participate in IceTop air shower events shown in Fig. 4.9 depends on the primary energy spectrum and mass composition, individual tank thresholds, and the local coincidence condition. Due to the local coincidence condition, odd tank numbers cannot occur. Accuracy of the detector simulation can be verified because measured rates mostly lie between the simulated proton and iron fluxes. Agreement between data and simulation is very good in case of the two-component assumption. In case of pure proton, there are too many events with a small number of tanks, while there are too few of these events in case of pure iron. This difference can be explained by the different shower attenuation in the atmosphere. The deficit in the uppermost bin for all composition assumptions is most likely due to the limited range of simulated primary energies.

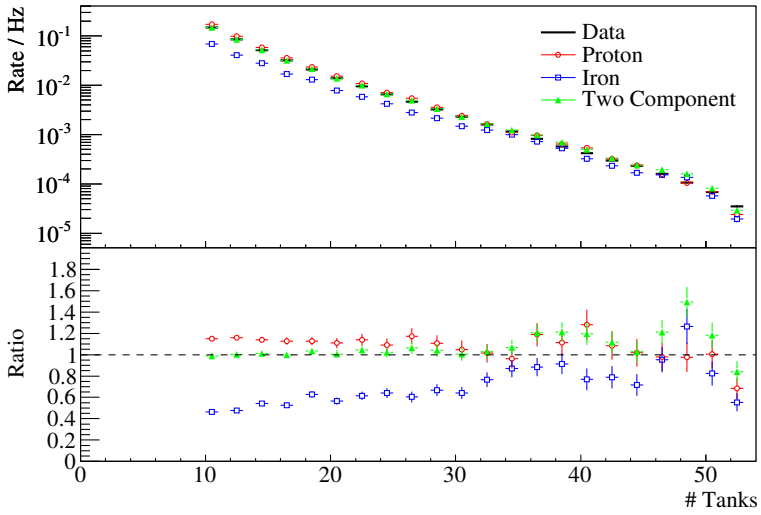

Figure 4.9.: Number of tanks participating in IceTop events. Due to the local coincidence condition odd tank numbers do not occur.

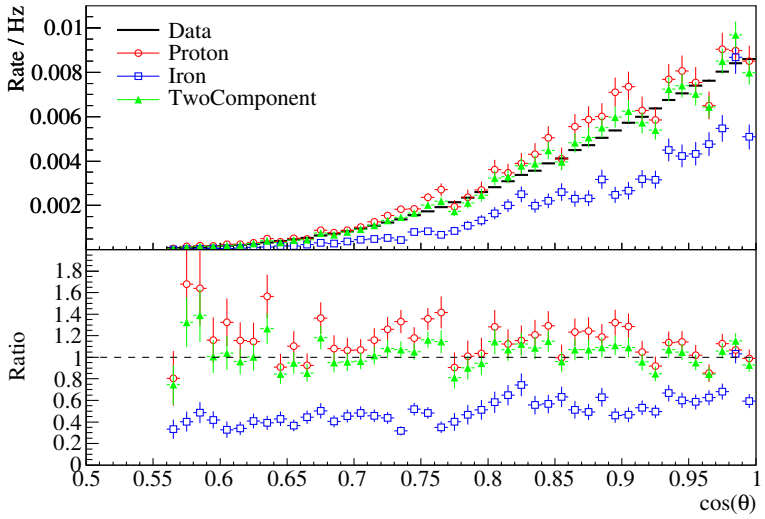

Figure 4.10.: Distribution of reconstructed zenith angles in data and simulation.

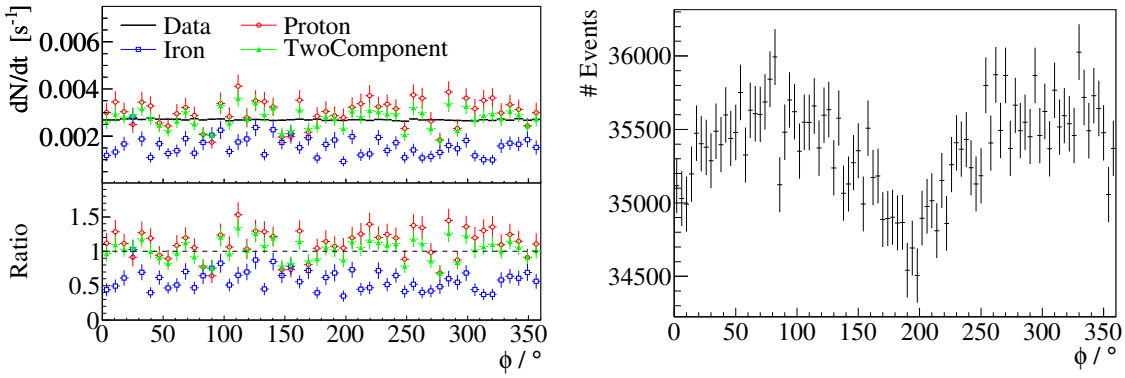

Figure 4.11.: *Left:* Distribution of reconstructed azimuth angles in data and simulation. Particles coming from positive x direction in the IceCube coordinate system have an azimuth angle of 0°. *Right:* Azimuth distribution in experimental data with a finer binning to reveal structures invisible in Monte Carlo due to limited statistics.

4.6.2. Reconstructed parameters

Reconstructed zenith angles. Showers are simulated isotropically and the cosmic ray flux is also assumed to be isotropic in the energy range of interest and at the sensitivity of this analysis. The zenith angle distribution of reconstructed events shown in Fig. 4.10 is influenced by shower attenuation in the atmosphere and the snow cover on top of the IceTop tanks. The distribution for experimental data lies in between the proton and the iron simulation, indicating that these influences are simulated realistically. Furthermore, best agreement between experimental and simulated data is achieved for the mixed composition. Agreement of the zenith angle distribution between data and simulation is particularly important since in this thesis the attenuation of showers with zenith angle will be exploited to study primary composition.

Azimuth. Since geomagnetic cutoff does not play a role in the given energy range azimuth angles of showers should be evenly distributed. Any deviation from uniformity is most likely a detector effect. In Fig. 4.11 a comparison of the reconstructed azimuth distribution in data and simulation is shown. Within statistical uncertainties, the azimuth distribution in simulation appears flat and in agreement with experimental data. However, due to the larger statistics experimental data show a variation of the order of 4%. It appears that showers moving along the x-axis of IceCube have a slightly smaller chance of triggering the array than those moving along the y-axis. This kind of asymmetry is not unexpected due to the shape of the 26 station IceTop array and it should disappear in the final configuration. A much larger Monte Carlo sample would be necessary to confirm this effect in simulation.

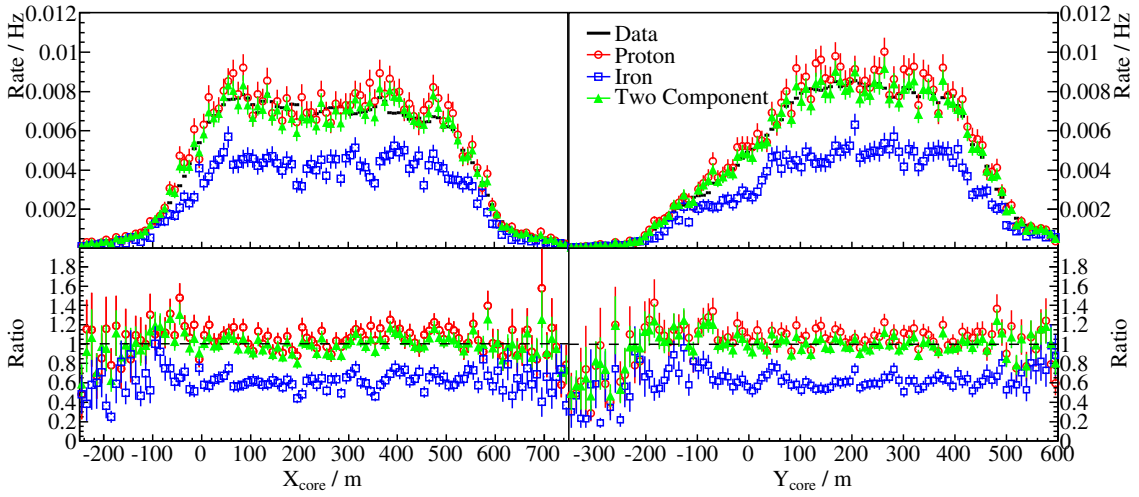

Figure 4.12.: Projection of the distribution of reconstructed core positions on the x-axis (left) and y-axis (right) of the IceCube coordinate system.

Core position. True and simulated shower core positions are distributed evenly across the IceTop array. The distribution of reconstructed core positions depends on the geometry of the array and on the distribution of snow.The energy threshold for showers with a core close to or outside the border of the array is higher than in the center of the IceTop and snow increases trigger thresholds. Figure 4.12 shows the projections of the distribution of reconstructed core positions on the x and y axes in the IceCube coordinate system. Inside the array, the projection on the x axis is almost flat whereas it drops steeply outside the array. The projection on the y axis is flat in the range $100\,\mathrm{m} < y_{\mathrm{core}} < 400\,\mathrm{m}$. The increase below $y = 100\,\mathrm{m}$ is a geometrical effect since the array becomes narrower in this range with a tip at station 21 at $y \approx 210\,\mathrm{m}$. Independent of primary composition assumption the ratio between data and simulation of the two projections is almost flat for the full range of contained air shower events.

Shower size. Simulated and measured spectra of the shower size parameter S_{125} in the zenith angle range from 0° to 46° are shown in Fig. 4.13. Above the threshold the agreement between data and the two-component model is very good. The proton flux is slightly larger whereas the iron flux shows a disagreement due to shower attenuation. Toward high energies proton and iron fluxes converge, which is to be expected from the decreasing difference in shower sizes that will be shown in Section 5.5. This observation is also in agreement with what is seen in the distribution of number of tanks shown in subsection 4.6.1.

The difference in threshold behavior between proton and iron Monte Carlo is most likely caused by the difference in shower attenuation and the bias introduced by the detector threshold, which allows only showers above a certain size to trigger the detector. Of course, signal fluctuations also influence the detector threshold

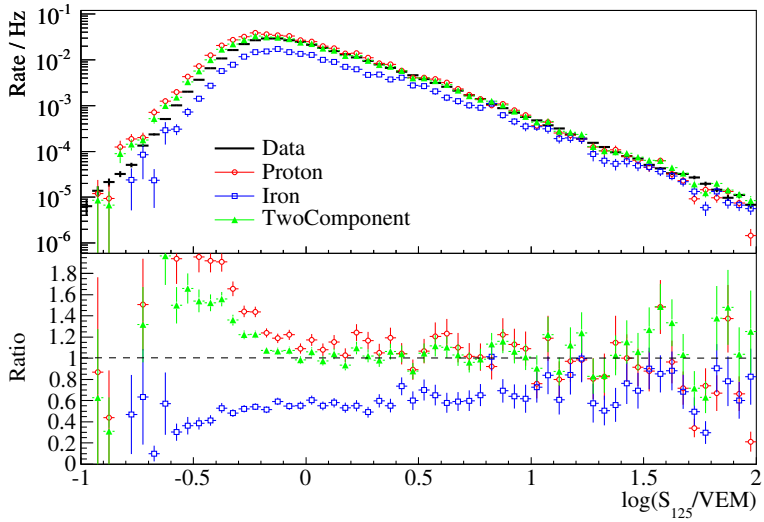

Figure 4.13.: Measured and simulated shower size spectra in the zenith angle range $0° \leq \theta < 46°$.

behavior and differences in these fluctuations between different primary particles can also have an effect on the shower size distribution in this region.

However, there is a possible discrepancy between data and simulation. The simulated S_{125} spectrum in case of the two-component model is in very good agreement with experimental data above the threshold, but it diverges below $\log(E_p/\mathrm{PeV}) < -0.2$. Of course, this might be explained by a difference in primary composition. However, an actual disagreement in shower size threshold cannot be excluded.

Slope parameter β. The parameter β of the lateral distribution function (3.7) is related to the shower age and is sensitive to primary particle mass, as will be shown in Section 5.5.3. However, there is a clear disagreement between data and simulation in the distribution of β as shown in Fig. 4.14. While the average value is well-reproduced by simulation, all composition models lead to a narrower distribution than in data. This might be related to possible differences in signal fluctuations between experiment and simulation (see next subsection). Since β was not used as a parameter for primary mass in this analysis this difference was not investigated any further. Additionally the cut on this parameter, $2 \leq \beta < 4.5$, only had a minor influence on the result. The peaks at $\beta = 1.5$ and $\beta = 5$ are pile-up effects due to the limitation of β to this range in the fit.

4.6.3. Likelihood values

χ^2 distribution of the lateral fit. The value of the likelihood function at its extremum is difficult to interpret as a measure of the quality of the lateral fit. A

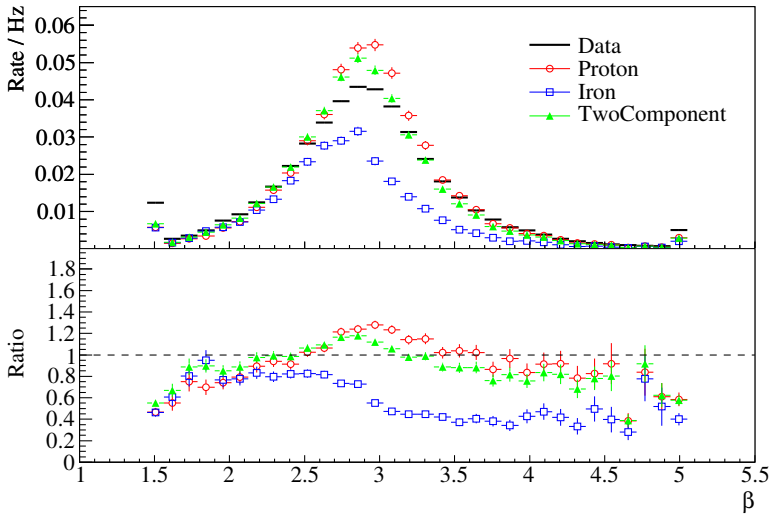

Figure 4.14.: Distribution of the lateral fit slope parameter β in data and simulation. The peaks at $\beta = 1.5$ and $\beta = 5$ are due to the limitation of the parameter in the lateral fit (see Section 3.2.3). The cut on β was not applied.

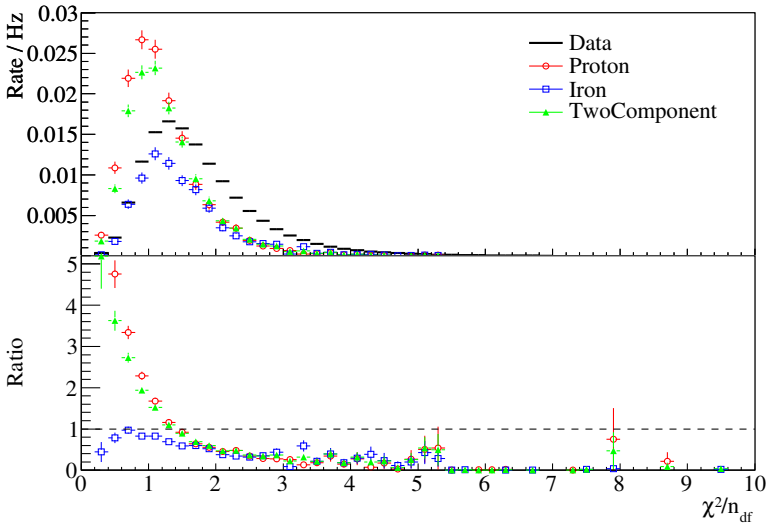

Figure 4.15.: Distribution of χ^2 per degree of freedom in the lateral fit. The χ^2 is defined in Eq. 4.14.

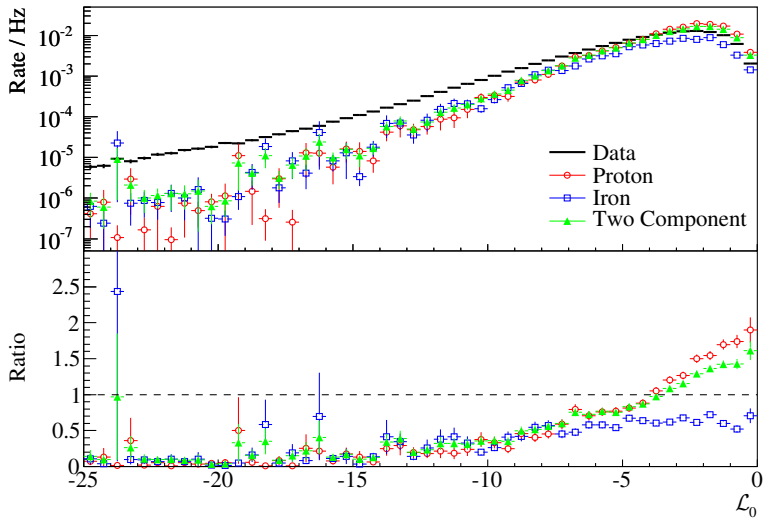

Figure 4.16.: Distribution of the no-hit log-likelihood $\mathcal{L}_0$ defined in Eq. (3.18) in data and simulation.

classical χ^2 function:

$$\chi^2 = \sum_i \frac{\left(\log S_i - \log S_i^{\text{fit}}\right)^2}{\sigma_S^2(S_i^{\text{fit}})}, \tag{4.14}$$

was used instead, where the sum runs over all triggered tanks. On average, this quantity should be close $\langle \chi^2 \rangle = n_{\text{df}}$, where n_{df} is the number of degrees of freedom, if signal fluctuations are described correctly by $\sigma_S(S)$ (see Eq. (3.22)). However, deviations from this value could to some degree be explained by the fact that the log-likelihood function (3.16) contains additional terms and the fact that fluctuations of $\log(S)$ are not purely Gaussian.

The χ^2/n_{df} distribution in data and Monte Carlo is shown in Fig. 4.15. In proton Monte Carlo the peak is $\chi^2/n_{\text{df}} \approx 1$ and only at slightly larger values in the case of iron simulation. In data on the other hand, the peak is at $\chi^2/n_{\text{df}} \approx 1.3$, indicating that signal fluctuations in data are larger than in simulation. This observation is also in agreement with the results of the signal fluctuation study in data and simulation that were shown in Fig. 3.4, although the interpretation of the difference was different at that time.

In fact, this discrepancy in the χ^2 distribution has already been observed with an older tank simulation code that was not based on Geant4 directly (Berghaus, 2009a). The use of Geant4 has improved the situation and a possibility for further improvement has been investigated (Melzig, 2011). This discrepancy is the reason why no cut on the reconstruction quality was made.

Likelihood term for tanks that have no signal. The no-hit log-likelihood, $\mathcal{L}_0$, defined in Eq. (3.18) is strongly influenced by the signal thresholds and signal

Table 4.4.: Passing rates of the quality cuts described in Section 3.4 for events with $S_{125} > 1$ VEM in data and the two-component simulation. Statistical errors on experimental data are negligible. All passing rates are given relative to the number of events with $N_{\text{station}} > 5$ and $S_{125} > 1$. In Fig. 4.17 this information is displayed graphically.

Cut	Experimental data		Simulation	
	Passing rate	Cumulative	Passing rate	Cumulative
$N_{\text{station}} > 5$	100%		100%	
Loudest station cut	42.5%	42.5%	$(39.4 \pm 0.5)\%$	$(39.4 \pm 0.5)\%$
CoG contained	60.4%	40.7%	$(56.4 \pm 0.4)\%$	$(37.6 \pm 0.5)\%$
Core contained	35.6%	32.1%	$(33.5 \pm 0.5)\%$	$(30.5 \pm 0.6)\%$
Zenith $\theta < 46°$	94.9%	30.9%	$(95.4 \pm 0.1)\%$	$(29.4 \pm 0.6)\%$
$\sigma_{\text{core}} < 20\,\text{m}$	92.8%	30.8%	$(93.4 \pm 0.2)\%$	$(29.4 \pm 0.6)\%$
$2.0 \leq \beta < 4.5$	92.1%	30.2%	$(96.4 \pm 0.1)\%$	$(29.3 \pm 0.6)\%$

fluctuations. Since pulses were retriggered with a charge threshold of 0.3 VEM, all DOMs have the same charge threshold in data and simulation, leaving signal fluctuations in the threshold regime as the main influence. As shown in Fig. 4.16, as in the case of the χ^2 distribution discussed above, there are clear differences between data and all simulations. In experimental data $\mathcal{L}_0$ takes larger absolute values than in simulation suggesting that fluctuations are underestimated. Certainly, there is a relation between the χ^2 and $\mathcal{L}_0$ and the discrepancy in the χ^2 distribution can at least partly be due to the $\mathcal{L}_0$ discrepancy.

4.7. Performance of the reconstruction

Table 4.4 lists the passing rates of data and two-component Monte Carlo of the individual quality cuts listed in Section 3.4. The same information is summarized graphically in Fig. 4.17. Due to the inconsistency between data and simulation in the threshold region (see Section 4.6.2), only events with $S_{125} > 1$ VEM were considered here. While there is some difference in the passing rates of individual cuts between experimental and simulated data, the overall passing rate is in good agreement. The remaining difference will be taken into account as a systematic error.

In Fig. 4.18, core position and angular resolution of the reconstruction for showers with zenith angles $\theta < 30°$ in case of the two-component model are shown as a function of energy. For 68% of reconstructed shower cores, the distance between true and reconstructed shower core position in the x-y plane is smaller than the value indicated in the figure. Similarly, the angular resolution is defined as the

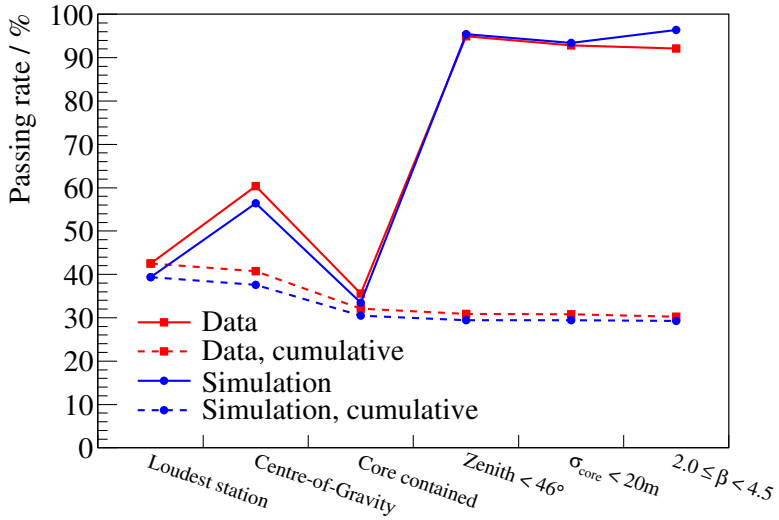

Figure 4.17.: Passing rates of the quality cuts described in Section 3.4 for events with $S_{125} > 1$ VEM.

angle between true and reconstructed shower direction,

$$\varphi = \arccos(\boldsymbol{n}_{\text{true}} \cdot \boldsymbol{n}_{\text{reco}}), \tag{4.15}$$

where $\boldsymbol{n}_{\text{true}}$ and $\boldsymbol{n}_{\text{reco}}$ are the true and reconstructed unit vectors in direction of movement of the shower front.

The core resolution of the likelihood fit improves from 15 m below 1 PeV primary energy to 6 m above 30 PeV. More inclined showers have a slightly worse core resolution, in the zenith angle range 40° to 46° between 8 and 19.5 m. This is consistent with a constant core resolution in the plane perpendicular to the shower axis. At the same time the center-of-gravity yields the best resolution at primary energies between 1 and 3 PeV, at about 22 m. Toward higher energies the resolution becomes worse, because showers are no longer fully contained inside the array, and therefore not sampled symmetrically. This strongly biases the center-of-gravity calculation. The core resolution as a function of energy above $E = 1$ PeV can approximately be described by

$$\sigma_{\text{core}}/\text{m} = \frac{10.4(7)}{\sqrt{E/\text{PeV}}} + 4.9(4), \tag{4.16}$$

which points at an optimum resolution at high energies of ~5 m.

The angular resolution of the likelihood fit improves from 0.9° below primary energies of 1 PeV to 0.3° at 100 PeV. More inclined showers have a slightly worse angular resolution, in the zenith angle range between 40° and 46° achieving 0.5° at 100 PeV. The resolution of the plane fit below 3 PeV is about 1.6° and degrades toward higher energies for the same reason as the center-of-gravity calculation:

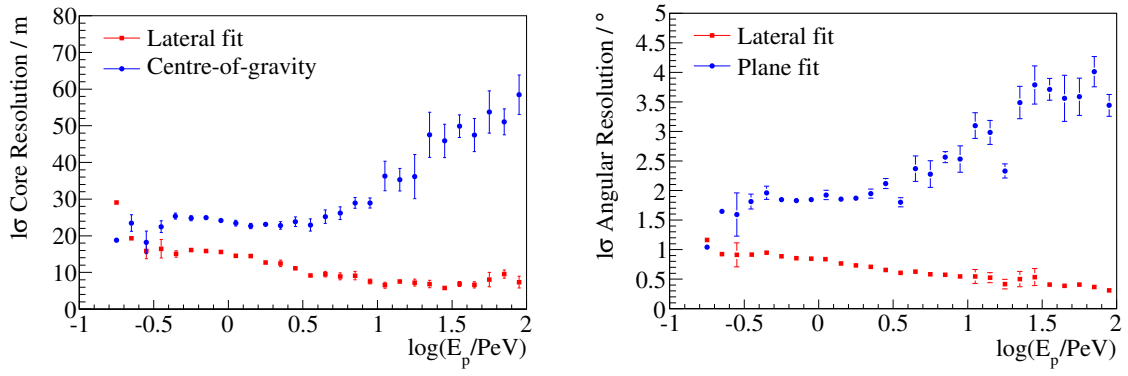

Figure 4.18.: Reconstruction quality of showers with $\theta < 30°$ in case of the two-component assumption. Given are the 1σ resolutions as a function of primary energy. *Left:* Distance between true and reconstructed shower core of the lateral fit and the center-of-gravity. *Right:* Angle between true and reconstructed shower direction in case of the likelihood and the plane fit.

the fit is biased if the shower front is sampled asymmetrically. A simple straight line fit above 1 PeV of the angular resolution as a function of energy yielded:

$$\sigma_{\text{angle}}/^\circ = 0.806(14) - 0.256(15)\log(E/\text{PeV}). \tag{4.17}$$

Obviously, this cannot be extrapolated to larger energies. However, a flattening is not yet clearly visible below 100 PeV.

5. Determination of the primary energy

An unfolding method was used to convert the shower size spectra described in Section 3.5 into primary energy spectra. The unfolding relies on the shower simulations described in the previous chapter and on assumptions on primary mass composition to account for detector response and efficiency.

5.1. General method

In order to convert the S_{125} spectra to energy spectra, the response of the detector to a primary particle of mass M, energy E_p, zenith angle θ, and azimuth ϕ was determined from the simulations described in the previous chapter. The response of the detector is defined here as the probability to measure the shower size S_{125} given the primary energy E_p,

$$P(S_{125}\,|\,E_p) = P(S_{125}\,|\,E_p; M, \theta, \phi), \tag{5.1}$$

which depends on the primary mass M and shower direction (θ, ϕ). For binned data the response can be described by a matrix $\mathbf{R}^{(k)}$, which connects the contents of bin i of a measured S_{125} spectrum, N_i^s $(i = 1, \ldots, m)$, with the contents N_j^p of bin j of a primary energy spectrum $(j = 1, \ldots, n)$ for the zenith range Ω_k:

$$N_i^s = R_{ij}^{(k)}\, N_j^p. \tag{5.2}$$

The response matrix elements can be formulated as an acceptance integral:

$$R_{ij}^{(k)} = \frac{\sum\limits_M \int\limits_{\Delta E_p^j} \mathrm{d}E_p \int\limits_0^1 \mathrm{d}\cos\theta \int\limits_0^{2\pi} \mathrm{d}\phi \int \mathrm{d}A \cos\theta\, \Phi(E_p;\, M)\, p(S_{125}^i, \Omega_k | E_p, x_c, y_c, \theta, \phi;\, M)}{\sum\limits_M \int\limits_{\Delta E_p^j} \mathrm{d}E_p \int\limits_{\Delta_k \cos\theta} \mathrm{d}\cos\theta \int\limits_0^{2\pi} \mathrm{d}\phi \int\limits_{A_{\mathrm{cut}}} \mathrm{d}A \cos\theta\, \Phi(E_p; M)}. \tag{5.3}$$

The model flux $\Phi(E_p; M)$ of nuclei with mass M, weighted by their acceptance function p, is integrated over primary energy bin E_p^j, angles θ and ϕ, and core po-

sition (x_c, y_c). The sum runs over all nuclei with masses M that contribute assuming a specific composition assumption. The acceptance function p describes the probability that a particle with mass M and kinematic parameters $(E_p, x_c, y_c, \theta, \phi)$ initiates an air shower with the S_{125} parameter in bin i and a reconstructed zenith angle in range Ω_k and that the event passes all cuts listed in Section 3.4. The detector response was averaged over azimuth angles in each zenith angle interval Ω_k defined in Eq. (3.29). It is normalized to the total number of events in energy bin j with true core position inside the fiducial area A_{cut} and zenith angle within Ω_k (indicated in the denominator by integrals over $\Delta_k \cos\theta$ and A_{cut}). Thus, the response matrix element $R_{ij}^{(k)}$ is equivalent to the ratio between the expected number of measured events in shower size and energy bin (i, j) and the true number of events in energy bin j. $R_{ij}^{(k)}$ therefore corresponds to the integral of the probability density $P(S_{125} \mid E_p)$, Eq. (5.1), over shower size bin i and energy bin j.

Due to this normalization $\mathbf{R}$ has the following normalization properties (dropping the superscript k for the zenith range):

$$\sum_i R_{ij} = \varepsilon_j, \quad \text{and} \quad \sum_j R_{ij} = 1. \tag{5.4}$$

The row sum of the matrix $\mathbf{R}$ is equal to the detection efficiency ε_j, i. e. the probability that a shower with primary energy E_p in bin j will be in the final sample in any S_{125} bin i. The second normalization property states that the probability for an event in S_{125} bin i to be caused by a primary particle of any energy is unity.

To obtain primary energy spectra from the measured data the matrix equation (5.2) has to be inverted:

$$N_j^p = (R^{-1})_{ji} N_i^s. \tag{5.5}$$

For this unfolding procedure the iterative algorithm described in Section 5.3 was used which properly accounts for statistical fluctuations.

5.2. Detector response

The integrals in Eq. (5.3) were solved numerically using the Monte Carlo method. Figure 5.1 shows the response matrix for proton showers with $0° \leq \theta < 30°$. The colors indicate the probability $P(S_{125}^i \mid E_p^j)$ to measure an S_{125} in bin i given a primary energy in bin j. The crosses represent $\langle \log(S_{125}/\text{VEM}) \rangle$ for each energy bin, and the RMS of the distribution. The binning uses a logarithmic scale. Above the threshold of about 1 PeV, $\langle \log(S_{125}/\text{VEM}) \rangle$ is almost proportional to $\log(E_p/\text{PeV})$. Below $E_p = 1\,\text{PeV}$ shower sizes approach a constant value because

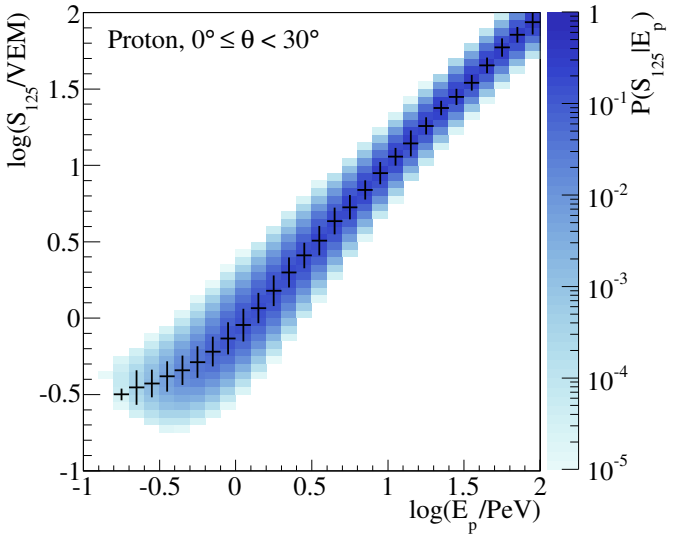

Figure 5.1.: Response matrix: distribution of the shower size S_{125} as a function of primary energy for simulated proton showers with zenith angles between 0° and 30°. The crosses indicate the mean value and RMS of the distribution in each energy bin.

smaller showers would not pass the 5 station requirement.

The distribution of $\log S_{125}$ in each $\log E_p$ bin was fit with a Gaussian to smooth statistical fluctuations:

$$p\Big(\log(S_{125}/\mathrm{VEM})\Big) = \frac{\varepsilon_j}{\sqrt{2\pi}\,\sigma_{\log S,j}} \exp\left(\frac{\Big(\log(S_{125}/\mathrm{VEM}) - \langle\log(S_{125}/\mathrm{VEM})\rangle_j\Big)^2}{2\,\sigma^2_{\log S,j}}\right). \quad (5.6)$$

The complete response matrix can then be described by the energy dependence of three quantities: mean value and standard deviation of these Gaussian distributions corresponding to mean logarithmic shower size $\langle\log(S_{125}/\mathrm{VEM})\rangle_j$ and resolution $\sigma_{\log S,j}$ in bin j. The efficiency ε_j was obtained from the simulation as

$$\varepsilon = \frac{\sum_{i=1}^{N_{\mathrm{rec}}} w_i}{\sum_{j=1}^{N_{\mathrm{gen}}} w_j}, \quad (5.7)$$

which is the ratio between the simulation weights of the events that pass all cuts (N_{rec} events) and the sum of the weights of all generated events (N_{gen} events). Due to migration of shower cores into the fiducial area, this quantity can become larger

Table 5.1.: Effective areas in the three zenith angle intervals Ω_k for proton showers. Within statistical uncertainties the same values were obtained for iron primaries.

Zenith range	$A_{\text{eff}}/10^5\,\text{m}^2$
$0° \le \theta < 30°$	1.051 ± 0.013
$30° \le \theta < 40°$	0.900 ± 0.019
$40° \le \theta < 46°$	0.803 ± 0.012

than unity. This needs to be taken into account when calculating the statistical error of ε_j, see Eq. (B.10). The complete error calculation for the efficiencies can be found in Appendix B.

The three quantities, $\langle \log(S_{125}/\text{VEM}) \rangle$, $\sigma_{\log S}$, and ε, are shown as a function of energy in Fig. 5.2. The average shower size increases almost linearly with energy and above threshold their relation can be approximated by

$$\frac{\mathrm{d}\log S_{125}}{\mathrm{d}\log E_p} \approx 1.05. \tag{5.8}$$

This will be used later in Chapter 6 in the estimation of systematic uncertainties.

Below the threshold between 1 and 3 PeV depending on zenith angle, shower sizes level off. This cutoff also influences the apparent energy resolution (see below). For a given primary energy, shower sizes of inclined showers are smaller than for vertical ones due to attenuation by the increased slant depth.

The standard deviation of the $\log S_{125}$ distribution peaks near the threshold, and narrows toward higher energies. The altitude of the shower maximum decreases (i. e. gets closer to the detector) with increasing primary energy. This leads to smaller shower fluctuations for larger energies, and a better energy resolution. The improvement toward lower energies is caused by the cutoff effect due to the trigger condition mentioned above. It is only an apparent improvement of energy resolution, since the cutoff also introduces a bias which impairs the actual energy resolution. The variation of $\log S_{125}$ is larger for inclined showers, because they traverse more atmosphere and are therefore detected further away from shower maximum.

The efficiency increases rapidly in the threshold region and then approaches a constant value at high energies. While the threshold energy increases with zenith angle due to shower attenuation in the atmosphere, the efficiency at high energies approaches ~92% almost independently of zenith angle. It is less than unity, mostly due to the strict containment cut (see Section 3.4). The peak efficiencies in the three zenith angle ranges Ω_k correspond to the effective areas A_{eff} given in Table 5.1. Within statistical uncertainties the same values were obtained for iron primaries.

For further smoothing, the energy dependence of these three quantities was

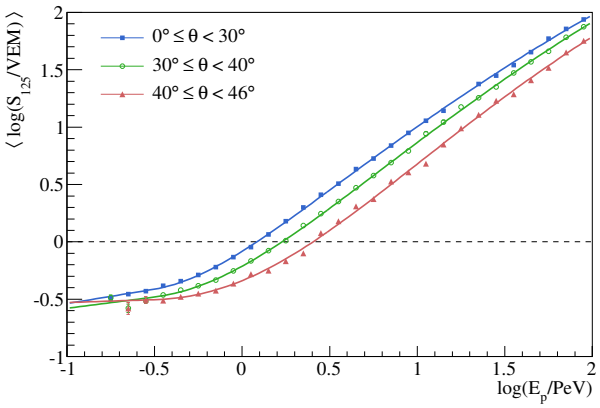

(a) Average shower size

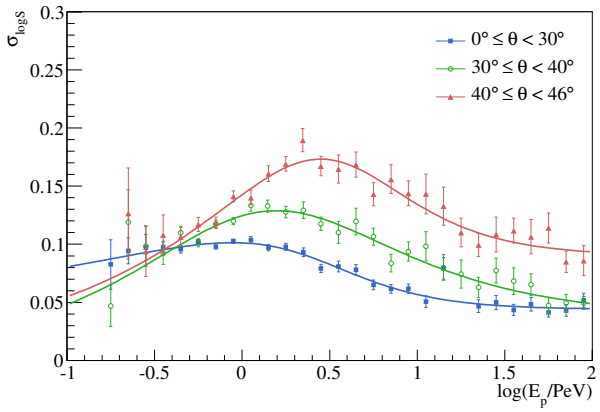

(b) Resolution

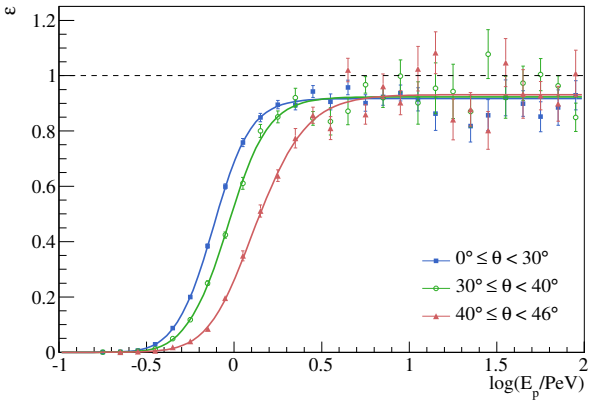

(c) Efficiency

Figure 5.2.: Parameters of the detector response for proton showers: (a) average shower size, $\langle \log(S_{125}/\mathrm{VEM}) \rangle$, (b) standard deviation of the shower size distribution, $\sigma_{\log S}$, and (c) efficiency ε, as functions of primary energy E_p.

fitted with empirical functions, adapted from Klepser (2008):

$$\langle \log S_{125} \rangle (E_p) = a_0 + \log E_p + \ln\left(\frac{\exp(a_1 \log E_p) + \exp\Big(a_2 + a_3 \log E_p + a_4 (\log E_p)^2\Big)}{1 + \exp(a_2)} \right), \quad (5.9)$$

$$\sigma_{\log S}(E_p) = \frac{b_0\Big(1 + \exp(b_3 b_4)\Big) + \exp(-b_1)\Big(\exp(-b_2 \log E_p) - 1\Big)}{1 + \exp\Big(-b_3(\log E_p - b_4)\Big)}, \quad (5.10)$$

and

$$\varepsilon(E_p) = \begin{cases} \dfrac{\varepsilon_0}{1 + \exp\Big(-c_1(\log E_p - c_2)\Big)} & \log E_p \geq c_4 \\ \dfrac{\varepsilon_0}{1 + \exp\Big(-c_1(\log E_p - c_2) + c_3(\log E_p - c_4)^2\Big)} & \log E_p < c_4 \end{cases}. \quad (5.11)$$

Besides smoothing the simulation results, these functions were also used to extrapolate in order to create a response matrix that spans the full range of measured shower sizes. This was done in order to avoid cut-off effects at the end of the unfolded spectrum. However, only data up to 100 PeV, which marked the upper end of simulated primary energies, were considered in the final result.

The first function, Eq. (5.9), parametrizes the mean shower size as a function of energy, taking into account that $\langle \log(S_{125}/\mathrm{VEM}) \rangle$ and $\log(E_p/\mathrm{VEM})$ are almost proportional above the threshold (see Fig. 5.2(a)). The residuals are parametrized as a smooth transition from a linear function describing the threshold behavior and a second order polynomial for the region above the threshold.

The resolution $\sigma_{\log S}$ was parametrized by a combination of two exponential functions and a constant in Eq. (5.10), see Fig. 5.2(b).

The efficiency, Eq. (5.11), is assumed to converge to a fixed value ε_0 at high energies, while the threshold is modeled by a second order polynomial in $\log \varepsilon$. The function is continuously differentiable at $\log E_p = c_4$.

While the standard deviation $\sigma_{\log S}$ of the S_{125} distribution in the energy bins is used in the unfolding procedure a more intuitive quantity is the energy resolution $\sigma_{\log E}$, i. e. the width of the distribution of reconstructed energies for a given primary energy. The distribution of reconstructed energies in primary energy bin j was obtained by transforming the S_{125} distribution in that bin back onto the $\log E_p$ axis using the average shower sizes parametrized by function (5.9). These distributions were then fitted with Gaussian functions, and the energy resolution was defined as their standard deviation. The energy resolution for proton showers from the three zenith ranges Ω_k is shown in Fig. 5.3. At 100 PeV a resolution of 0.04 in $\log E$ is achieved for showers with $\theta < 30°$, corresponding to a resolution

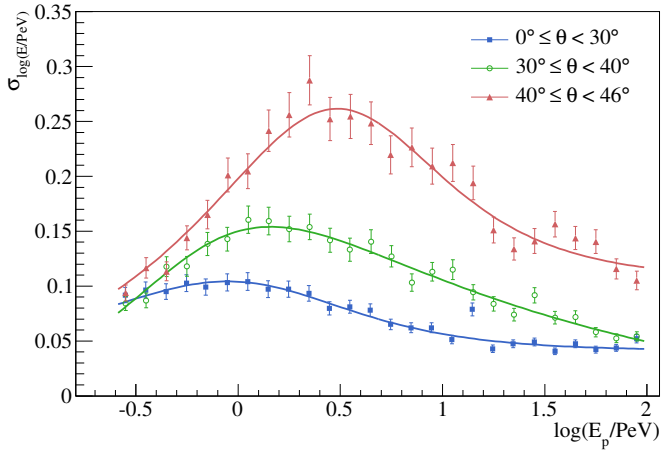

Figure 5.3.: Energy resolution for proton showers in the three zenith range Ω_k. Since the general behavior is the same as for $\sigma_{\log S}$, fit of the same functional form (Eq. (5.10)) are shown to guide the eye.

of 10% in energy. The resolution is worse for lower energy showers and for more inclined showers, due to the larger shower age.

In order to verify the fits of $\langle \log S_{125} \rangle (\log E_p)$, the function (5.9) was used to convert shower sizes from the same simulation dataset into energies, and the result was compared to the true energy (see Fig. 5.4). In order to ensure that function (5.9) could be inverted, it was extrapolated linearly below $\log(E_p/\mathrm{PeV}) = -0.5$ and above $\log(E_p/\mathrm{PeV}) = 2.5$. The inversion was calculated numerically. The extrapolation is responsible for the large energy mis-reconstruction in the threshold region. Since it is not needed in the unfolding process, where the full information from Equations (5.9) to (5.11) is used, no such mis-reconstruction should occur. As seen in Fig. 5.4, for the two-component primary composition and $\theta < 30°$, there is a small bias of less than 0.03 in $\log E$ in the range between 1 and 10 PeV due to slight shortcomings of the parametrization. However, this bias is much smaller than both the energy resolution (error bars in Fig. 5.4) and the chosen final bin size of the energy spectra (see next chapter). A very similar bias was found for more inclined showers and for other composition assumptions.

5.3. Unfolding

The response matrices described in Section 5.2 have to be inverted in order to reconstruct the primary energy spectrum from the measured S_{125} distribution. This was done using an iterative unfolding method based on Bayes' theorem which takes into account the efficiency ε and migration due to fluctuations $\sigma_{\log(S)}$ (D'Agostini, 1995).

The convolution of the energy spectrum with the detector response corresponds

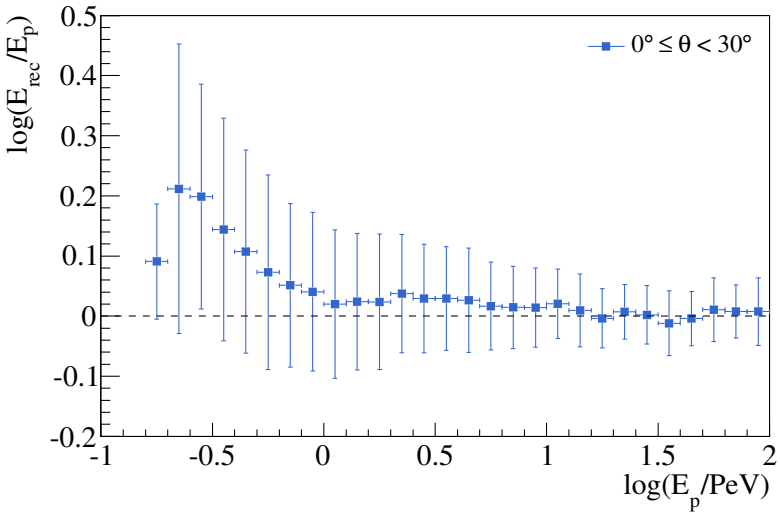

Figure 5.4.: Difference between reconstructed energies obtained using the parametrization (5.9) and true energies for the two-component assumption and $\theta < 30°$. The error bars indicate the spread of the distribution, and thus the energy resolution.

to a Fredholm integral equation of the first kind, where the kernel is given by the detector response. The limited resolution of the detector has a damping effect on high-frequency components of the input (the energy spectrum), so that the output (the shower size spectrum) appears "smoothed". Consequently, in the solution of the inverse problem all high-frequency components are amplified. Thus, simply inverting the response matrix $\mathbf{R}$ would lead to unnatural fluctuations in the result due to amplification of statistical fluctuations (Hansen, 1998). The unfolding algorithm avoids these fluctuations by assuming a smooth prior on the spectrum and by introducing a regularization criterion.

5.3.1. Unfolding algorithm

Starting from a prior distribution $P_k(E_p^{(j)})$ in the k-th iteration, the inverse of the response matrix, $\mathbf{R}^{-1}$, is constructed by inverting $R_{ij} = P(S_{125}^{(i)}|E_p^{(j)})$ using Bayes' theorem:

$$P_k(E_p^{(j)}|S_{125}^{(i)}) = \frac{P(S_{125}^{(i)}|E_p^{(j)})\, P_k(E_p^{(j)})}{\sum_\ell P(S_{125}^{(i)}|E_p^{(\ell)})\, P_k(E_p^{(\ell)})}. \tag{5.12}$$

Then, an estimate of the energy spectrum $\hat{N}_{j,k}^p$ is obtained from the shower size spectrum N_i^s:

$$\hat{N}_{j,k}^p = \frac{1}{\varepsilon_j} \sum_i N_i^s\, P_k(E_p^{(j)}|S_{125}^{(i)}). \tag{5.13}$$

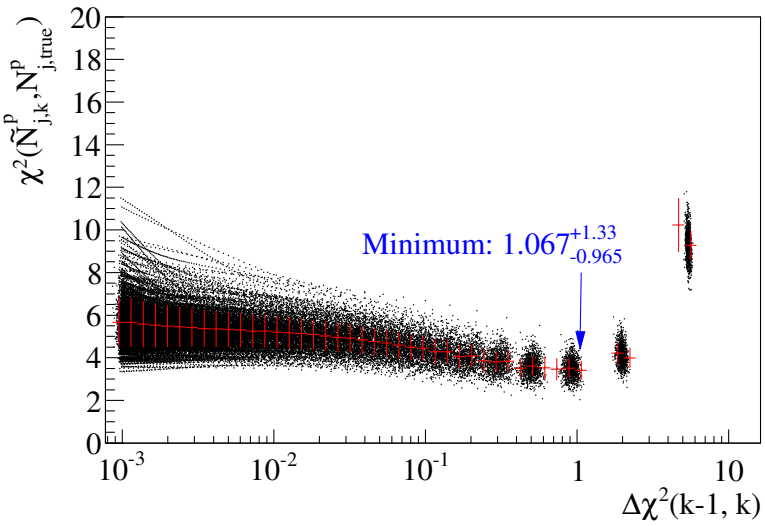

Figure 5.5.: Difference between true and reconstructed spectrum as a function of the regularization criterion $\Delta\chi^2$. In the toy simulation 1000 spectra were unfolded and after each unfolding step, $\Delta\chi^2$ and $\chi^2(\tilde{N}^p_{j,k}, N^p_{j,\mathrm{true}})$ were calculated (black dots). The red crosses are averages of $\chi^2(\tilde{N}^p_{j,k}, N^p_{j,\mathrm{true}})$ in bins of $\Delta\chi^2(k-1,k)$.

In the next step of the iteration, the prior distribution $P_k(E_p^{(j)})$ is replaced by

$$P_{k+1}(E_p^{(j)}) = \frac{\hat{N}^p_{j,k}}{\sum_\ell \hat{N}^p_{\ell,k}}. \tag{5.14}$$

These steps are repeated until the termination criterion described in the next subsection is reached. As initial prior a power law $P_0(E_p^{(j)}) \sim E_p^{-3}$ in the energy range $-1 \leq \log(E_p/\mathrm{PeV}) < 2$ was chosen normalized to the total number of events (weighted with their prescale factor) in the input S_{125} spectrum. The systematic error due to the choice of prior will be discussed in Section 6.5.2.

5.3.2. Termination criterion

The iteration was stopped once a termination condition was fulfilled. After each iteration, the unfolded spectrum was folded with the response matrix, $\tilde{N}^s_{i,k} = \sum_j R_{ij} N^p_{j,k}$. The convergence criterion was then defined using the change in χ^2 between $\tilde{N}^s$ and the measured shower size spectrum N^s between two iterations k and $k-1$, as used by Ulrich (2004):

$$\Delta\chi^2(k-1,k) = \chi^2(\tilde{N}^s_{k-1}, N^s) - \chi^2(\tilde{N}^s_k, N^s). \tag{5.15}$$

The iteration was stopped once $\Delta\chi^2$ dropped below $\Delta\chi^2_{\text{term}} = 1.1$. This is a regularization condition introduced to avoid unphysical fluctuations. After an infinite number of iterations the unfolding would converge to the result obtained by naïvely inverting the response matrix.

If the iteration is aborted too early, the result will still depend on the initial prior P_0 while too many iterations lead to unnatural fluctuations and strong negative correlations of neighboring bins. The optimum value of the termination criterion was determined using a toy simulation. In this toy simulation an assumed flux according to Eq. (4.8), $N^p_{j,\text{true}}$, was folded with the response matrix of proton showers in zenith range Ω_1 to obtain the expected event number $N^s_{j,\text{true}}$. Then, bin contents were varied 1000 times according to a Poisson distribution with mean $N^s_{j,\text{true}}$ and each spectrum N^s_j was unfolded. After each step $\Delta\chi^2(k-1,k)$ and the χ^2 between true and unfolded spectrum, $\chi^2(\tilde{N}^p_{j,k}, N^p_{j,\text{true}})$, were calculated, as shown in Fig. 5.5. The regularization parameter $\Delta\chi^2_{\text{term}} = 1.1$ was chosen in order to optimize the agreement between true and unfolded spectrum. The best value of $\Delta\chi^2_{\text{term}}$ varies for different assumptions on the primary composition and zenith angles but since the minimum is very wide it was decided for simplicity to use one value in all unfoldings.

5.3.3. Error estimation

Statistical errors were propagated through the unfolding process using the bootstrap method (Efron and Tibshirani, 1998) as follows. The measured shower size spectra were varied within their statistical errors and unfolding was repeated. This was done $n = 3000$ times for each spectrum and the errors of bin j were determined by comparing each unfolding result $N^{p(k)}_j$ to the average $\langle N^p\rangle_j$:

$$(\sigma^p_j)^2 = \frac{1}{n-1}\sum_{k=1}^{n}\left(N^{p(k)}_j - \langle N^p\rangle_j\right)^2. \tag{5.16}$$

Similarly, bin-to-bin correlations were obtained:

$$\text{cov}(i,j) = \frac{1}{n}\sum_{k=1}^{n}\left(N^{p(k)}_i - \langle N^p\rangle_i\right)\left(N^{p(k)}_j - \langle N^p\rangle_j\right). \tag{5.17}$$

The matrix of linear correlation coefficients, $\text{cov}(i,j)/\sigma_i\sigma_j$, for the two-component model with $\theta < 30^\circ$ is shown in Fig. 5.6. Adjacent bins are positively correlated, with a correlation coefficient decreasing with energy. This is expected due to the improvement of the energy resolution with increasing energy. Bins off the diagonal by two or three elements are slightly negatively correlated, but still acceptable, due to a slightly too large number of iterations. Bins at larger distances are mostly uncorrelated. In the threshold region bins are strongly correlated

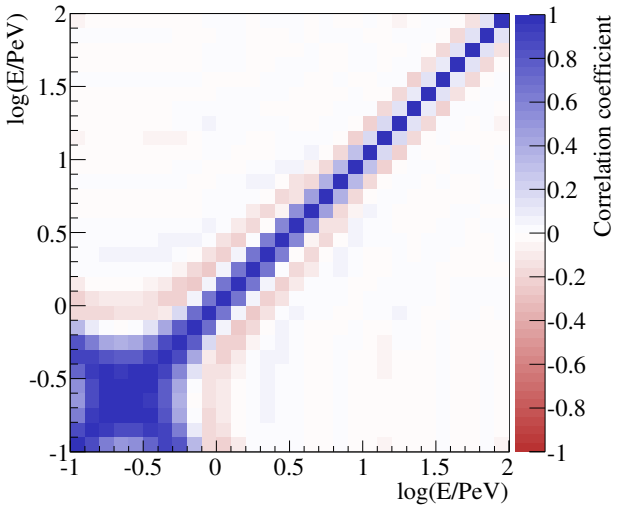

Figure 5.6.: Matrix of the linear correlation coefficients for the two-component model with $\theta < 30°$.

because energies can no longer be resolved due to the cutoff introduced by the trigger.

5.3.4. Verification of the unfolding procedure

The correctness of the unfolding procedure and the error assignment was verified using a simple toy simulation. A true energy spectrum according to the flux by Hörandel, equations (4.8) and (4.9), was assumed. Event numbers were drawn in bins with a width of 0.05 in $\log(E_p)$ assuming the experimental livetime and effective area and solid angle of IceTop in zenith band Ω_1. The spectrum created in this way was folded with the response matrix of the two-component assumption and then unfolded again. This was repeated 100 times.

Figure 5.7 confirms that the average unfolded flux corresponded to the input spectrum and that the average error assigned in each bin according to Eq. (5.16) corresponds to the spread of unfolded fluxes. The errors assigned using the bootstrap method described above correctly reproduce the spread of unfolded spectra. Above ~1 PeV where the detector is fully efficient the unfolding procedure correctly reproduces the model spectrum. The steep threshold function on the other hand is not taken into account very well leading to a divergence of the unfolded spectrum below threshold. The threshold region was therefore excluded in the final result.

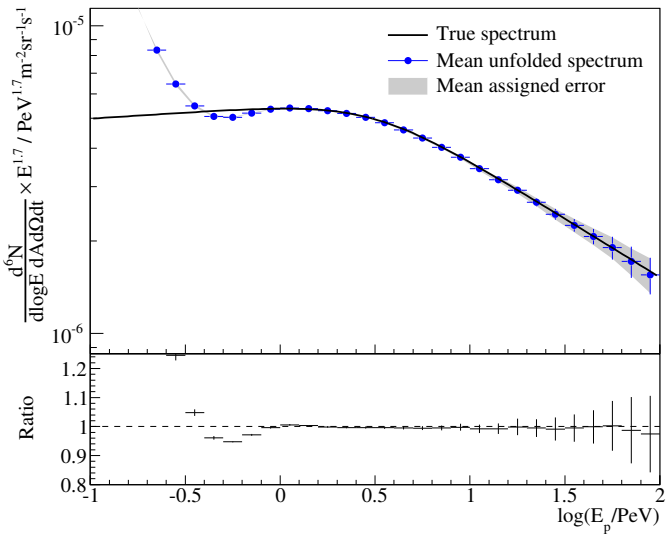

Figure 5.7.: Verification of the unfolding procedure using the toy simulation described in the text. In the upper panel the thick black line is the model flux and the blue points are the average unfolded energy spectrum. The shaded area represents the average errors assigned by the bootstrap method, while the error bars on the data points show the spread of unfolding results. In the lower panel the ratio between model flux and average unfolded spectrum is shown.

Table 5.2.: Energy thresholds in PeV and in $\log(E/\mathrm{PeV})$ where the efficiency becomes larger than 90% of the maximum value ε_0.

Primaries	Ω_1		Ω_2		Ω_3	
	$\log E$	E	$\log E$	E	$\log E$	E
Proton	0.115	1.30	0.218	1.65	0.450	2.82
Iron	0.263	1.83	0.530	3.39	0.572	3.73
Two Component	0.174	1.49	0.315	2.07	0.524	3.34
Poly-gonato	0.178	1.51	0.341	2.20	0.532	3.41
IceCube/IceTop-40	0.141	1.38	0.276	1.89	0.466	2.92

5.3.5. Energy thresholds

There is a potential discrepancy between data and simulation in the energy threshold of the detector discussed in Section 4.6.2. in the previous section, deficiencies of the unfolding procedure at the threshold were revealed. These lead to an untrustworthy spectrum in this energy range. Therefore, results are only considered in the region of full acceptance although the full S_{125} spectra were used as input for the unfolding. To define a threshold, the energy was chosen where the efficiency according to parametrization (5.11) becomes greater than 90% of the maximum value ε_0. The threshold increases with zenith angle and mass of the primary particle (Table 5.2). The discussion of systematic errors in the next chapter always refers to the energy range above these individual thresholds.

5.4. Correction for snow

As explained in Section 2.4, snow accumulates constantly on top of the IceTop tanks, but a manual measurement of the snow height is only possible during the austral summer and therefore is done only once every year. Techniques for an automatic, continuous monitoring of snow depths are under development (Rawlins, 2011; Kuwabara and Tilav, 2011), but were not yet available. The detector simulation took the snow depths measured in January, 2007, into account. Data, on the other hand, were taken between June and October, 2007, when more snow will have accumulated. In order to estimate the effect of this difference, the detector response to proton showers with primary energies of 1 PeV, 10 PeV and 30 PeV and zenith angles 0°, 30° and 40° was simulated assuming once the snow heights measured in January 2007 and once those measured in January 2008. In January 2007 the average snow depth on top of IceTop tanks was 20.5 cm, while in January 2008 the height on top of the same tanks was 53.2 cm. The results for vertical showers are shown in Fig. 5.8. Assuming constant growth of snow depth and proportionality between $\log S_{125}$ and snow depth, shower sizes in August, 2007, were estimated. All results are summarized in Table 5.3. Using Eq. (5.8) this lead to the following zenith angle dependent energy corrections relative to the simulations based on the January 2007 snow height measurement, which were applied to all unfolded energy spectra:

$$\begin{aligned} \Omega_1: &\quad \Delta\log(E/\mathrm{PeV}) = 0.0368(9), \\ \Omega_2: &\quad \Delta\log(E/\mathrm{PeV}) = 0.0440(13), \\ \Omega_3: &\quad \Delta\log(E/\mathrm{PeV}) = 0.0513(8). \end{aligned} \tag{5.18}$$

The values for different energies only seem to fluctuate but do not show a clear energy dependent trend.

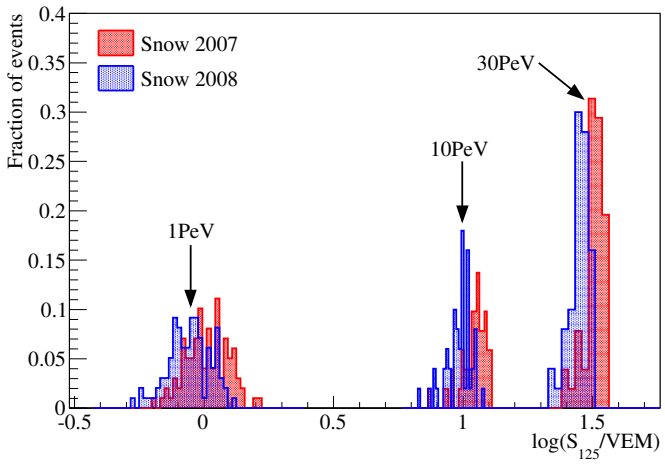

Figure 5.8.: Size of showers induced by vertical 1, 10, and 100 PeV protons assuming snow depths measured in January 2007 and 2008.

Table 5.3.: Size of proton showers of different primary energies and zenith angles given the snow covers of January 2007 and 2008 and an interpolation for August 15, 2007. The shift given in the last column is the difference to be applied to the data. N is the number of showers simulated for the given energy and zenith angle.

Energy	Zenith	N	January '07	January '08	August '07	Shift
1 PeV	0°	100	0.012(9)	−0.057(9)	−0.028(9)	−0.042(5)
	30°	100	−0.114(12)	−0.185(11)	−0.155(12)	−0.0435(19)
	40°	100	−0.266(13)	−0.318(10)	−0.296(11)	−0.032(6)
10 PeV	0°	50	1.043(7)	0.983(7)	1.008(7)	−0.0368(9)
	30°	50	0.965(7)	0.892(8)	0.922(8)	−0.0447(23)
	40°	50	0.807(12)	0.722(12)	0.757(12)	−0.0521(9)
30 PeV	0°	50	1.486(19)	1.430(19)	1.453(19)	−0.024(4)
	30°	50	1.447(9)	1.375(9)	1.405(9)	−0.0441(23)
	40°	50	1.337(9)	1.257(10)	1.290(10)	−0.0490(21)

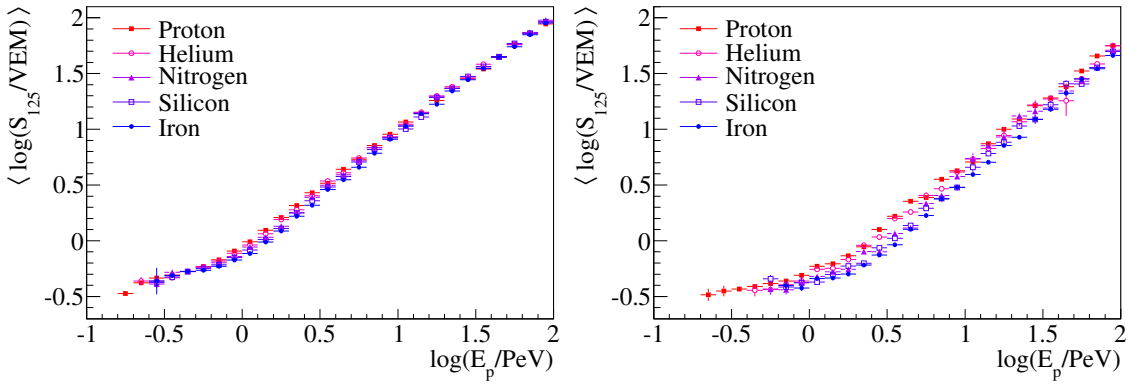

(a) $\theta < 30°$ (b) $40° \leq \theta < 46°$

Figure 5.9.: Mean logarithmic shower size in zenith intervals (a) Ω_1 and (b) Ω_3 as a function of energy for proton, helium, nitrogen, silicon and iron induced showers.

5.5. Showers initiated by primary particles of different mass

5.5.1. Shower size and energy resolution

The response matrices obtained with the procedure described in the previous section depend on an assumption on the primary energy and on the composition assumption — the shower development of different primary particles differs, as discussed in Section 1.4. In Fig. 5.9 the average logarithmic shower size of primaries of different mass as a function of energy is shown for zenith angle intervals Ω_1 and Ω_3. A qualitative explanation of the difference in shower development is given by the superposition model as described in Section 1.4.

Showers of heavy primaries, thus, lead to a smaller shower size than showers initiated by lighter particles of the same energy per nucleus. This attenuation increases for inclined showers, which is apparent when comparing Figures 5.9(a) and (b). The development of reconstructed shower size spectra for increasing zenith angle (Fig. 3.7), therefore, depends on primary mass composition, which can be exploited in order to draw conclusions about the primary cosmic-ray composition, as demonstrated by Klepser (2008).

Energy resolution is better for heavier primaries in the case of inclined showers, as shown in Fig. 5.11. Larger initial particle multiplicities reduce the variations of the shower development as discussed in the framework of the superposition model in Section 1.4. In the case of near vertical showers, the difference in particle numbers at ground level and the higher threshold could be the reason that the energy resolution for iron showers is worse than for proton showers, especially at low energies.

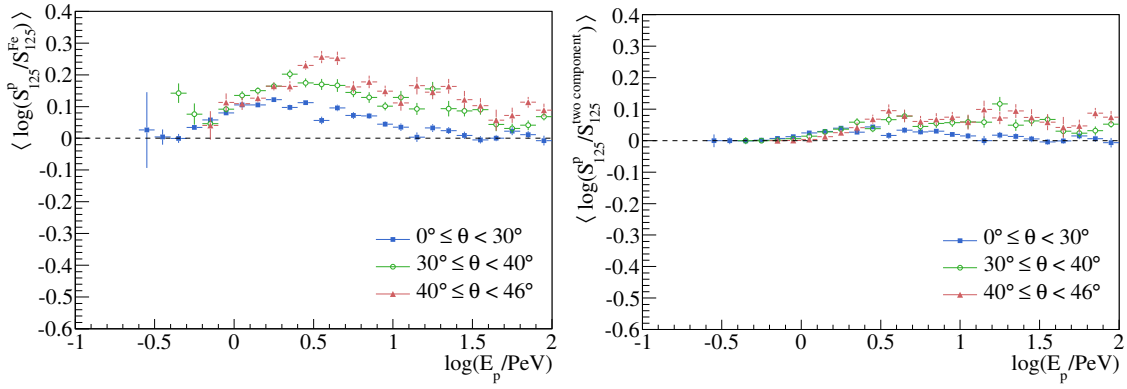

Figure 5.10.: *Left:* Difference in the shower size between proton and iron showers as a function of energy in all three zenith angle ranges Ω_k. *Right:* Comparison of proton showers and the two-component primary composition assumption.

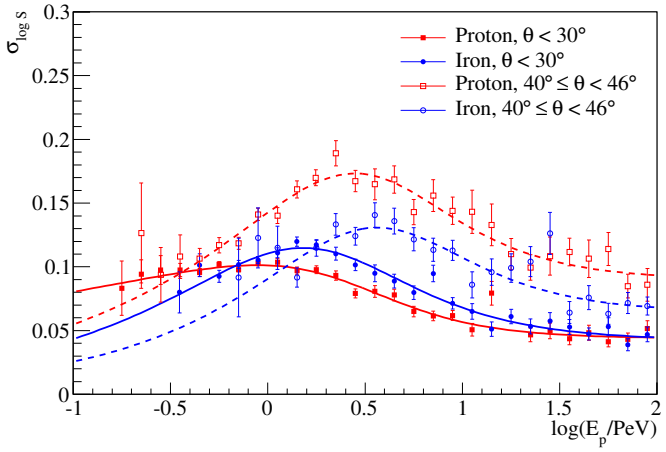

Figure 5.11.: Standard deviation of the S_{125} distribution of proton and iron showers in zenith angle ranges Ω_1 and Ω_3 as a function of primary energy.

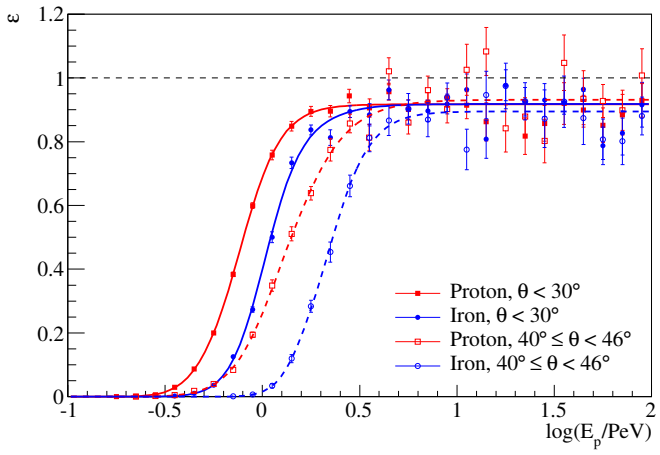

Figure 5.12.: Total efficiency for proton and iron showers in zenith angle ranges Ω_1 and Ω_3. While the maximum efficiency is independent of primary mass and zenith angle, the energy threshold strongly depends on these quantities.

The smaller size of showers initiated by heavy primaries also leads to an increased energy threshold, as shown in Fig. 5.12. Within statistical uncertainties, the maximum efficiency at high energies is independent of zenith angle and primary mass.

5.5.2. Effects on the unfolding result

The effect of different assumptions about primary particle composition on the result of the unfolding can be illustrated with the help of a highly simplified analytical calculation. The true energy spectrum is assumed there to be a simple isotropic power law:

$$\frac{\mathrm{d}N}{\mathrm{d}\log E} = E^{-2}. \tag{5.19}$$

Furthermore the detector resolution is assumed to be perfect, and without threshold:

$$\log S_{125}(\log E) = \log E + \log C, \tag{5.20}$$

where C is a constant that decreases with increasing zenith angle due to shower attenuation. The energy spectrum was then folded with this detector response, to obtain shower size spectra. In the folding the following values of C were assumed:

$$\log C_{\mathrm{true}}(\Omega_1) = 1.0, \qquad \log C_{\mathrm{true}}(\Omega_2) = 0.7, \quad \text{and} \quad \log C_{\mathrm{true}}(\Omega_3) = 0.4. \tag{5.21}$$

This can be compared to a lighter composition corresponding to a smaller decrease of $\log C$ with zenith angle and a heavier primary composition, where $\log C$ would

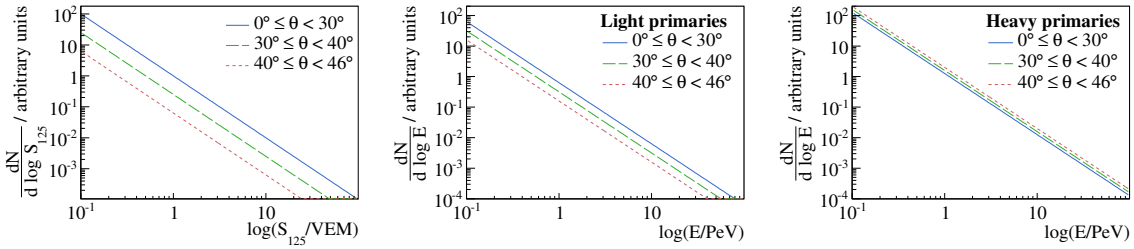

(a) Shower size spectra (b) Light composition (c) Heavy composition

Figure 5.13.: Toy calculation to illustrate the effect of the cosmic ray composition on the unfolding result. (a) Based on an isotropic flux, shower attenuation leads to different fluxes in different zenith angle ranges. (b) and (c) show that a wrong composition assumption in the unfolding can lead to an over or under compensation of shower attenuation.

decrease more strongly. This can be seen in Fig. 5.10 which compares average shower sizes of proton showers with iron and the two-component model.

The spectrum folded with the toy detector response (5.20) with the detector response is shown in Fig. 5.13(a). An unfolding then results in

$$\frac{\mathrm{d}N_{\mathrm{unfolded}}}{\mathrm{d}\log E} = \left(\frac{C_{\mathrm{true}}}{C}\right)^2 E^{-2}, \tag{5.22}$$

where C is the value assumed in the unfolding. If a composition is assumed that is too light the assumed shower size attenuation with increasing zenith angle will be too weak while it will be too strong if the assumed composition is too heavy. In the latter case the unfolding will overcompensate the shower attenuation while in case of a too light composition attenuation will not be fully compensated. This is illustrated in Figures 5.13(b) and (c). Only if the correct composition is assumed in the unfolding, $C = C_{\mathrm{true}}$, shower attenuation with zenith angle will be fully compensated, leading to agreement of the spectra from the three zenith angle ranges. This effect can in principle be exploited to determine primary composition. However, the sensitivity is not strong enough to make an independent composition measurement. Therefore, primary mass composition remains essentially unknown in this analysis and thus contributes to the systematic uncertainty.

5.5.3. Slope parameter β

Since the zenith angle dependency of S_{125} alone is not sufficient to measure the primary composition as a function of energy the unknown primary mass contributes to the systematic uncertainty on the all-particle spectrum. The slope parameter β of the lateral distribution function (3.6) was studied by Miloshevich (2009) in order to either allow a measurement of primary mass or allow for a mass

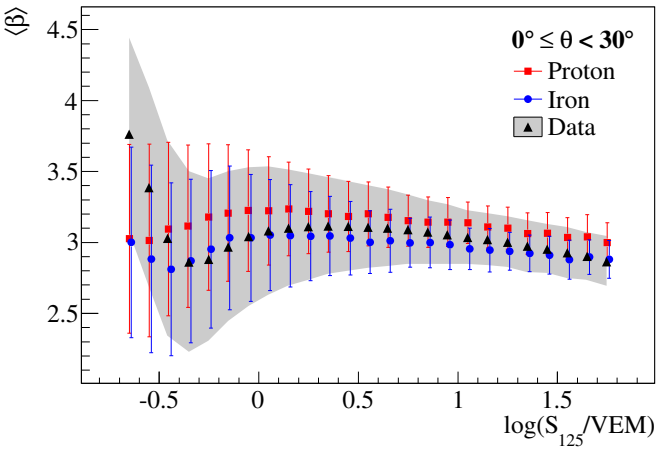

Figure 5.14.: Average slope parameter β of the lateral distribution function (3.6) as a function of shower size for proton and iron simulation and experimental data (Miloshevich, 2009). The error bars on the simulation data points represent the spread of β which is indicated by the gray band in case of data. The fact that data do not lie in between proton and iron simulation in the region below $S_{125} = 1\,\mathrm{VEM}$, is probably due a deficiency of the simulation in the threshold region.

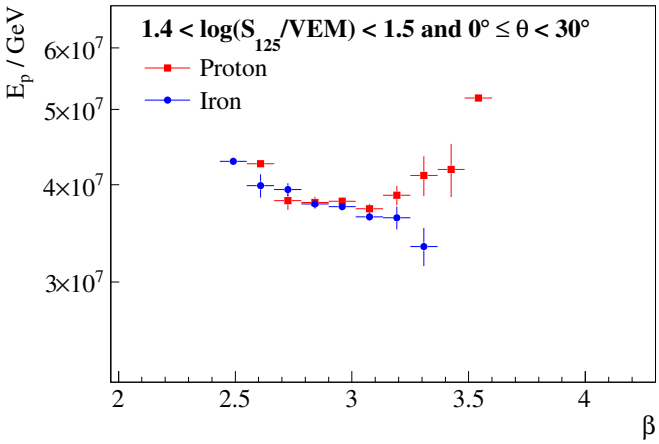

Figure 5.15.: Mean primary energy as a function of the slope parameter β for simulated proton and iron showers with $1.4 < \log(S_{125}/\mathrm{VEM}) < 1.5$ (Miloshevich, 2009).

independent measurement of primary energy.

Figure 5.14 shows the relation between β and shower size $\log S_{125}$ for proton and iron Monte Carlo and experimental data. Throughout the range of shower sizes, $\langle\beta\rangle$ for proton showers is larger than in case of iron. A larger β corresponding to a steeper lateral distribution function. As shown by Klepser (2008) a larger beta can be related to a smaller shower age. Thus, the result is expected due to the faster development of showers initiated by heavier primaries. In the 1 to 10 VEM range experimental data lie in between the proton and iron points with a tendency toward iron at higher energies. The fact that data do not lie in between proton and iron simulation in the threshold region is probably related to the discrepancy in thresholds between data and simulation.

On the other hand, it was shown that the mean primary energy of a shower with given S_{125} and β does not differ significantly between proton and iron showers, see e. g. Fig. 5.15. This means that β cannot be used directly to create a simple, primary particle independent energy estimator by correcting the energy obtained from S_{125} alone. Therefore, it was not used in this analysis. However, it could prove a valuable additional input parameter to composition analyses using multivariate techniques. However, before this parameter can be exploited, the discrepancy in the threshold region needs to be understood.

6. Systematic uncertainties

Several assumptions made during analysis, especially during Monte Carlo simulations, introduce systematic uncertainties to the result. These systematic effects are discussed in this chapter.

6.1. Environmental influence

6.1.1. Snow height measurement

To estimate the systematic error due to the energy correction for snow described in Section 5.4, snow accumulation was assumed proportional to wind speed (see Fig. 6.1), as illustrated in Fig. 6.2. In this case $\langle \log(S_{125}/\mathrm{VEM}) \rangle$ for a given E_p averaged over the period from June to October is smaller by

$$\Omega_1: \quad 0.0017, \qquad \Omega_2: \quad 0.0020, \quad \text{and} \quad \Omega_3: \quad 0.0021, \tag{6.1}$$

than the values estimated in Section 5.4 by assuming constant growth of snow depth. Using Eq. (5.8) this difference between snow heights using linear interpolation and an interpolation proportional to wind speed lead to a difference in reconstructed energy of:

$$\Omega_1: \quad 0.37\%, \qquad \Omega_2: \quad 0.44\%, \quad \text{and} \quad \Omega_3: \quad 0.46\%. \tag{6.2}$$

This was used as an estimate of the systematic error on energy determination due to snow height.

6.1.2. Variations of the atmosphere

The influence of atmospheric variations were studied using the experimental data. Two parameters of the atmosphere were studied: total overburden, X_v, and altitude profile, $\mathrm{d}\ln X_v/\mathrm{d}h$.

First, the days of data taking were ordered according to the total atmospheric overburden $X_v = p/g$, with the measured ground pressure p, and the gravitational acceleration at South Pole, $g = 9.86\,\mathrm{m/s^2}$. Then, the 50 days with the highest and with the lowest overburden were selected from the total of 153 days. The average overburden was $X_{\mathrm{low}} = 679\,\mathrm{g/cm^2}$ during the period of low overburden and $X_{\mathrm{high}} = 700\,\mathrm{g/cm^2}$ in the days of high overburden, yielding a difference

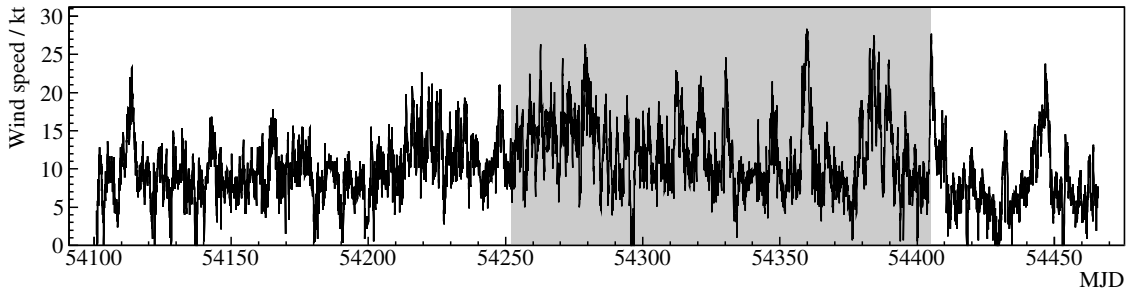

Figure 6.1.: Wind speeds measured at South Pole in 2007. Based on these measurements, the systematic error on snow depth in August 2007 was determined. The gray shaded region indicates the period during which the data used in this thesis were taken.

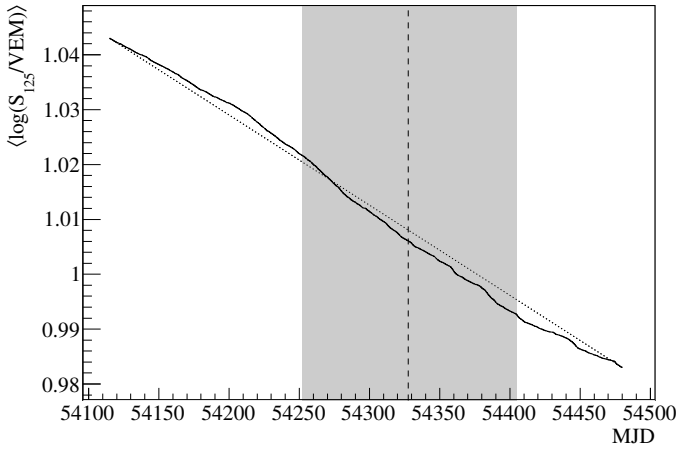

Figure 6.2.: Development of shower size of vertical 10 PeV proton showers in 2007, assuming $\log S_{125}$ is proportional to snow depth. Accumulation of snow is assumed proportional to wind speed (solid line) and constant (dashed line). The gray shaded area is the time between 1 June and 31 October, 2007.

of $\Delta X_v = 21\,\mathrm{g/cm^2}$. From the data taken during these periods shower size spectra were created, as shown in Fig. 6.3 for zenith range Ω_2.

For each zenith angle interval the weighted average logarithmic flux difference:

$$\langle \Delta \log I \rangle = \frac{\sum_{i=1}^{N_{\mathrm{bins}}} (\Delta \log I)_i / (\sigma_{\Delta \log I,i})^2}{\sum_{i=1}^{N_{\mathrm{bins}}} (\sigma_{\Delta \log I,i})^{-2}}, \tag{6.3}$$

was calculated in the range $0.6 \leq \log(S_{125}/\mathrm{VEM}) < 2.0$. Here,

$$(\Delta \log I)_i = \log\left(I^{(i)}_{\mathrm{high}} / I^{(i)}_{\mathrm{low}}\right) \tag{6.4}$$

is the logarithm of the ratio of fluxes in the ith bin and $\sigma_{\Delta \log I,i}$ is the statistical error of this quantity. Furthermore, both spectra were fit with a power law in the same range of shower sizes. It was found, that in all zenith ranges the two spectral indices, γ_{low} and γ_{high}, were compatible within statistical error. Thus, $\langle \Delta \log I \rangle$ can be converted into an approximately energy independent shift of $\log S_{125}$ using the average spectral index:

$$\Delta \log S_{125} = \frac{2}{\gamma_{\mathrm{low}} + \gamma_{\mathrm{high}}} \langle \Delta \log I \rangle. \tag{6.5}$$

Here, it is assumed that the flux of cosmic rays is constant in time (there is no indication of a variation of the flux in the energy range of interest and at the sensitivity of this measurement). This shift is only approximately energy independent. The assumption of energy independence of the effect of atmospheric overburden will certainly break down when energies at which the shower maximum for vertical showers is at or below detector altitude are covered in the analysis. Including the difference in atmospheric overburden, one can approximate

$$\frac{\mathrm{d} \log S_{125}}{\mathrm{d}X_v} \approx \frac{1}{\Delta X_v} \frac{2}{\gamma_{\mathrm{low}} + \gamma_{\mathrm{high}}} \langle \Delta \log I \rangle. \tag{6.6}$$

The results obtained for the three zenith angle intervals are:

$$\begin{aligned}
\Omega_1: &\quad \frac{\mathrm{d} \log S_{125}}{\mathrm{d}X} = (-1.2 \pm 0.9) \cdot 10^{-4} \, \frac{1}{\mathrm{g/cm^2}}, \\
\Omega_2: &\quad \frac{\mathrm{d} \log S_{125}}{\mathrm{d}X} = (-9.0 \pm 1.5) \cdot 10^{-4} \, \frac{1}{\mathrm{g/cm^2}}, \\
\Omega_3: &\quad \frac{\mathrm{d} \log S_{125}}{\mathrm{d}X} = (-14.3 \pm 2.9) \cdot 10^{-4} \, \frac{1}{\mathrm{g/cm^2}}.
\end{aligned} \tag{6.7}$$

The RMS variation of the total atmospheric overburden between June 1 and October 31, 2007, was determined to be $\sigma_{X_v} = 9.86\,\mathrm{g/cm^2}$. Using approximation (5.8),

this lead to a systematic error on energy of

$$\Delta \log E = \frac{\mathrm{d} \log S_{125}}{\mathrm{d}X} \cdot \frac{\sigma_X}{1.05}, \tag{6.8}$$

yielding the following relative uncertainties on E_p in the three zenith angle intervals:

$$\Omega_1: \quad 0.26\%, \qquad \Omega_2: \quad 1.94\%, \quad \text{and} \quad \Omega_3: \quad 3.09\%. \tag{6.9}$$

This variation was included as a systematic uncertainty.

In contrast to total overburden the altitude profile of the atmosphere at South Pole undergoes a clear annual cycle, see Fig. 2.9(b). To study the effect of varying the atmospheric profile on air shower measurements the data taking period was divided into a period of very dense atmosphere (July 25 to October 10) and one when the atmosphere was less dense (all other days). Shower size spectra were extracted from the data taken in these two periods and the same procedure outlined above was applied. The difference in shower sizes for a given primary energy between the two periods for the three zenith angle ranges is

$$\begin{aligned} \Omega_1: &\quad |\Delta \log S_{125}| = (11.3 \pm 1.5) \cdot 10^{-3}, \\ \Omega_2: &\quad |\Delta \log S_{125}| = (8.0 \pm 2.5) \cdot 10^{-3}, \\ \Omega_3: &\quad |\Delta \log S_{125}| = (5 \pm 5) \cdot 10^{-3}, \end{aligned} \tag{6.10}$$

yielding the following systematic errors on energy, when applying Eq. (5.8):

$$\Omega_1: \quad 2.5\%, \qquad \Omega_2: \quad 1.8\%, \quad \text{and} \quad \Omega_3: \quad 1.1\%. \tag{6.11}$$

Obviously, the systematic error in the most inclined zenith angle range is only a crude estimate since the difference between the two spectra is not very significant.

Assuming there is no correlation between altitude profile and total overburden (the linear correlation coefficient of the two quantities is only 0.340) the numbers obtained here and above have been added quadratically to estimate the systematic error due to atmospheric pressure variations listed in (6.9):

$$\Omega_1: \quad 2.6\%, \qquad \Omega_2: \quad 2.7\%, \quad \text{and} \quad \Omega_3: \quad 3.3\%. \tag{6.12}$$

6.1.3. Atmosphere model in simulation

To estimate the error due to atmospheric influences on the absolute energy scale simulations using two different atmosphere parametrizations were compared, see Fig. 6.4. Atmosphere model 12 (July 1, 1997), which was used in the unfolding procedure, has a total overburden of 692.9 g/cm^2 and atmosphere model 13 (October 1, 1997) has a total overburden of 704.4 g/cm^2. Averaging the difference in $\log S_{125}$ between the two simulations above $E_p = 1$ PeV the following changes

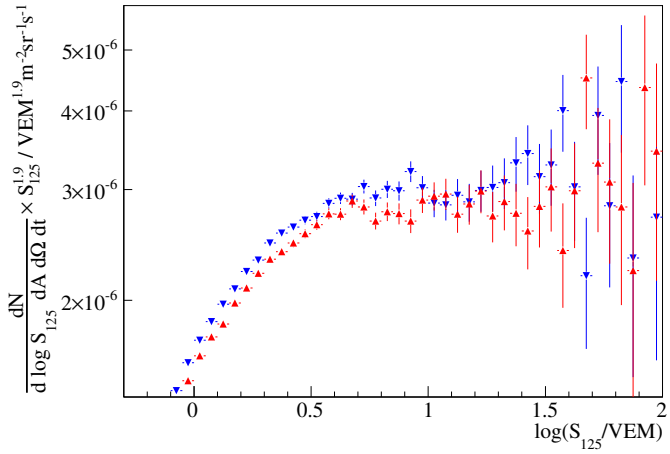

Figure 6.3.: Shower size spectra obtained in zenith range Ω_2 from data taken during the 50 days of highest (▲) and lowest (▼) overburden.

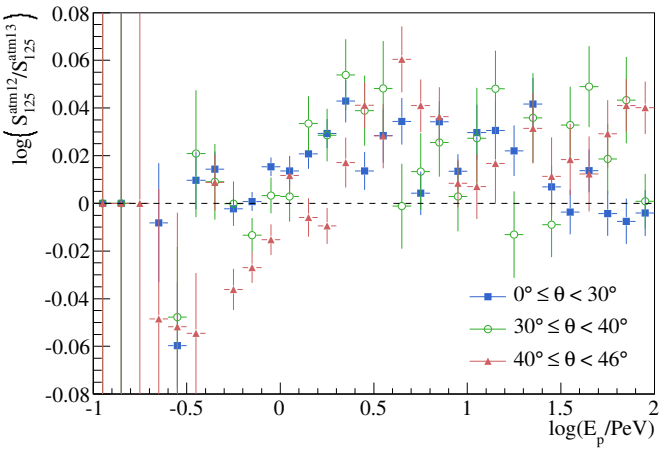

Figure 6.4.: Ratio between shower sizes as a function of energy obtained with CORSIKA atmosphere models 12 (July) and 13 (October).

of shower size with overburden were obtained:

$$\begin{aligned}
\Omega_1: \quad & \frac{\mathrm{d}\log S_{125}}{\mathrm{d}X} = (-14 \pm 2.2) \cdot 10^{-4} \, \frac{1}{\mathrm{g/cm^2}}, \\
\Omega_2: \quad & \frac{\mathrm{d}\log S_{125}}{\mathrm{d}X} = (-18 \pm 4) \cdot 10^{-4} \, \frac{1}{\mathrm{g/cm^2}}, \\
\Omega_3: \quad & \frac{\mathrm{d}\log S_{125}}{\mathrm{d}X} = (-9 \pm 6) \cdot 10^{-4} \, \frac{1}{\mathrm{g/cm^2}}.
\end{aligned} \tag{6.13}$$

This effect is larger than observed in experimental data, see (6.7). That might be due to different atmosphere profiles of the two models, as well as different atmosphere profiles contributing to experimental data. The difference between measured average overburden (695.5 $\mathrm{g/cm^2}$) and simulated overburden (692.9 $\mathrm{g/cm^2}$) thus lead to the following additional systematic uncertainties of the energy determination:

$$\Omega_1: \quad 0.9\%, \qquad \Omega_2: \quad 1.1\%, \quad \text{and} \quad \Omega_3: \quad 0.6\%. \tag{6.14}$$

6.2. Detector effects

6.2.1. Calibration

Systematic uncertainties due to calibration can arise for two reasons: variations of the calibration constants between calibration runs and a discrepancy between the calibration of the experiment and the detector simulation.

The first point was addressed by studying the variation of the VEM calibration between calibration runs. In Fig. 6.5 the relative difference in the number of photoelectrons corresponding to 1 VEM between calibration runs for all DOMs is shown. From the RMS of this distribution the systematic uncertainty on the energy reconstruction due to variations of the VEM calibration was estimated to be 3.0% using Eq. (5.8).

Simulated tanks were calibrated using the same procedure as for real tanks, as described in Section 4.4.3. For different tanks the conversion factors between number of Cherenkov photons and number of photoelectrons resulting from this calibration varied by 1.5% RMS. Since the Geant4 simulation of all tanks is identical, this is a purely statistical error. However, it was included as a systematic error on the energy of the same order because fixing the calibration constant leads to a systematic error on the calibration that is the same for all signals.

Varying the spectral index of the primary energy spectrum of the showers used in the calibration of simulated tanks did not yield any systematic change of the calibration constant.

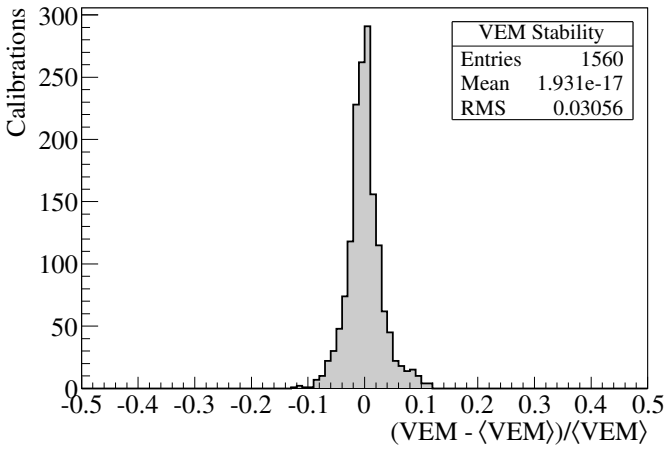

Figure 6.5.: Relative change in the number of photoelectrons corresponding to 1 VEM between consecutive calibration runs for all calibration runs and all DOMs. The RMS value of 0.031 of this distribution was used to estimate the systematic error of the energy determination.

6.2.2. Droop

The toroid used to decouple the PMT from the signal capture electronics introduces a significant droop effect, as described in Section 2.1.3. This droop was not corrected for, which in itself is not a source of systematic uncertainty, since it should be covered by the VEM calibration. However, discrepancies in the way the droop effect is simulated in the detector Monte Carlo or incorrect droop parameters (not all DOMs were measured individually) may lead to undesired systematic effects. In order to quantify these effects a set of experimental and Monte Carlo data were reprocessed correcting for droop. After droop correction, signal charges are smaller than without, due to the baseline determination described in Section 3.1.2, by about 2% for "droopy" and 0.5% for "non-droopy" DOMs, see Fig. 6.6. Comparing this effect of droop on the charge determination in Monte Carlo and experimental data leads to a systematic uncertainty on the energy determination of about 1.5%. This uncertainty was assumed to translate directly into a systematic error of the energy determination. The effect can be partly compensated by VEM calibration. However, since not all simulated DOMs were calibrated individually some uncertainty remains.

6.2.3. PMT Saturation

Differences between simulated saturation behavior of the PMT and the true behavior can cause a systematic uncertainty on energy determination mostly at high energies. As shown in Fig. 6.8, in simulation saturation sets in at higher charges than in the experiment. In order to estimate the effect of this discrepancy on the

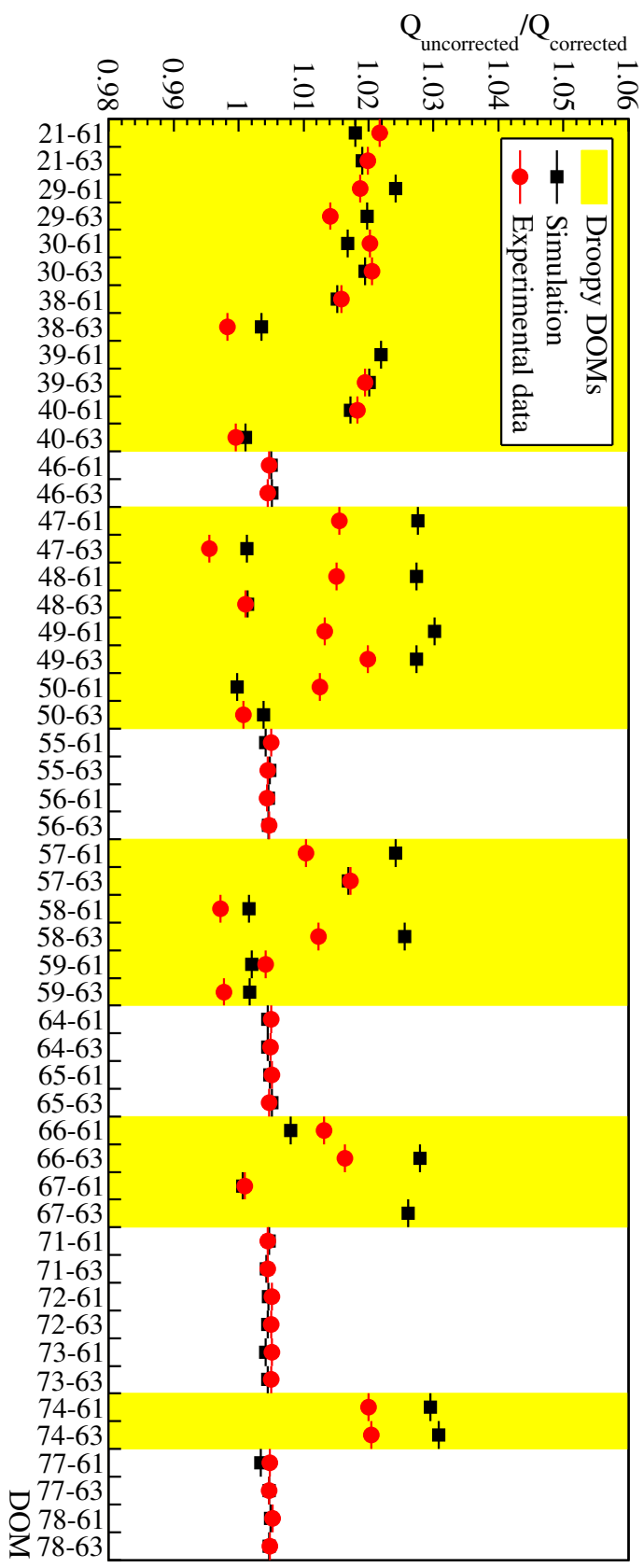

Figure 6.6.: Ratio between pulse charges with and without droop correction, when pulses are otherwise treated identically, for both simulated and experimental data.

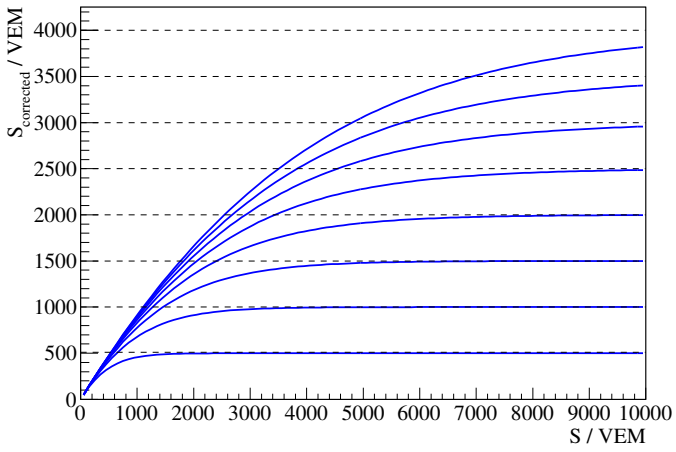

Figure 6.7.: Saturation function (6.15) for different values of the maximum charge $S_{\max}$ (dashed lines).

energy spectrum, an artificial, charge-based[1] saturation function was applied to the simulated charges S (see also Fig. 6.7),

$$S_{\text{corrected}}(S) = S_{\max}\left[1 - \frac{\ln\left(\exp\left(-\frac{S\,\ln(4)}{S_{\max}}\right)+1\right)}{\ln(2)}\right], \tag{6.15}$$

in order to bring the simulated charge spectrum in agreement with experimental data. The only parameter in the formula, $S_{\max}$, is the maximum possible charge. A saturation value of $S_{\max} = 3000\,\text{VEM}$ yielded the best agreement between simulated and experimental data. Simulated showers were reprocessed and the change in $\log S_{125}$ was used to estimate the systematic error on energy based on Eq. (5.8), see Fig. 6.9. For primary energies below 10 PeV, the systematic error due to the difference in saturation behavior is less than 0.5%. Above 10 PeV it increases exponentially to a value of 2.5% at 100 PeV.

Ideally, the influence of saturation on simulated shower sizes would be taken into account as a correction when determining the response matrices. However, since this is only an effect of less than 2.5% (much less than the total systematic uncertainty), it was decided to simply include it as a systematic error. This should also improve for future analyses since the gain dependence of saturation has been studied (Berghaus, 2009b) in order to improve the agreement between data and simulation at high charged.

[1] In reality, current is the relevant parameter for saturation. However, applying additional saturation to charges was simpler since a complete reprocessing of waveforms was avoided.

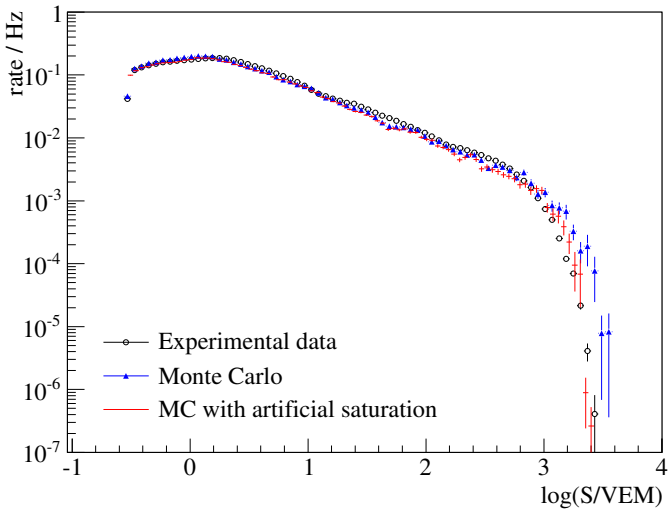

Figure 6.8.: Distribution of measured charges in all showers in the final data sample (black open circles), compared to proton Monte Carlo simulations (blue triangles), and simulations including an artificial charge saturation (red crosses).

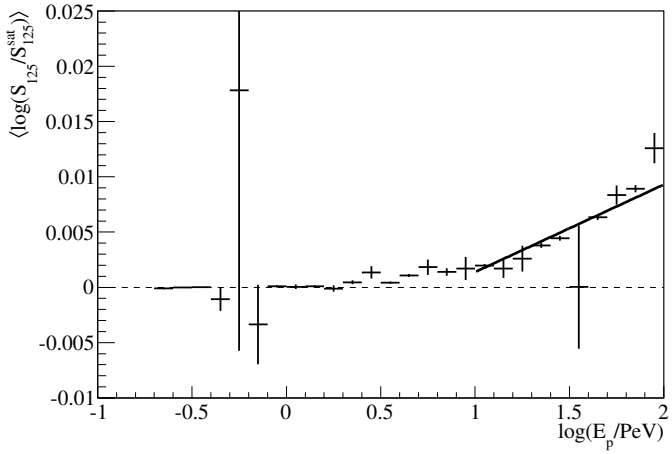

Figure 6.9.: Change in shower size as a function of energy when applying an artificial saturation value of $S_{max} = 3000\,\mathrm{VEM}$ in order to bring the charge spectra in data and Monte Carlo simulations into agreement, see Fig. 6.8.

6.3. Shower reconstruction

6.3.1. Reconstruction method

An assumption made in shower reconstruction is the correlation coefficient ξ of tanks in the P_{nohit} term of the likelihood function, Eq. (3.18). Tank signal fluctuations were assumed to be uncorrelated, corresponding to $\xi = 0$. In order to determine the systematic error introduced by this assumption, the other extreme case $\xi = 1$, was studied in data and simulation, as shown in Fig. 6.10. Since the ratio between the numbers of triggered and untriggered stations increases with energy, the importance of the P_{nohit} term decreases with increasing primary energy, leading to a decreasing influence of the choice of ξ on S_{125}.

The influence on shower size at low energies itself does not constitute a systematic error, as the same behavior is reproduced in simulation. In the lower panel of Fig. 6.10 the logarithm of the Monte Carlo to data ratio is shown:

$$\Delta \log\left(S_{125}^{(\xi=1)}/S_{125}^{(\xi=0)}\right) = \log\left(S_{125}^{(\xi=1)}/S_{125}^{(\xi=0)}\right)_{\text{MC}} - \log\left(S_{125}^{(\xi=1)}/S_{125}^{(\xi=0)}\right)_{\text{data}}. \quad (6.16)$$

From $\Delta \log\left(S_{125}^{(\xi=1)}/S_{125}^{(\xi=0)}\right) < 0.002$ above the detector threshold it can be concluded using Eq. (5.8) that the systematic error on energy reconstruction is less than 0.5%.

6.3.2. Quality cuts

Differences in passing rates of quality cuts described in Section 3.4 when applied to experimental and simulated data lead to a systematic uncertainty on the reconstruction efficiency and consequently on the flux normalization. Passing rates of all cuts for data and Monte Carlo events above threshold are listed in Table 4.4. There is a relative difference of 3.0% between data and Monte Carlo in the total cumulative passing rate, which was included in the systematic uncertainty on the flux.

6.4. Different interaction models

Small simulation datasets of proton and iron showers created using the high energy hadronic interaction models QGSJET-II and EPOS 1.99 were used to estimate the systematic uncertainty due to the modeling of hadronic interactions. Figure 6.11 shows the shower size ratio between SIBYLL and the alternative simulations as a function of primary energy for the two-component primary composition assumption and zenith angles up to 30°. Simulations with SIBYLL seem to yield systematically smaller shower sizes, and the same observation was made for more inclined showers.

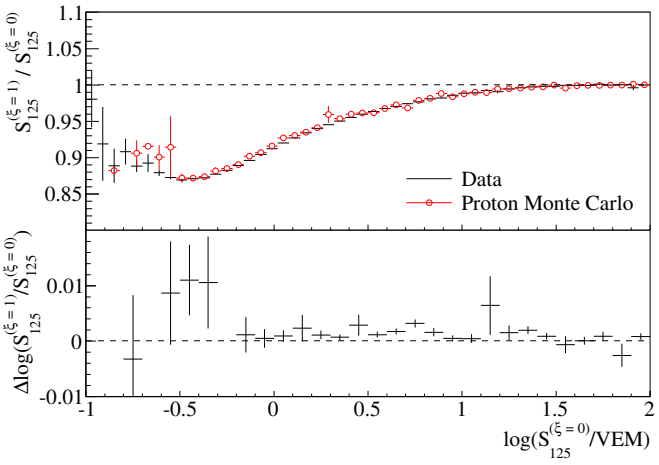

Figure 6.10.: Influence of the correlation coefficient ξ of tanks in the P_{nohit} term of the likelihood function, Eq. (3.18), on the reconstructed shower size in data and proton simulation. In the lower panel the logarithm of the Monte Carlo to data ratio is shown.

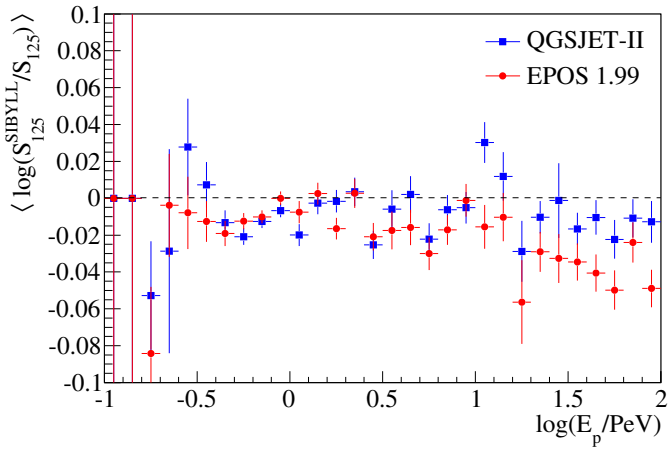

Figure 6.11.: Shower size ratio for the two-component assumption between SIBYLL and QGSJET and EPOS based Monte Carlo simulations for the two component primary assumption and showers with zenith angles up to 30°.

From the differences between SIBYLL and the other two interaction models, the following errors on primary energy determination were derived:

$$\Omega_1: \quad 2.1\%, \qquad \Omega_2: \quad 4.3\%, \quad \text{and} \quad \Omega_3: \quad 2.0\%. \tag{6.17}$$

The systematic error derived here is purely based on a comparison of interaction models. All of these models have different known strengths and weaknesses in their description of the underlying physics. Additionally, they all include an extrapolation to energy ranges not accessible by current collider experiments which are relevant in the first few cosmic ray interactions. This leads to the possibility of an unknown systematic error if correct behavior is not covered by the variation observed between different hadronization models.

6.5. Unfolding

6.5.1. Response matrix

Limited Monte Carlo statistics lead to uncertainties in the determination of the response matrix. Assuming the efficiency is constant above the threshold, the flux error induced by uncertainties of the detector response can be estimated by the fit error on ε_0 in Eq. (5.11) in case of the two-component composition assumption:

$$\Omega_1: \quad 0.9\%, \qquad \Omega_2: \quad 1.6\%, \quad \text{and} \quad \Omega_3: \quad 1.2\%. \tag{6.18}$$

The uncertainties on the parameters a_0 and b_0 in Equations (5.9) and (5.10) in case of the two-component model translate to an uncertainty on the energy in the unfolding process:

$$\Omega_1: \quad 0.7\%, \qquad \Omega_2: \quad 1.2\%, \quad \text{and} \quad \Omega_3: \quad 0.8\%. \tag{6.19}$$

These statistical uncertainties on the response matrix were also included in the systematic error of the final result.

Additionally, the flux model used in the simulation also influences the response matrix. A harder spectrum leads to larger average shower sizes in an energy bin than a softer one as shown in Fig. 6.12. In the figure simulations based on an E^{-2} flux and an E^{-4} flux were compared with the standard simulation which assumes a power law of E^{-3}. Above the threshold this difference appears to be independent of primary energy. In the three zenith angle ranges the following average differences in shower size between the two extreme spectral indices were found above $E_p = 1\,\text{PeV}$:

$$\Omega_1: \Delta \log S_{125} = 0.0033, \quad \Omega_2: \Delta \log S_{125} = 0.0044, \quad \Omega_3: \Delta \log S_{125} = 0.0045. \tag{6.20}$$

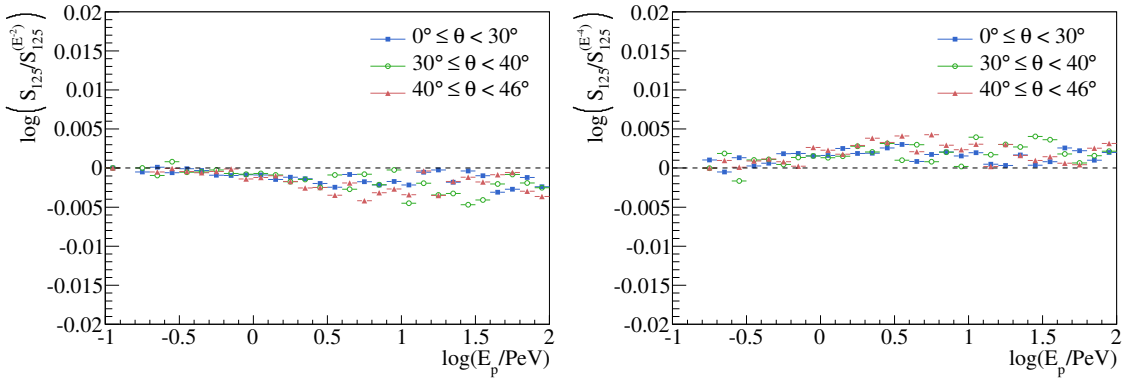

Figure 6.12.: Difference in logarithmic shower size between the standard Monte Carlo (flux $\propto E^{-3}$) and differently weighted simulations assuming an E^{-2} flux (left) and an E^{-4} flux (right).

Using Eq. (5.8) this leads to the following systematic errors on energy:

$$\Omega_1: \quad 0.73\%, \qquad \Omega_2: \quad 0.97\%, \quad \text{and} \quad \Omega_3: \quad 0.99\%. \tag{6.21}$$

6.5.2. Unfolding method

Two parameters besides the response matrix that influence the result of the unfolding are: the termination criterion $\Delta\chi^2_{\text{max}}$ and the prior distribution P_0. Since $\Delta\chi^2_{\text{max}}$ was determined in a toy simulation by comparing unfolding results to a true spectrum, the uncertainty on that number is defined as the range within which the χ^2 between the true and the unfolded spectrum increases by 1 from the overall minimum. Varying the termination criterion within this range lead to the following variation of the total flux:

$$\Omega_1: \quad 1.3\%, \qquad \Omega_2: \quad 3.2\%, \quad \text{and} \quad \Omega_3: \quad 5.1\%. \tag{6.22}$$

Varying the spectral index of the initial prior P_0 between -2.5 and -3.5, a variation of the total flux of about 2% was observed, see Fig. 6.13. This was added in quadrature to the numbers above. Below the knee region around 3 to 4 PeV, the spectral index seems to depend on the prior (in the most inclined zenith interval even up to 10 PeV. Varying the prior lead to a variation of the spectral index below the knee in the most vertical zenith band by ±0.01, and in the most inclined zenith range by ±0.025. At higher energies variations appear to be purely statistical.

6.6. Primary composition

Assuming pure proton and pure iron are the most extreme cases of the primary composition, the systematic uncertainty on the energy arising from the unknown

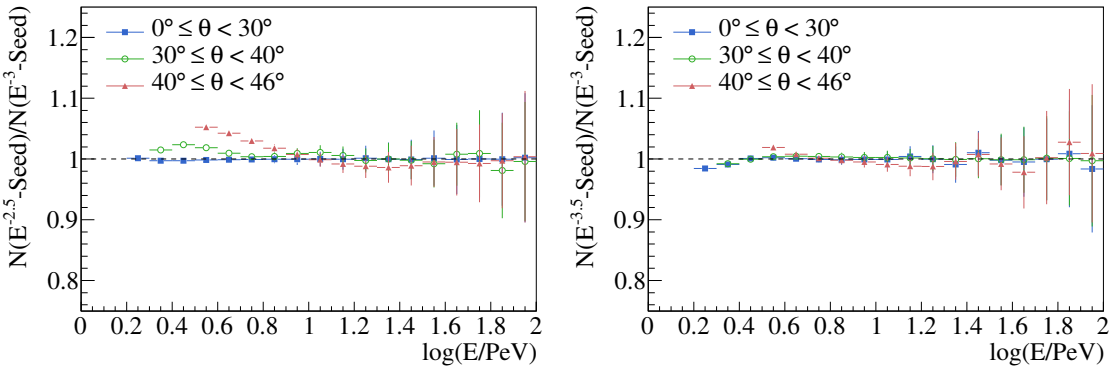

Figure 6.13.: Variation of the prior in the unfolding. *Left:* Ratio between the flux obtained with $P_0 \propto E^{-2.5}$ and the result obtained with the default E^{-3} prior, in case of the two-component assumption. *Right:* Comparison of the results obtained with $P_0 \propto E^{-3.5}$ to the default prior.

Table 6.1.: Shower size differences and resulting systematic errors on energy due to the unknown composition.

	$E \leq 10\,\mathrm{PeV}$		$E > 10\,\mathrm{PeV}$	
	Proton – 2 Components		Proton – Iron	
Zenith	$\langle \Delta \log S_{125} \rangle$	Syst. error	$\langle \Delta \log S_{125} \rangle$	Syst. error
Ω_1	0.0309(23)	7.0%	0.013(4)	2.9%
Ω_2	0.049(5)	11.3%	0.075(6)	17.9%
Ω_3	0.053(6)	12.3%	0.115(8)	28.7%

primary composition can be estimated from Fig. 5.10. Furthermore, as will be shown later, we can exclude pure iron at least below 10 PeV. Therefore, it is not included when determining the systematic uncertainty below energies of 10 PeV but only the difference between proton and the two-component model. Table 6.1 lists the shower size differences between different models and resulting systematic uncertainties.

6.7. Summary of systematic errors

Systematic uncertainties are summarized in Table 6.2.

The total systematic uncertainty was determined by quadratically adding the individual contributions. The error on the determination of the primary energy in the most vertical zenith angle range is 8.7% below $E_p = 10\,\mathrm{PeV}$, and 6.4% above. Main contributions are the unknown primary mass composition (7.0% below 10 PeV), and the variation of the atmosphere (2.6%). Furthermore, a flux uncertainty of 3.5% is caused by differences in cut efficiencies between data and Monte

Table 6.2.: Summary of systematic uncertainties of the energy and flux determination in the three zenith angle intervals Ω_1, Ω_2, and Ω_3. The different points are explained in the text. The total systematic error is the quadratic sum of all contributions. The error labeled 'Independent' at the bottom is the total systematic error excluding those contributions that have the same effect on all zenith angle intervals and the contribution from the unknown composition.

	$0° \leq \theta < 30°$		$30° \leq \theta < 40°$		$40° \leq \theta < 46°$	
Uncertainty	**Energy**	**Flux**	**Energy**	**Flux**	**Energy**	**Flux**
Snow height	0.4%		0.4%		0.4%	
Atmosphere variation	2.6%		2.7%		3.3%	
Atmosphere model	0.9%		1.1%		0.6%	
Saturation, $E_p \leq 10\,\mathrm{PeV}$	0.5%		0.5%		0.5%	
Saturation, $E_p > 10\,\mathrm{PeV}$	2.5%		2.5%		2.5%	
Droop	1.5%		1.5%		1.5%	
MC Calibration	1.5%		1.5%		1.5%	
Calibration stability	3.0%		3.0%		3.0%	
Reconstruction	0.5%		0.5%		0.5%	
Interaction model	2.1%		4.3%		2.0%	
Composition, $E_p \leq 10\,\mathrm{PeV}$	7.0%		11.3%		12.3%	
Composition, $E_p > 10\,\mathrm{PeV}$	2.9%		17.9%		28.7%	
Flux model	0.7%		1.0%		1.0%	
$\langle \log S \rangle$ and $\sigma_{\log S125}$	0.7%		1.2%		0.8%	
Cut passing rates		3.0%		3.0%		3.0%
Efficiency		0.9%		1.6%		1.2%
Unfolding procedure		1.6%		3.4%		5.2%
Total: $E_p \leq 10\,\mathrm{PeV}$	**8.7%**	**3.5%**	**13.1%**	**4.8%**	**13.5%**	**6.1%**
$E_p > 10\,\mathrm{PeV}$	**6.4%**	**3.5%**	**19.2%**	**4.8%**	**29.3%**	**6.1%**
Independent: $E_p \leq 10\,\mathrm{PeV}$	**3.7%**	**1.8%**	**5.5%**	**3.8%**	**4.3%**	**5.4%**
$E_p > 10\,\mathrm{PeV}$	**4.4%**	**1.8%**	**6.0%**	**3.8%**	**4.9%**	**5.4%**

Carlo, the efficiency calculation in Monte Carlo, and the termination criterion and seed in the unfolding procedure.

In addition to the total systematic error, the Table 6.2 lists those systematic errors that apply to different zenith angle intervals independently. From this error the following contributions were excluded:

- calibration of the simulation, calibration stability, and droop because these apply to all zenith angle ranges in the same way;
- and the uncertainty due to unknown composition because it only applies to the final result.

This individual systematic error needs to be taken into account when comparing spectra from different zenith angle ranges.

7. The cosmic ray energy spectrum

Using the method described before, the shower size spectra obtained from the air shower measurement and reconstruction presented in Chapter 3 were unfolded in order to obtain the primary cosmic ray energy spectrum. This was done independently for the three zenith angle ranges defined in Eq. (3.29):

$$\Omega_1 : 0^\circ \leq \theta < 30^\circ, \qquad \Omega_2 : 30^\circ \leq \theta < 40^\circ, \quad \text{and} \quad \Omega_3 : 40^\circ \leq \theta < 46^\circ.$$

Five different models of the primary mass composition were used as input to the unfolding procedure.

All unfolded spectra are shown in Figures 7.1 and 7.2. The lower end of the energy range was chosen as specified in Section 5.3.5 based on a 90% efficiency threshold. The spectra were cut off at 100 PeV, since Monte Carlo simulations of higher energies were not available. A binning of 10 bins per decade in energy was chosen based on the energy resolution.

In Section 5.5 it was shown that the difference in shower size between proton and iron showers increases with zenith angle due to the increasing slant depth of the atmosphere: showers initiated by heavy primary particles are attenuated more strongly with increasing slant depth than proton showers. Since one can safely assume that the cosmic ray flux is isotropic (at the level of sensitivity of this analysis) the flux measured in the different zenith angular intervals has to be the same.

In case of the pure proton assumption, Fig. 7.1(a), a good agreement between the three spectra is observed. On the other hand, in case of the assumption of pure iron, Fig. 7.1(b), the individual spectra for the three different zenith bands clearly disagree at low energies while they start to converge toward higher energies. This will be discussed more quantitatively later.

Agreement of the three spectra in case of the two-component model, Fig. 7.2(a), is good at low and high energies. In the intermediate energy range there is some deviation between the spectrum obtained from the steepest zenith angle interval and the other two spectra. However, they are still consistent when considering systematic errors. When using the poly-gonato model, Fig. 7.2(b), or the results from the IceTop/IceCube coincident events analysis, Fig. 7.2(c), as input, the spectra obtained in different zenith ranges disagree above the knee. The order of the spectra is consistent with the fact that in those two cases $\langle \ln A \rangle$ is larger than for the two-components model, i. e. attenuation is over-compensated. Possible reasons for this disagreement will be discussed in Section 8.2.

In case of the pure iron assumption a χ^2 test was used in order to quantify the

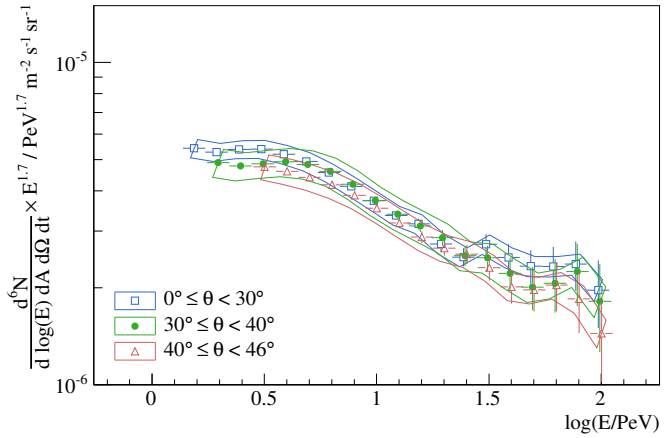

(a) Proton

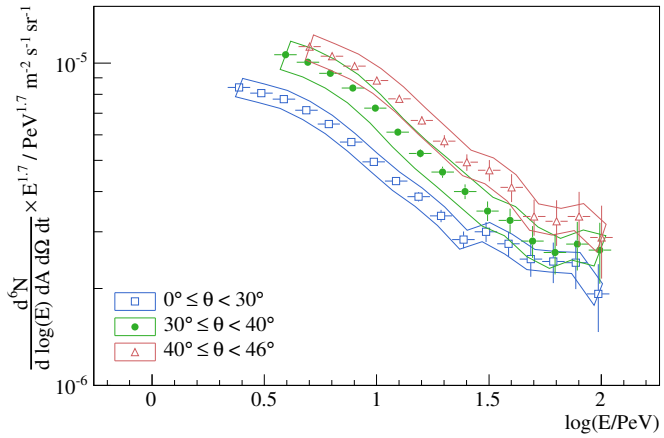

(b) Iron

Figure 7.1.: Unfolded energy spectra assuming pure proton or iron primary particles. The lines indicate the individual systematic errors of the different zenith ranges, i. e. excluding all contributions that are expected to have the same effect on all three spectra, and excluding the systematic error due to primary composition.

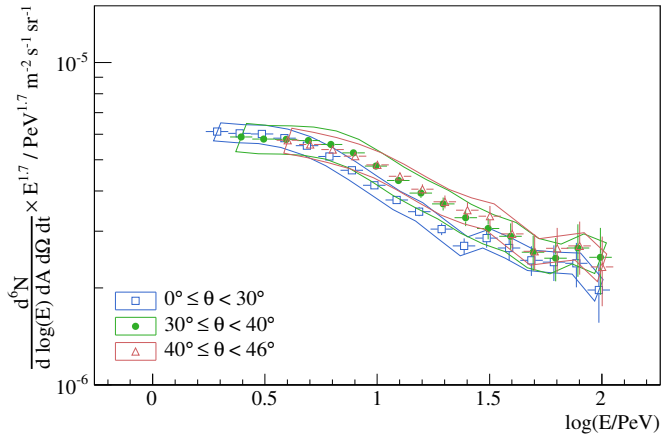

(a) Two Components

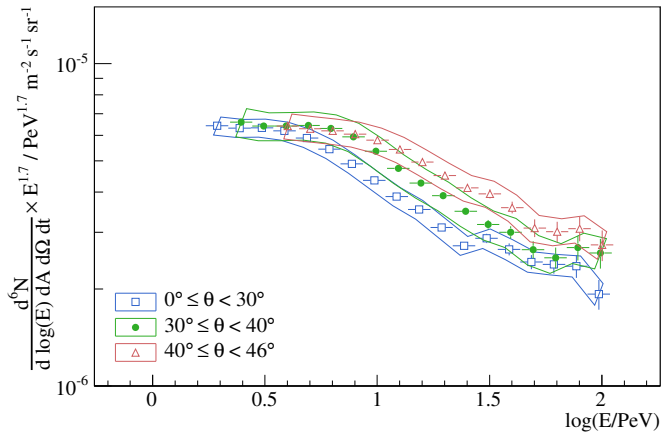

(b) Poly-gonato

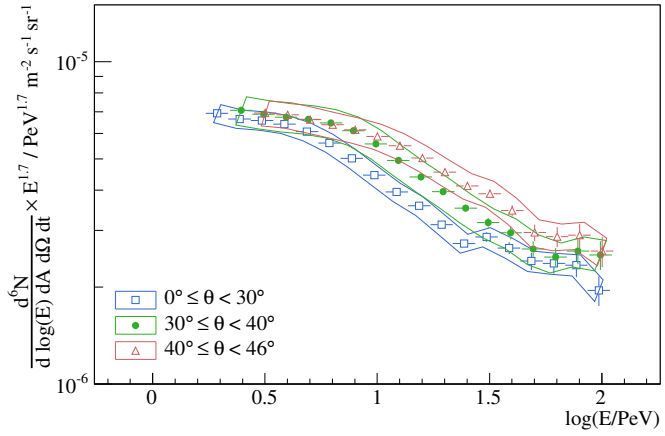

(c) IceTop/IceCube-40 Coincidences

Figure 7.2.: Unfolded energy spectra using three different mixed composition assumptions. See Fig. 7.1 for an explanation of the systematic error bands.

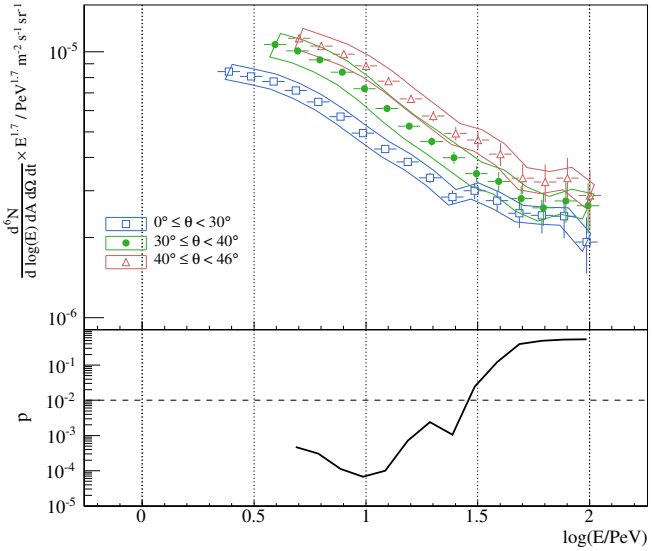

Figure 7.3.: *Upper panel:* the three spectra obtained under the pure iron assumption as in Fig. 7.1(b). *Lower panel:* Probability p that the three spectra agree given the observed statistical and systematic uncertainties.

disagreement between spectra from different zenith ranges. In each energy bin the χ^2 probability was calculated that the three points from the different zenith angles are due to the same mean. Systematic errors were added quadratically to the statistical error, because of a lack of knowledge about the correct distribution. Furthermore, the systematic error on energy $\Delta \log E = \Delta E/(E \ln 10)$ was transformed into an error on the flux $\Delta N/N = \ln(10)\Delta \log N$ based on the local spectral index $\tilde{\gamma}$:

$$\Delta \log N = \tilde{\gamma} \Delta \log E, \tag{7.1}$$

where $\tilde{\gamma}$ was determined from the change in flux between consecutive energy bins. The result is shown in Fig. 7.3. Below 27 PeV, agreement of the spectra from pure iron can be excluded at a 99% confidence level assuming that systematic errors can be described by a normal distribution and that they are independent in different zenith angle ranges. This is a conservative estimate, since systematic errors in different zenith angle intervals are most likely positively correlated. Based on this study, pure iron was excluded from the estimation of the systematic error arising from the unknown primary composition below $E = 25$ PeV ($\log(25) = 1.40$).

Figure 7.5 compares the unfolded spectra in zenith range Ω_1 ($0° \leq \theta < 30°$) obtained under pure proton, pure iron, and the two-component assumption. Because the difference in shower size between proton and iron decreases toward higher energies (see Fig. 5.10) the spectrum obtained under the iron assumption is softer than the proton-based result. All three spectra show a steepening between 3 PeV and 5 PeV, and a slight flattening around 28 PeV.

The three spectra in case of the pure proton and the two-component primary

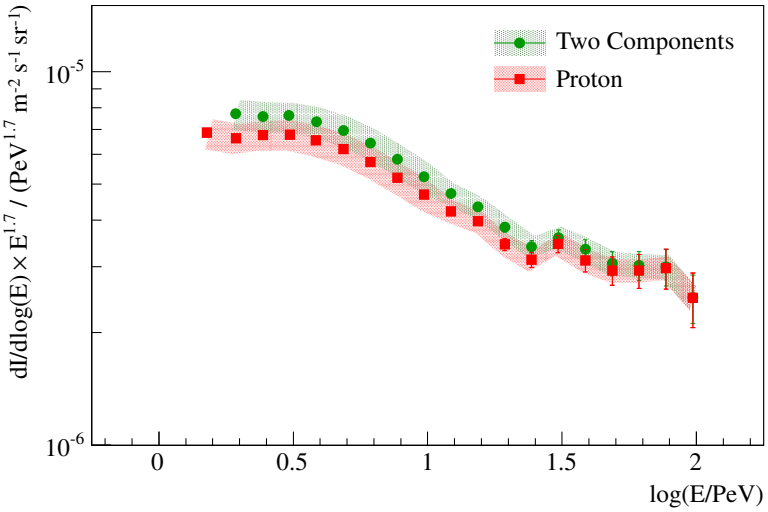

Figure 7.4.: All-particle primary energy spectrum based on the two-component composition assumption derived from showers with $0° \leq \theta < 30°$. The shaded bands indicate the systematic uncertainty ranges.

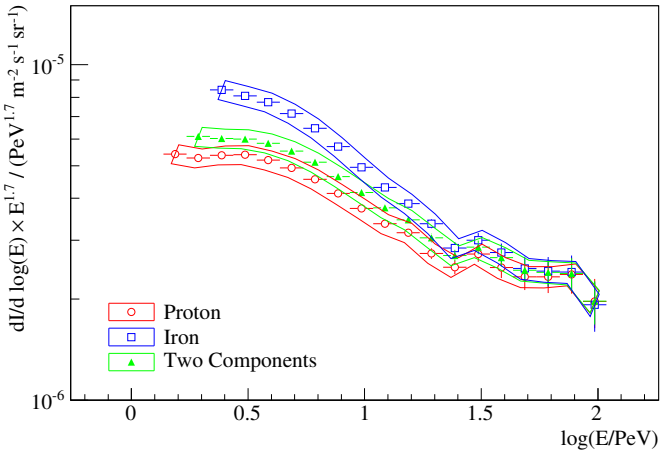

Figure 7.5.: Unfolded spectra in zenith range Ω_1 ($0° \leq \theta < 30°$) assuming pure proton, pure iron, and the two-component model. The boxes indicate the systematic errors as in Fig. 7.1.

composition assumptions both appear to be in good agreement. It was decided to use only spectra from zenith interval Ω_1 ($0^\circ \leq \theta < 30^\circ$) in the final result because systematic errors in this zenith range are smallest, especially the uncertainty due to primary composition. The spectra derived from these two primary composition assumptions from showers in this zenith angle interval are shown in Fig. 7.4 together with the full systematic error range given in Table 6.2. All data points together with their statistical uncertainties can be found in Appendix A.

In order to find the best-fit position of the knee and the spectral indices above and below the knee, the spectra were fit with function (4.8) expressed in terms of the flux at the knee:

$$\frac{\mathrm{d}N}{\mathrm{d}\log E} = \frac{I_{\mathrm{knee}}}{2^{\Delta\gamma/\varepsilon}} \left(\frac{E}{E_{\mathrm{knee}}}\right)^{\gamma_1+1} \left(1 + \left(\frac{E}{E_{\mathrm{knee}}}\right)^{\varepsilon}\right)^{\Delta\gamma/\varepsilon}, \tag{7.2}$$

where I_{knee} is the flux at the knee energy E_{knee}. Errors and correlations between data points obtained from the bootstrap method described in Section 5.3.3 were taken into account. Two cases were considered:

- the whole range from threshold up to $E = 100\,\mathrm{PeV}$ was fit;
- only the range from the threshold up to the flattening at $\log(E/\mathrm{PeV}) = 1.44$ (corresponding to $E = 27.5\,\mathrm{PeV}$) was fit.

The results are summarized in Table 7.1. When fitting only up to the flattening at $\log(E/\mathrm{PeV}) = 1.44$ a clear improvement in χ^2/N_{dof} can be observed compared to the fit of the full energy range. The bad χ^2 value in case of the proton fits is caused by the dip between the first and the fourth data point (potentially hinting at an underestimation of correlations between data points). The spectral index below the knee, γ_1, and the position of the knee, E_{knee}, are hardly affected by the choice of fit range. The change in spectral index at the knee, $\Delta\gamma$, increases when limiting the energy range of the fit, and the shape of the knee becomes softer (ε becomes smaller).

The systematic error of the knee energy is the systematic error of the energy determination at that primary energy as given in Chapter 6, however, excluding the contribution from the unknown composition, since these are fits of specific composition models. The systematic error of I_{knee} is the quadratic sum of the systematic error on the flux, ΔN, and the error on the energy, $\Delta \log E$, transformed into a flux uncertainty:

$$(\Delta \log I_{\mathrm{knee}})^2 = \left(\left.\frac{\mathrm{d}\log N}{\mathrm{d}\log E}\right|_{E=E_{\mathrm{knee}}} \Delta \log E(E_{\mathrm{knee}}) \right)^2 + (\Delta \log N)^2, \tag{7.3}$$

with

$$\Delta \log N = \frac{\Delta N}{N \ln(10)} \tag{7.4}$$

Table 7.1.: Fit parameters of the cosmic-ray energy spectrum according to function (7.2) for the pure proton and two-component model primary composition assumptions. Systematic errors were derived as described in the text and exclude the systematic error due to the unknown composition, since these are fits of spectra derived under specific composition assumptions. The proton fit contains one additional data point at lower energy.

(a) Proton

Parameter	Full range fit		
$I_{\text{knee}}/10^{-7}\,\text{m}^{-2}\,\text{s}^{-1}\,\text{sr}^{-1}$	5.0	± 0.3(stat)	± 0.5(syst)
γ_1	−2.714	± 0.007(stat)	± 0.020(syst)
$E_{\text{knee}}/\text{PeV}$	3.97	± 0.13(stat)	± 0.17(syst)
$\Delta\gamma$	−0.364	± 0.014(stat)	± 0.018(syst)
ε	12	± 4(stat)	
χ^2/N_{df}	82.3/14		
Parameter	**Fit up to $\log(E/\text{PeV}) = 1.44$**		
$I_{\text{knee}}/10^{-7}\,\text{m}^{-2}\,\text{s}^{-1}\,\text{sr}^{-1}$	4.5	± 0.3(stat)	± 0.4(syst)
γ_1	−2.714	± 0.008(stat)	± 0.020(syst)
$E_{\text{knee}}/\text{PeV}$	4.22	± 0.15(stat)	± 0.18(syst)
$\Delta\gamma$	−0.406	± 0.020(stat)	± 0.06(syst)
ε	9.2	± 2.3(stat)	
χ^2/N_{df}	58.1/8		

(b) Two Components

Parameter	Full range fit		
$I_{\text{knee}}/10^{-7}\,\text{m}^{-2}\,\text{s}^{-1}\,\text{sr}^{-1}$	5.01	± 0.28(stat)	± 0.5(syst)
γ_1	−2.742	± 0.012(stat)	± 0.021(syst)
$E_{\text{knee}}/\text{PeV}$	4.20	± 0.12(stat)	± 0.18(syst)
$\Delta\gamma$	−0.365	± 0.017(stat)	± 0.09(syst)
ε	9.3	± 2.5(stat)	
χ^2/N_{df}	29.4/13		
Parameter	**Fit up to $\log(E/\text{PeV}) = 1.44$**		
$I_{\text{knee}}/10^{-7}\,\text{m}^{-2}\,\text{s}^{-1}\,\text{sr}^{-1}$	4.5	± 0.3(stat)	± 0.4(syst)
γ_1	−2.734	± 0.015(stat)	± 0.022(syst)
$E_{\text{knee}}/\text{PeV}$	4.47	± 0.16(stat)	± 0.19(syst)
$\Delta\gamma$	−0.419	± 0.029(stat)	± 0.08(syst)
ε	6.4	± 1.6(stat)	
χ^2/N_{df}	4.7/7		

and

$$\left.\frac{\mathrm{d}\log N}{\mathrm{d}\log E}\right|_{E=E_{\mathrm{knee}}} = 1 + \gamma_1 + \frac{\Delta\gamma\,(E_{\mathrm{knee}}/\mathrm{PeV})^{\varepsilon}}{1+(E_{\mathrm{knee}}/\mathrm{PeV})^{\varepsilon}}. \tag{7.5}$$

Due to the power law shape of the cosmic ray energy spectrum, the transformation between energy and flux error was performed on a double logarithmic scale. Finally:

$$\frac{\Delta I_{\mathrm{knee}}}{I_{\mathrm{knee}}} = \ln(10)\cdot\Delta\log I_{\mathrm{knee}}. \tag{7.6}$$

In order to determine systematic errors on γ_1 and $\Delta\gamma$, the upper and lower boundary of the systematic error band were fit with the same function. The dominant contribution to the systematic error of γ_1, however, is the the uncertainty from the unfolding prior (see Section 6.5.2), which was added quadratically.

Under the assumption that the change in spectral index at $\log(E/\mathrm{PeV}) = 1.44$ is not a detector artifact, the spectra were fitted above this energy range, obtaining the following spectral indices:

$$\begin{array}{ll} \text{Proton:} & \gamma_3 = -2.93 \pm 0.11, \\ \text{Two Components:} & \gamma_3 = -2.97 \pm 0.09, \end{array} \tag{7.7}$$

which are both clearly flatter than the indices below $\log(E/\mathrm{PeV}) = 1.44$.

8. Discussion and outlook

8.1. Comparison with other experiments

Figure 8.1 shows a comparison of the primary energy spectra obtained in this thesis under the pure proton and the two-component primary composition assumption in comparison with several other experimental results. Quoted data are from: GAMMA (Garyaka et al., 2008); KASCADE-Grande (Haungs et al., 2009); Tibet (Amenomori et al., 2008); Tunka (Antokhonov et al., 2010; Wischnewski and Kuzmichev, 2011); and private communication with T. K. Gaisser (all other spectra). Furthermore, the results of fits of cosmic ray energy spectra by Erlykin and Wolfendale (2009) are listed in Table 8.1 together with the results of this thesis.

The variations between different experiments seen in Fig. 8.1 and Table 8.1 could be interpreted as a possible problem in the energy calibration of indirect cosmic ray measurements. Primary energy determination relies on Monte Carlo simulations and different hadronization models are used by different experiments. The systematic error due to these models may be different at the different altitudes where experiments are located. Furthermore, sensitivity of experiments to different components of an air shower depends on the detector technology used. All this can cause large variation of energy scales of different experiments.

The position of the knee of the cosmic ray energy spectrum, E_{knee}, found in this thesis is in agreement with the range of knee energies found by other experiments. KASCADE and Tibet found a slightly lower position of the knee, which judging from Fig. 8.1 can probably be explained by a discrepancy in the energy calibration between this measurement and KASCADE and Tibet. Additionally, the spectral index above the knee appears in very good agreement with the value found in this work. In case of Tunka and GAMMA, on the other hand, the knee is at larger energies than in case of our measurement, whereas the flux weighted with $E^{1.7}$ in Fig. 8.1 is lower. This could hint at some other systematic difference.

Several experiments have reported deviations from a single power law in the energy region between 10 and 100 PeV. GAMMA found a significant 'bump' in the all-particle spectrum between 60 and 80 PeV (Garyaka et al., 2008). This irregularity was interpreted as due to an additional iron component attributed to Pulsars with a very flat spectrum up to a cut-off at about 77 PeV. The Tunka experiment reports a change of the spectral index from about 3.2 to 3.0 at primary energies of about 20 PeV (Kuzmichev, 2011). Furthermore, they found a 'bump' between 80 and 100 PeV. It is thus at slightly higher energy than the feature seen by GAMMA, but this might be due to differences in the energy calibration.

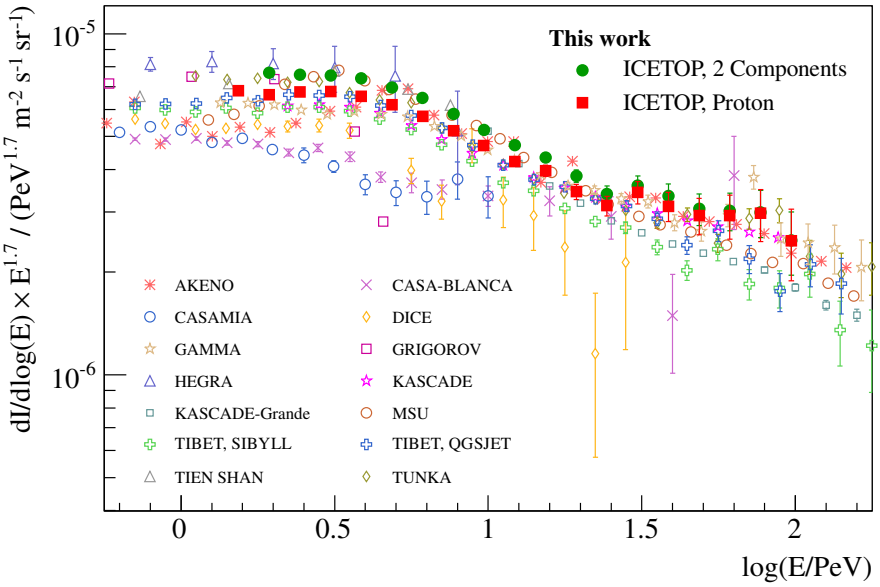

Figure 8.1.: Comparison of the results obtained in this thesis with a selection of other experiments (see text for references).

Table 8.1.: Results of fits of the cosmic ray energy spectrum in this thesis compared to other experiments (fits by Erlykin and Wolfendale, 2009): position of the knee, E_{knee}, spectral index below the knee, γ_1, and the change in spectral index at the knee, $\Delta\gamma$.

Experiment	E_{knee}/PeV	$-\gamma_1$	$-\Delta\gamma$
Tibet-III	3.89	2.64	0.48
KASCADE	3.55	2.60	0.49
GAMMA	5.75	2.76	0.32
Yakutsk	3.71	2.64	0.46
Maket-ANI	6.03	2.75	0.44
Tunka	4.37	2.59	0.75
IceTop (this work)			
Proton	3.97	2.71	0.36
2 Components	4.20	2.74	0.37

KASCADE-Grande also finds a spectral index above about 16 PeV that is flatter than $\gamma_2 \approx -3.1$ found directly above the knee by most experiments (Arteaga-Velázquez et al., 2010). They refer to this feature as a concavity around 10 PeV, but only have two data points below the flattening.

Erlykin and Wolfendale have analyzed the structure of the cosmic ray energy spectrum at the knee and above and give an interpretation of the visible features in the context of their single-source model (2009). By averaging spectra from several experiments they found a small irregularity at about 13 PeV. They suggest that, if the knee is due to a cut-off of helium, this irregularity could be interpreted as caused by nuclei of the CNO group. Then the structure above 30 PeV could be attributed to iron. Erlykin and Wolfendale remark that the existence of these structures and the sharpness of the knee supports their hypothesis of a single nearby source as the origin of cosmic rays, since in that case spectra would be much less affected by effects of propagation than in typical galactic diffusion models.

8.2. Comparison with previous IceTop results

Klepser (2008) has analyzed a subset of the IceTop data used in this thesis and developed many of the techniques used here. However, he also points out several deficiencies especially in the available simulation codes, most importantly the lack of an adequate treatment of snow on top of the tanks and discrepancies in the detector threshold. Many of these problems have been solved now. Due to these obvious differences mostly in the detector simulation, no quantitative comparison of the results will be made here.

More recently, an analysis of coincident events in IceCube and IceTop based on data taken with the 40 strings and 40 stations configuration has been completed (Andeen, 2011b). In this analysis, S_{125} as a measure of the shower size at the surface and a quantity describing the size of the muon bundle in IceCube (K_{70}) are used as inputs for a neural network. The output of this multivariate analysis are the primary energy and a quantity related to $\ln A$. In this way a measurement of the all-particle cosmic ray energy spectrum and of $\langle \ln A \rangle$ as a function of energy were obtained.

In this analysis, a relatively soft knee at $E_{\text{knee}} = 5.16 \pm 0.42$ PeV and spectral indices below and above the knee of 2.63 ± 0.07 and 3.35 ± 0.08 were found. The total flux found by Andeen (2011b) is in agreement within systematic errors with the flux obtained from the pure proton assumption in this thesis (see Fig. 8.2). However, it is generally below the best-fit points found in this work. Furthermore, the knee is at a higher energy, and the spectral slope is steeper above the knee. Additionally, the composition obtained in the analysis of coincident events, appears too heavy in this analysis (see Fig. 7.2(c)).

The analyses differed in the following aspects:

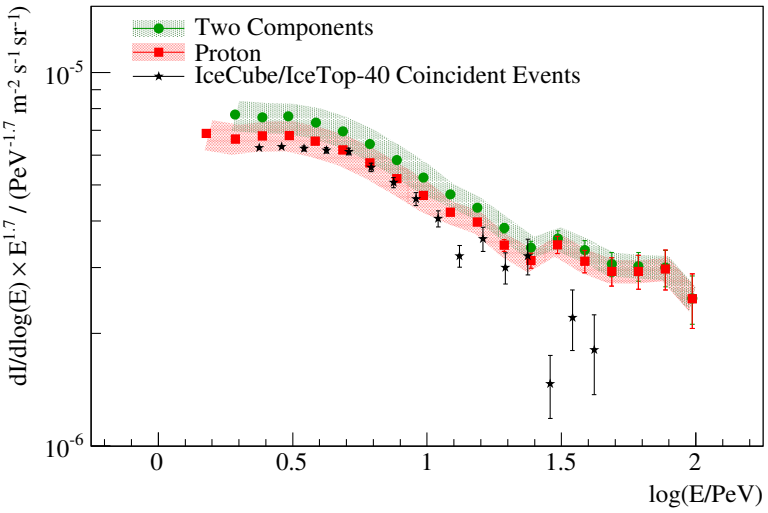

Figure 8.2.: Comparison of the results obtained in this thesis with the all-particle cosmic ray energy spectrum determined in the analysis of IceTop/IceCube coincident events by Andeen (2011b).

- The detector simulation used by Andeen was not based on Geant4 but on a parametrization of the light yield of different particles developed by Klepser (2008). These parametrizations did not take into account the snow on top of the IceTop tanks.

- Instead of simulating snow, Andeen developed a method to correct for the effects of snow in the lateral fit.

- The most obvious difference is the method used to obtain the primary energy from the measured quantities. However, when using the same description of the detector response, they should yield equivalent results. The only remaining difference in this respect is then the fact that in the multivariate analysis of coincident events, quantities measured by both IceTop and IceCube will contribute to the reconstructed primary energy.

The most likely reason for the differences between the results is the simulation of the IceTop detector, especially of the contribution for snow. The interpolation of shower sizes between January, 2007, and January, 2008, described in Section 5.4 bears some uncertainty. If the snow height or the effect of snow on shower sizes was overestimated, reconstructed energies in this analysis could be overestimated. In addition, since the effect of snow is larger for inclined showers, overestimating the effect of snow would lead to an overestimation of shower attenuation with increasing zenith angle in simulation. This would lead to the opposite effect when reconstructing experimental data and ultimately an underestimate of the best fit mass composition from the comparison of spectra in different zenith angle

ranges. Therefore, an overestimation of snow could explain the discrepancy of spectra visible in Fig. 7.2(c) when using the results from Andeen (2011b) as input to the unfolding procedure. Another possibility that cannot be ruled out at this point is of course that the interaction models used (in both analyses SIBYLL and Fluka) do not correctly describe the relation between the electromagnetic component of an air shower, and its development, and the size of the muon bundle in the ice.

8.3. Outlook

The analysis performed in this thesis is a continuation and extension of the work done by Stefan Klepser (2008). Since then, the simulation of the IceTop detector has improved greatly, especially through the use of Geant4 to simulate the tanks. Furthermore, simulation of the VEM calibration spectrum based on methods developed by Van Overloop (2010) allowed a precise calibration of the simulated tanks. Composition sensitivity of the shower size development with increasing zenith angle has been confirmed with the improved understanding of our detector, increasing the confidence in the validity of the method.

The measurement of the snow height is a source of systematic error that will be eliminated in future analyses using the method developed by Rawlins (2011) and Kuwabara and Tilav (2011). In addition, using a method developed by Andeen (2011b), snow can be corrected for in the event reconstruction. In this way, future analysis could cover long data taking periods without introducing systematic errors or shifts (see Section 5.4) due to differences in the simulated and the actual snow depths. This, however, would require a confirmation of the parameters used to correct for the snow in simulation, which in turn would increase the confidence in our detector simulation.

The agreement between data and simulation discussed in Section 4.6 of this thesis is quite good. However, there is a striking disagreement between data and Monte Carlo simulations in the χ^2 distributions, which needs to be understood and improved. Signal fluctuations have been studied (Kislat, 2007), but since that time the IceTop detector has grown considerably, the accessible energy range has increased, and there have been great improvements in the detector calibration. Therefore, at some point these studies will have to be redone and extended to larger signals of several hundred VEM.

The description of the shower front curvature and the arrival time distribution also bears some room for improvement. Especially, it should be studied if the curvature contains some information on primary composition.

The main goal of IceTop is the measurement of the primary composition using coincident events in IceTop and IceCube. This method alone, however, depends greatly on simulations of air showers, and hadronic interaction models are one of the main sources of systematic errors. In this thesis, a measurement of coincident events has for the first time been compared to a systematically independent measure of the primary composition, revealing some unexplained discrepancies. Such

comparisons can help improving the understanding of the IceTop/IceCube detector and may at some point allow IceTop to help improving hadronic interaction models.

Besides the method described here and the measurement of coincident events with IceCube, IceTop offers further methods to determine cosmic ray composition. While in this thesis the zenith angle development of shower sizes was only used to judge on a range of a-priori composition assumptions, it could in principle be extended to determine the best-fit mean logarithmic mass as a function of energy. Further, it has been shown that muons can be identified in IceTop air shower signals (Lucke, 2008) and that their number is sensitive to primary composition (Birr, 2010). Exploiting SLC pulses (simple charge stamps transmitted by DOMs if the local coincidence condition is not satisfied) will enhance the capability of IceTop to detect single muons. Furthermore, as shown in Section 5.5.3, the slope parameter β of the lateral distribution function (3.6) is sensitive to primary mass. Also, the curvature of the shower front, which still needs to be studied in detail, might carry information on primary mass.

Given this large number of mass-sensitive parameters, IceTop should be capable to make most precise measurements of the primary energy spectrum and mass composition in the PeV to EeV energy range.

9. Summary

The main goal of this thesis was the measurement of the primary energy spectrum of cosmic rays using data taken with the IceTop air shower array at the geographic South Pole. Air showers were reconstructed by fitting the lateral charge and arrival time distributions as described in Chapter 3. The signal expectation value S_{125} at a distance of 125 m from the shower axis was used as a measure of the shower size. Shower size spectra were determined in three different zenith angle intervals,

$$\Omega_1: \quad [0^\circ, 30^\circ], \qquad \Omega_2: \quad [30^\circ, 40^\circ], \quad \text{and} \quad \Omega_3: \quad [40^\circ, 46^\circ].$$

In order to relate the measured shower sizes to primary energies, air shower simulations were carried out using the software package CORSIKA as described in Chapter 4. The results of these simulations were then fed into a detailed simulation of the IceTop detector. However, since the air shower simulation with CORSIKA is the most time consuming part of the simulation chain, air showers were resampled several times. Care had to be taken to not use a single shower too often, in order to avoid artificial fluctuations. The IceTop detector was then simulated using a custom detector simulation based on the Geant4 package. Since the relation between shower size and primary energy depends on the mass of the primary particle, showers initiated by five different particle species were simulated: hydrogen, helium, nitrogen, silicon, and iron.

From these simulations the response of the detector to primary particles with primary energies between 100 TeV and 100 PeV has been determined. The detector response was described using a response matrix, which was characterized by the mean logarithmic shower size, $\langle \log S_{125} \rangle$, of showers in a given range of primary energies, the shower size resolution and the detection efficiency. Response matrices were determined for each zenith angle interval Ω_k under five different assumptions on the primary mass composition (see Section 4.5): pure proton, pure iron, the two-component model, the poly-gonato model, and results from a measurement of the chemical composition of cosmic rays using coincident events in the IceTop and IceCube detector. Using these response matrices and an iterative unfolding method based on Bayes' Theorem, the shower size spectra were unfolded in Chapter 5 in order to obtain primary energy spectra.

In Chapter 7, the results obtained under different assumptions on the primary mass composition were presented. Since there is no indication for anisotropy in the flux of cosmic rays at the energies studied in this thesis, spectra measured in different zenith angle ranges should agree at the level of sensitivity of this analysis.

This fact was exploited to exclude the assumption of pure iron composition. The best agreement of spectra from the three zenith ranges has been obtained with the pure proton and the two-component primary composition assumption. Because systematic uncertainties (studied in Chapter 6) are smallest in the most vertical zenith angle range ($\theta < 30°$), it was decided to base the final results only on data taken in this interval.

Fits of function (7.2) to the resulting spectra yielded the following parameters. The knee in the cosmic ray energy spectrum was found at:

$$\begin{aligned} &\text{Proton:} && E_{\text{knee}} = 3.97 \pm 0.13(\text{stat}) \pm 0.17(\text{syst})\,\text{PeV}, \\ &\text{Two-Component:} && E_{\text{knee}} = 4.20 \pm 0.12(\text{stat}) \pm 0.18(\text{syst})\,\text{PeV}. \end{aligned}$$

Below the knee the spectral index is:

$$\begin{aligned} &\text{Proton:} && \gamma_1 = -2.714 \pm 0.007(\text{stat}) \pm 0.001(\text{syst}), \\ &\text{Two-Component:} && \gamma_1 = -2.742 \pm 0.008(\text{stat}) \pm 0.004(\text{syst}), \end{aligned}$$

and above the knee:

$$\begin{aligned} &\text{Proton:} && \gamma_2 = -3.078 \pm 0.016(\text{stat}) \pm 0.018(\text{syst}), \\ &\text{Two-Component:} && \gamma_2 = -3.107 \pm 0.021(\text{stat}) \pm 0.09(\text{syst}). \end{aligned}$$

However, it was also found that independent of primary composition assumption the spectrum flattens at around 30 PeV and that a fit with a single power law above the knee is not possible. Above this energy a spectral index of -2.93 ± 0.11 was found in the pure proton case and of -2.97 ± 0.09 in case of the two-component model. Such a flattening and other structures have been found by previous experiments in the same energy range. However, in the case of IceTop, confirmation with a larger detector and simulations that extend to higher energies would be desirable.

Improved detector simulations and improvements in the calibration of the simulated IceTop tanks have lead to a much better understanding of the detector. Future analyses will profit from continuous monitoring of the snow depths on top of the IceTop tanks and by taking these snow depths into account in the likelihood function of the lateral fit. A main concern in future should be to improve the agreement of likelihood distributions in simulations and experimental data. A key to this could be extended studies of charge fluctuations. Another important point is to understand and describe the shape of the shower front which is related to the lateral distribution of signal times. Due to continuous improvement of the understanding of the detector and thanks to various systematically independent measures of primary energy and mass, IceTop should be able to make most precise measurements of the all-particle energy spectrum and mass composition of cosmic rays.

A. The all-particle spectrum

Table A.1.: Measured cosmic-ray flux as a function of energy obtained from air showers in with zenith angle $\theta < 30°$, assuming pure primary protons. Errors are statistical errors only, systematic uncertainties are listed in Table 6.2.

Energy / 10^6 GeV	Flux / $\mathrm{GeV}^{-1}\,\mathrm{m}^{-2}\,\mathrm{s}^{-1}\,\mathrm{sr}^{-1}$
1.5375	$(9.26 \pm 0.04) \cdot 10^{-13}$
1.9355	$(4.838 \pm 0.020) \cdot 10^{-13}$
2.4367	$(2.650 \pm 0.014) \cdot 10^{-13}$
3.0676	$(1.426 \pm 0.010) \cdot 10^{-13}$
3.8619	$(7.38 \pm 0.06) \cdot 10^{-14}$
4.8618	$(3.76 \pm 0.05) \cdot 10^{-14}$
6.1207	$(1.868 \pm 0.027) \cdot 10^{-14}$
7.7055	$(9.10 \pm 0.17) \cdot 10^{-15}$
9.7006	$(4.41 \pm 0.10) \cdot 10^{-15}$
12.212	$(2.13 \pm 0.07) \cdot 10^{-15}$
15.375	$(1.08 \pm 0.04) \cdot 10^{-15}$
19.355	$(5.01 \pm 0.26) \cdot 10^{-16}$
24.367	$(2.45 \pm 0.17) \cdot 10^{-16}$
30.676	$(1.44 \pm 0.11) \cdot 10^{-16}$
38.619	$(7.0 \pm 0.7) \cdot 10^{-17}$
48.618	$(3.6 \pm 0.5) \cdot 10^{-17}$
61.207	$(1.91 \pm 0.29) \cdot 10^{-17}$
77.055	$(1.04 \pm 0.18) \cdot 10^{-17}$
97.006	$(4.64 \pm 1.10) \cdot 10^{-18}$

Table A.2.: Measured cosmic-ray flux as a function of energy obtained from air showers in with zenith angle $\theta < 30°$, assuming a mixed primary composition according to the two-component model. Errors are statistical errors only, systematic uncertainties are listed in Table 6.2.

Energy / 10^6 GeV	Flux / $\mathrm{GeV}^{-1}\,\mathrm{m}^{-2}\,\mathrm{s}^{-1}\,\mathrm{sr}^{-1}$
1.5375	$(1.0875 \pm 0.0020) \cdot 10^{-12}$
1.9355	$(5.612 \pm 0.013) \cdot 10^{-13}$
2.4367	$(2.974 \pm 0.009) \cdot 10^{-13}$
3.0676	$(1.589 \pm 0.006) \cdot 10^{-13}$
3.8619	$(8.30 \pm 0.04) \cdot 10^{-14}$
4.8618	$(4.222 \pm 0.025) \cdot 10^{-14}$
6.1207	$(2.098 \pm 0.017) \cdot 10^{-14}$
7.7055	$(1.021 \pm 0.011) \cdot 10^{-14}$
9.7006	$(4.92 \pm 0.07) \cdot 10^{-15}$
12.212	$(2.38 \pm 0.05) \cdot 10^{-15}$
15.375	$(1.177 \pm 0.028) \cdot 10^{-15}$
19.355	$(5.58 \pm 0.17) \cdot 10^{-16}$
24.367	$(2.66 \pm 0.11) \cdot 10^{-16}$
30.676	$(1.51 \pm 0.08) \cdot 10^{-16}$
38.619	$(7.5 \pm 0.5) \cdot 10^{-17}$
48.618	$(3.72 \pm 0.29) \cdot 10^{-17}$
61.207	$(1.97 \pm 0.18) \cdot 10^{-17}$
77.055	$(1.05 \pm 0.12) \cdot 10^{-17}$
97.006	$(4.7 \pm 0.7) \cdot 10^{-18}$

B. Uncertainty of the detection efficiencies

The detection efficiency of air showers was were determined from simulations as

$$\varepsilon = \frac{\sum_{i=1}^{N_{\mathrm{rec}}} w_i}{\sum_{j=1}^{N_{\mathrm{gen,i}}} w_j}, \tag{B.1}$$

(see Section 5.2), where $N_{\mathrm{gen,i}}$ is the number of events generated inside the fiducial area, N_{rec} is the number of events in the final sample and w_i are the simulation weights. It can become larger than unity, if more events with a true core position outside the fiducial area migrate into that area than vice versa. That $\varepsilon > 1$ is possible needs to be taken into account when calculating the statistical error of ε.

First, ε was split into contributions from events with their true core inside and outside the array,

$$\varepsilon = \varepsilon_{\mathrm{i}} + R\,\varepsilon_{\mathrm{o}}, \tag{B.2}$$

with the respective detection efficiencies of contained events and of events outside the fiducial area,

$$\varepsilon_{\mathrm{i}} = \frac{\sum_{i=1}^{N_{\mathrm{rec,i}}} w_i}{\sum_{j=1}^{N_{\mathrm{gen,i}}} w_j} \qquad \text{and} \qquad \varepsilon_{\mathrm{o}} = \frac{\sum_{i=1}^{N_{\mathrm{rec,o}}} w_i}{\sum_{j=1}^{N_{\mathrm{gen,o}}} w_j}. \tag{B.3}$$

Here, $N_{\mathrm{rec,i}}$ and $N_{\mathrm{rec,o}}$ are the number of reconstructed events (after containment cuts) with true cores inside and outside the array, whereas $N_{\mathrm{gen,i}}$ and $N_{\mathrm{gen,o}}$ are the corresponding generated event numbers. The factor R renormalizes ε_{o} to the number of events generated inside the fiducial area,

$$R = \frac{\sum_{i=1}^{N_{\mathrm{gen,o}}} w_i}{\sum_{j=1}^{N_{\mathrm{gen,i}}} w_j}. \tag{B.4}$$

Both ε_i and ε_o are limited to $0 \leq \varepsilon_\mathrm{x} \leq 1$ (as a shorthand notation, ε_x will be used in all cases that apply to both ε_i and ε_o).

These individual efficiencies can be rewritten as (Husemann, 2010):

$$\varepsilon_\mathrm{x} = \frac{\sum_k w_k \varepsilon_{\mathrm{x},k}}{\sum_k w_k}, \tag{B.5}$$

where $\varepsilon_{\mathrm{x},k}$ is the probability to detect event k with variance

$$\sigma_{\varepsilon,\mathrm{x},k} = \varepsilon_{\mathrm{x},k}(1 - \varepsilon_{\mathrm{x},k}) \tag{B.6}$$

due to binomial statistics. For independent events, the error is the quadratic sum of individual contributions:

$$\sigma_{\varepsilon,\mathrm{x}} = \frac{\sqrt{\sum_k w_k^2 \, \varepsilon_{\mathrm{x},k}(1 - \varepsilon_{\mathrm{x},k})}}{\sum_k w_k}. \tag{B.7}$$

Assuming approximately constant $\varepsilon_{\mathrm{x},k} \equiv \varepsilon_\mathrm{x}$ (within an energy bin and zenith angle range):

$$\sigma_{\varepsilon,\mathrm{x}} = \sqrt{\varepsilon_\mathrm{x}(1 - \varepsilon_\mathrm{x})} \, \frac{\sqrt{\sum_k w_k^2}}{\sum_k w_k}. \tag{B.8}$$

It is noteworthy that, for the case of constant weights:

$$\frac{\sqrt{\sum_k w_k^2}}{\sum_k w_k} \xrightarrow{w_k \equiv 1} \frac{1}{\sqrt{N}}, \tag{B.9}$$

with the number of events N that corresponds to the standard case of binomial statistics in case of unweighted events. Finally, the error of ε is

$$\sigma_\varepsilon = \sqrt{\sigma_\mathrm{i}^2 + R^2 \sigma_\mathrm{o}^2}. \tag{B.10}$$

A more precise alternative would be to split the Monte Carlo sample into N_sample subsamples and calculate the efficiencies for each sample. Then, the spread of calculated efficiencies would be a measure of the variance of ε and correlations and variations of the $\varepsilon_{\mathrm{x},k}$ would be taken into account. However, this method is unfeasible due to the limited size of the Monte Carlo datasets available in this thesis.

Bibliography

This bibliography includes some IceCube internal resources, like Internal Reports and the IceCube Wiki. These are not publicly available. In cases where work not done by the author has not been documented in any other way, it was decided to list these references since they are the most precise documentation available. If access is required, please refer to a member of the IceCube collaboration.

R. Abbasi et al. A Study of the composition of ultrahigh energy cosmic rays using the High Resolution Fly's Eye. *Astrophys. J.*, 622:910–626, 2005.

R. Abbasi et al. Solar Energetic Particle Spectrum on 13 December 2006 Determined by IceTop. *Astrophysical Journal Letters*, 689:65–68, 2008.

R. Abbasi et al. The IceCube data acquisition system: Signal capture, digitization, and timestamping. *Nucl. Instrum. Meth.*, A601:294–316, 2009.

R. Abbasi et al. Calibration and Characterization of the IceCube Photomultiplier Tube. *Nucl. Instrum. Meth.*, A618:139–152, 2010.

R. Abbasi et al. Cosmic Ray Composition from 1 PeV – 50 PeV using IceTop and IceCube. *Paper in preparation*, 2011a.

R. Abbasi et al. The Radio Air Shower Test Array (RASTA) – enhancing the IceCube observatory. In *Proc 32nd International Cosmic Ray Conference*, Beijing, China, 2011b.

J. Abraham et al. Correlation of the Highest-Energy Cosmic Rays with Nearby Extragalactic Objects. *Science*, 318(5852):938–943, 2007.

J. Abraham et al. Measurement of the Depth of Maximum of Extensive Air Showers above 10^{18} eV. *Phys. Rev. Lett.*, 104(091101), 2010.

A. Achterberg et al. First year performance of the IceCube neutrino telescope. *Astropart. Phys.*, 26:155–173, 2006.

M. Ackermann et al. Optical properties of deep glacial ice at the South Pole. *J. Geophys. Res.*, 111(D13203), 2006.

M. Aglietta et al. The cosmic ray proton, helium and CNO fluxes in the 100 TeV energy region from TeV muons and EAS atmospheric Cherenkov light observations of MACRO and EAS-TOP. *Astropart. Phys.*, 21:223–240, 2004.

S. Agostinelli et al. GEANT4: A simulation toolkit. *Nucl. Instrum. Meth.*, A506: 250–303, 2003.

J. Ahrens et al. IceCube Preliminary Design Document. Technical report, 2001. URL `http://www.icecube.wisc.edu/science/publications/pdd/pdd.pdf`.

J. Allison et al. Geant4 developments and applications. *IEEE Trans. Nucl. Sci.*, 53: 270, 2006.

M. Amenomori et al. The all-particle spectrum of primary cosmic rays in the wide energy range from 10^{14} eV to 10^{17} eV observed with the Tibet-III air-shower array. *Astrophys. J.*, 678:1165, 2008.

L. Anchordoqui and T. Montaruli. In Search of Extraterrestrial High-Energy Neutrinos. *Annu. Rev. Nucl. Part. Sci.*, 60:129–162, 2010.

L. Anchordoqui et al. High energy physics in the atmosphere: phenomenology of cosmic ray air showers. *Ann. Phys.*, 314:145–207, 2004.

K. Andeen. Private communication, 2011a.

K. Andeen. *First Measurements of Cosmic Ray Composition from 1-50 PeV using New Techniques on Coincident Data from the IceCube Neutrino Observatory*. PhD thesis, University of Wisconsin-Madison, 2011b.

B. V. Antokhonov et al. Tunka-133: the New EAS Cherenkov Light Array for Cosmic Ray Study (10^{15} – 10^{18} eV). In *Proc. 25th Texas Symposium on Relativistic Astrophysics*, Heidelberg, Germany, 2010.

T. Antoni et al. The cosmic-ray experiment KASCADE. *Nucl. Instrum. Meth. A*, 513:490–510, 2003.

W. D. Apel et al. The KASCADE-Grande experiment. *Nucl. Instrum. Meth. A*, 620: 202–216, 2010a.

W. D. Apel et al. Lateral distribution of the radio signal in extensive air showers measured with LOPES. *Astropart. Phys.*, 32:294–303, 2010b.

J.C. Arteaga-Velázquez et al. The KASCADE-Grande experiment: measurements of the all-particle energy spectrum of cosmic rays. In *Proc. 16th International Symposium on Very High Energy Cosmic Ray Interactions*, Batavia, IL, USA, 2010.

K. Asakimori et al. Cosmic Ray Proton and Helium Spectra — Results from the JACEE Experiment. *Astrophys. J.*, 502:278–283, 1998.

J. Auffenberg. IC79 UHE/EHE neutrino analysis with IT SLC veto. In *IceCube Collaboration Meeting*, Brussels, Belgium, 2010. IceCube internal.

P. Auger, P. Ehrenfest, R. Maze, J. Daudin, and R.A. Fréon. Extensive Cosmic-Ray Showers. *Rev. Mod. Phys.*, 11:288–291, 1939.

G. Battistoni et al. The FLUKA code: Description and benchmarking. volume 896 of *AIP Conference Proceeding*, pages 31–49, 2007. Proceedings of the Hadronic Shower Simulation Workshop 2006.

M. Beimforde. Calibration of air shower signals in the IceTop detector using cosmic ray muons. Diploma thesis, Humboldt-Universität zu Berlin, 2006.

P. Berghaus. IceTop Snow Parametrization, 2009a. URL `http://wiki.icecube.wisc.edu/index.php/IceTop_Snow_Parametrization`. IceCube Wiki, retrieved June 16, 2011.

P. Berghaus. IceTop PMT Saturation, 2009b. URL `http://wiki.icecube.wisc.edu/index.php/IceTop_PMT_Saturation`. IceCube Wiki, retrieved July 19, 2011.

P. Berghaus. First Look at SLC Hits as InIce Veto. In *IceCube Collaboration Meeting*, Brussels, Belgium, 2010. IceCube internal.

P. Birr. Analysis of Signals in the IceTop Detector to identify Muons. Bachelor's thesis, Humboldt-Universität zu Berlin, 2010.

J. Blümer, R. Engel, and J.R. Hörandel. Cosmic rays from the knee to the highest energies. *Prog. Part. Nucl. Phys.*, 63:293–338, 2009.

G. D'Agostini. A Multidimensional unfolding method based on Bayes' theorem. *Nucl. Instrum. Meth.*, A362:487–498, 1995.

C. David. Study of the IceCube DOM analog signals. *IceCube Internal Report*, (200910002), 2009.

L. Demirörs. IT calib run0037728, 2007. URL `http://wiki.icecube.wisc.edu/index.php/IT_calib_run0037728`. Retrieved April 4, 2011.

L. Demirörs. IceTop VEM calibration, 2008. URL `http://wiki.icecube.wisc.edu/index.php/IceTop_VEM_calibration`. IceCube Wiki, retrieved March 27, 2011.

A. Dixit et al. New physics, the cosmic ray spectrum knee, and pp cross section measurements, 2010. arXiv:astro-ph.CO/0912.0980v3.

B. Efron and R. T. Tibshirani. *An introduction to the bootstrap*. Chapman & Hall/CRC, London, 1998.

A. D. Erlykin and A. W. Wolfendale. Structure in the cosmic ray spectrum: an update. *J. Phys. G: Nucl. Part. Phys.*, 27:1005–1030, 2001.

A. D. Erlykin and A. W. Wolfendale. The Knee in the Cosmic Ray Energy Spectrum. In *Proc. 31st International Cosmic Ray Conference*, Łódź, Poland, 2009.

A. Fassò, A. Ferrari, J. Ranft, and P.R. Sala. FLUKA: a multi-particle transport code, 2005. CERN-2005-10 (2005), INFN/TC_05/11, SLAC-R-773.

T. Feusels. Core study, 2010. Presentation in IceTop telephone conference. Retrieved 16 May, 2011. IceCube Internal.

C. C. Finlay et al. International Geomagnetic Reference Field: the eleventh generation. *Geophysical Journal International*, 183:1216–1230, 2010.

R. S. Fletcher, T. K. Gaisser, P. Lipari, and T. Stanev. SIBYLL: An event generator for simulation of high energy cosmic ray cascades. *Phys. Rev. D*, 50:5710–5731, 1994.

R. S. Fletcher, T. K. Gaisser, P. Lipari, and T. Stanev. Air shower calculations with the new version of SIBYLL. In *Proc. 26th International Cosmic Ray Conference*, volume 1, page 415, Salt Lake City, USA, 1999.

M. Furukawa et al. All Particle Spectrum, Average Mass From RUNJOB Data. In *Proc. 28th International Cosmic Ray Conference*, pages 1885–1888, Tsukuba, Japan, 2003.

T.K. Gaisser. *Cosmic Rays and Particle Physics*. Cambridge University Press, 1990.

A.P. Garyaka et al. An all-particle primary energy spectrum in the $3 - 200\,\mathrm{PeV}$ energy range. *J. Phys. G*, 35(115201), 2008.

L. Gerhardt et al. Study of High p_T Muons in IceCube. In *Proc. 31st International Cosmic Ray Conference*, Łódź, Poland, 2009. arXiv:astro-ph.HE/0909.0055.

R. Glasstetter et al. Analysis of electron and muon size spectra of EAS. In *Proc. 26th International Cosmic Ray Conference*, Salt Lake City, USA, 1999.

K. Greisen. Cosmic Ray Showers. *Annu. Rev. Nucl. Sci.*, 10:63–108, 1960.

K. Greisen. End to the Cosmic-Ray Spectrum? *Phys. Rev. Lett.*, 16:748–750, 1966.

J.-L. Han and R. Wielebinski. Milestones in the Observations of Cosmic Magnetic Fields. *Chin. J. Astron. Astrophys.*, 2(4):293–324, 2002.

P. C. Hansen. *Rank-Deficient and Discrete Ill-Posed Problems*. SIAM, Philadelphia, PA, USA, 1998.

A. Haungs et al. Results on the cosmic ray energy spectrum measured with KASCADE-Grande. In *Proc. 31st International Cosmic Ray Conference*, Łódź, Poland, 2009.

D. Heck et al. CORSIKA: A Monte Carlo Code to Simulate Extensive Air Showers. *Report FZKA*, 6019, 1998. URL `http://www-ik.fzk.de/corsika/physics_description/corsika_phys.pdf`.

A. E. Hedin. Extension of the MSIS thermosphere model into the middle and lower atmosphere. *J. Geophys. Res.*, 96:1159–1172, February 1991.

V.F. Hess. Beobachtungen der durchdringenden Strahlung bei sieben Freiballonfahrten. In *Mitteilungen aus dem Institut für Radiumforschung, Sitzungsberichte der mathematisch-naturwissenschaftlichen Klasse der kaiserlichen Akademie der Wissenschaften*, volume 121, pages 2001–2032. Wien, 1912.

A. M. Hillas. The Knee of the Cosmic Ray Spectrum: Not a Magnetic Trapping Effect? In *Proc. 16th International Cosmic Ray Conference*, Kyoto, Japan, 1979.

A.M. Hillas. Cosmic Rays: Recent Progress and some Current Questions. In H.-R. Klöckner, M. Jarvis, and S. Rawlings, editors, *Cosmology, Galaxy Formation and Astroparticle Physics on the pathway to the SKA*, Oxford, UK, April 10th-12th 2006.

U. Husemann. Private communication, 2010.

J. Hörandel. Models of the knee in the energy spectrum of cosmic rays. *Astropart. Phys.*, 21:241–265, 2004.

J.R. Hörandel. On the Knee in the Energy Spectrum of Cosmic Rays. *Astropart. Phys.*, 19:193–220, 2003.

K. Kamata and J. Nishimura. The Lateral and Angular Structure Functions of Electron Showers. *Progr. Theor. Phys. Suppl.*, 6:93–155, 1958.

D. Kazanas and A. Nicolaidis. Cosmic Ray Spectrum "Knee": A Herald of New Physics?, 2001. arXiv:astro-ph/0103147v2.

F. Kislat. Study of charge and time fluctuations of signals in the IceTop detector. Diploma thesis, Humboldt-Universität zu Berlin, 2007.

F. Kislat, S. Klepser, and A. Van Overloop. A Lateral Distribution Function and Fluctuation Parametrisation for IceTop, 2007. URL `http://internal.icecube.wisc.edu/reports/details.php?type=report&id=icecube%2F200702001`. IceCube Internal Report icecube/200702001-v6.

S. Klepser. *Reconstruction of Extensive Air Showers and Measurement of the Cosmic Ray Energy Spectrum in the Range of 1-80PeV at the South Pole*. PhD thesis, Humboldt-Universität zu Berlin, 2008.

W. Kohlhörster, I. Matthes, and E. Weber. Gekoppelte Höhenstrahlen. *Naturwissenschaften*, 26:576, 1938.

H. Kolanoski. *Einführung in die Astroteilchenphysik*. Lecture notes, Humboldt-Universität zu Berlin, Germany, 2010. URL `http://www-zeuthen.desy.de/~kolanosk/astro0910/skripte/astro.pdf`. Retrieved December 26, 2010.

G. V. Kulikov and G. B. Khristiansen. On the size spectrum of Extensive Air Showers. *Sov. Phys. JETP*, 8:441–444, 1959. Originally published in *Zh. Éksp. Teor. Fiz.*, 35:635–640, 1958, in Russian.

T. Kuwabara and S. Tilav. IceTop Snow Height Estimation From VEMCal, 2011. URL `http://wiki.icecube.wisc.edu/index.php/IceTop_Snow_Height_Estimation_From_VEMCal`. IceCube Wiki, retrieved July 14, 2011.

L. A. Kuzmichev. Tunka-133: status, all particle spectrum and future plans, May 2011. URL `http://agenda.infn.it/getFile.py/access?contribId=40&sessionId=29&resId=0&materialId=slides&confId=3187`. Presentation given at *Roma International Conference on Astroparticle Physics*.

D. R. Lide. *CRC Handbook of Chemistry and Physics 48th Edition*. Chemical Rubber Company, 1967.

A. Lucke. Analysis of Signals in the IceTop Detector to Identify Muons in Extensive Air Showers. Diploma thesis, Humboldt-Universität zu Berlin, 2008.

T. Melzig. Verbesserung der IceTop-Detektorsimulation unter Verwendung von Geant4. Master's thesis, Humboldt-Universität zu Berlin, 2011. In German.

G. Miloshevich. Analysis of β parameter for IceTop Air Shower Reconstruction. Summer student's report, DESY, Zeuthen, 2009.

K. Nakamura et al. Review of particle physics. *J. Phys. G*, 37(075021), 2010.

W.R. Nelson, H. Hirayama, and D.W.O. Rogers. The EGS4 Code System. *Report SLAC-0265*, 1985. URL `http://www.slac.stanford.edu/pubs/slacreports/slac-r-265.html`.

J. Ochab. Test of shower reconstruction procedures with the IceTopA, IceTopB subarrays. Summer student's report, DESY, Zeuthen, 2007.

S. Ostapchenko. QGSJET-II: towards reliable description of very high energy hadronic interactions. *Nucl. Phys. B Proc. Suppl.*, 151:143–146, 2006a.

S. Ostapchenko. QGSJET-II: results for extensive air showers . *Nucl. Phys. B Proc. Suppl.*, 151:147–150, 2006b.

D.H. Perkins. *Particle Astrophysics*. Oxford University Press, Oxford, UK, 2003.

B. Peters. Origin of Cosmic Radiation. *Nuovo Cimento Suppl.*, 14:1868–1888, 1959.

B. Peters. Primary Cosmic Radiation and Extensive Air Showers. *Nuovo Cimento*, 22:4500–4519, 1961.

T. Pierog. Review of (High Energy) Hadronic Interaction Models. In *CORSIKA School*, Lauterbad, Germany, 2008. URL `http://www-ik.fzk.de/corsika/corsika-school2008/talks/3_thursday/pierog_had_inter.pdf`.

K. Rawlins. IceTop Snow as a Function of Time, 2011. URL `http://wiki.icecube.wisc.edu/index.php/IceTop_Snow_as_a_Function_of_Time`. IceCube Wiki, retrieved July 14, 2011.

S. P. Reynolds. Supernova Remnants at High Energy. *Annu. Rev. Astron. Astrophys.*, 46:89–126, 2008.

C. Roucelle. Documentation for the DOMcalibrator module. *IceCube Internal Report*, (200709001), 2007a.

C. Roucelle. DOMsimulator user's guide for IceSim release V02-00-00 and more... *IceCube Internal Report*, (200709002-v2), 2007b.

F. Schröder. Radio detection of cosmic ray air showers with LOPES, February 2010. URL `https://indico.desy.de/getFile.py/access?contribId=51&sessionId=7&resId=0&materialId=slides&confId=2729`. Presentation given at the *Cosmic Ray Workshop*, Zeuthen, Germany.

O. Schulz. *The design study of IceCube DeepCore: Characterization and veto studies*. PhD thesis, Universität Heidelberg, 2010. URL `http://www.ub.uni-heidelberg.de/archiv/10978`.

T. Stanev, P. L. Biermann, and T. K. Gaisser. Cosmic rays. IV. The spectrum and chemical composition above 10^4 GeV. *Astron. Astrophys.*, 274:902–908, July 1993.

A. W. Strong, I. V. Moskalenko, and V. S. Ptuskin. Cosmic-Ray Propagation and Interactions in the Galaxy. *Annu. Rev. Nucl. Part. Sci.*, 57:285–327, 2007.

S. P. Swordy. Expectations for Cosmic Ray Composition Changes in the Region 10^{14} to 10^{16} eV. In *Proc. 24th International Cosmic Ray Conference*, volume 2, pages 697–700, Rome, Italy, 1995.

S. V. Ter-Antonyan and L. S. Haroyan. About EAS size spectra and primary energy spectra in the knee region, 2000. arXiv:hep-ex/0003006v3.

S. Tilav. IceTop Good Run List, 2007. URL `http://icecube.bartol.udel.edu/GoodRun/IceTop-GoodRunList-2007A.html`.

S. Tilav. Private communication, 2011.

S. Tilav et al. Atmospheric Variations as observed by IceCube. In *Proc. 31st International Cosmic Ray Conference*, Łódź, Poland, 2009.

H. Ulrich. *Untersuchungen zum primären Energiespektrum der kosmischen Strahlung im PeV-Bereich mit dem KASCADE-Experiment*. PhD thesis, Universität Karlsruhe, 2004. In German.

A. Van Overloop. TopLeInjector, 2010. URL `http://wiki.icecube.wisc.edu/index.php/TopLeInjector`. IceCube Wiki, retrieved May 4, 2011.

T. Waldenmaier. Private communication, 2007.

T. Waldenmaier. IceTop Configurations, 2010. URL `http://wiki.icecube.wisc.edu/index.php/IceTop_Configurations`. IceCube Wiki, retrieved July 16, 2011.

J. Warren, J. Hughes, et al. Tycho's Supernova Remnant, NASA/CXC/Rutgers, 2005. URL `http://chandra.harvard.edu/photo/2005/tycho/`. Retrieved January 2, 2011.

K. Werner, F.-M. Liu, and T. Pierog. Parton ladder splitting and the rapidity dependence of transverse momentum spectra in deuteron-gold collisions at the BNL Relativistic Heavy Ion Collider. *Physical Review C*, 74(044902), 2006.

R. Wischnewski and L. Kuzmichev. Private communication, 2011.

G. T. Zatsepin and V. A. Kuz'min. Upper Limit of the Spectrum of Cosmic Rays. *Soviet Journal of Experimental and Theoretical Physics Letters*, 4:78–80, 1966.

List of Figures

List of Tables

Acknowledgments

There are many people without whose help this thesis probably would not exist.

First of all, I would like to thank my advisor Prof. Dr. Hermann Kolanoski for his help and guidance throughout the last five years. When I started my Diploma work he convinced me that working on IceTop was a good choice and I stayed with the project for the work on this thesis.

I always felt very well supported by Christian Spiering, who was a good and understanding head of the astroparticle group at DESY and who allowed me to travel to various schools and conferences.

I am most thankful to Tom Gaisser and for making possible my trip to South Pole. When I got there, James Roth and Chris Elliott gave me an excellent introduction to IceTop tank deployment and the Freeze Control Units. Great support at the Pole also came from Jim Haugen, Gary Freeman and Emanuel Jacobi.

I would also like to thank Tilo Waldenmaier very much for the pleasant time we had sharing an office for almost three years. I enjoyed it very much and we had many useful and productive discussions. What would I have done without your invaluable knowledge of the technical details of IceTop?

Many thanks also go to Patrick Berghaus. He only spent a few months in Zeuthen, but I think those were some of the most productive ones for me. The discussions we had were extremely helpful.

I am very much indebted to Makio Shibata from the Tibet experiment, Andreas Haungs from KASCADE-Grande, and Leonid Kuzmichev from Tunka for giving me access to their results, which I used in the comparison plots in the final chapter.

Several people have proof-read parts of this thesis. I would like to thank all of them for their helpful comments and criticism: Markus Ackermann, Gareth Hughes, Eike Middell, Heike Prokoph, Arne Schönwald, Jakob van Santen, Achim Stößl, Nathan Whitehorn and Juan Pablo Yáñez.

I am extremely thankful to Stefan Klepser, who was a great supervisor during my time as a Diploma student. He taught me a lot and always took the time to answer all the questions I had while I got started working on IceTop.

In the last three years I have co-supervised several Master, Bachelor and summer students: Sarah Becker, George Miloshevich, Thomas Melzig, Rebekka Schlichte, Patric Birr and Lev Dushkin. They gave great help and insight and working with

them was a big pleasure. Thanks to all of them for the nice time we had sharing an office, the “Headquarter”.

For almost five years I have now been part of the IceCube family. During this time I have met many wonderful people and great physicists. I am especially happy to have made the acquaintance of Arne Van Overloop, Tom Feusels, Serap Tilav, Don La Dieu, and Troy Straszheim.

The exceptional social environment of the astroparticle group at DESY made this a great place to work. Among the many people I met I would like to thank most of all Konstancja Satalecka, Elisa Bernardini, Sebastian Panknin, and Robert Franke, with whom I spent many enjoyable lunch breaks with interesting and fun discussions. Also Robert Lauer, Gessica De Caneva, Rebecca Gozzini, Stefan Schlenstedt, Delia Tosi, Ralf Wischnewski, and Igor Telezhinsky were great colleagues and made the time I spent at DESY working on this thesis enjoyable.

Last, but certainly not least, I want to thank my family for all the support they gave me throughout my years of study.

Selbständigkeitserklärung

Hiermit erkläre ich, dass ich die vorliegende Arbeit selbständig und nur unter Verwendung der angegebenen Literatur und Hilfsmittel angefertigt habe. Ich habe mich nicht anderweitig um einen Doktorgrad beworben und besitze keinen Doktorgrad. Die Promotionsordnung der Mathematisch-Naturwissenschaftlichen Fakultät I der Humboldt-Universität ist mir bekannt.

Berlin, den 21. Juli 2011 Fabian Kislat